High contrast imaging polarimetry of circumstellar environments

ISBN 978-90-393-5614-2
Printed by Wöhrmann Print Service, Zutphen

Cover image: ExPo images of the young star MWC 147. The *polarized intensity* image, shown at the center, indicates the presence of dust around the star. The blue vectors represent the orientation of the polarization plane. On top, the *intensity* image of the same star.
Cover designed by Juan Agüera © 2011 Soda Graphics
www.sodagraphics.com

High contrast imaging polarimetry of circumstellar environments

Hoog contrast beeldvorming polarimetrie van circumstellaire omgevingen

(met een samenvatting in het Nederlands)

Proefschrift

ter verkrijging van de graad van doctor aan de Universiteit Utrecht op gezag van de rector magnificus, prof. dr. G. J. van der Zwaan, ingevolge het besluit van het college voor promoties in het openbaar te verdedigen op Donderdag 23 september 2011 des middags te 2.30 uur

door

Héctor Cánovas Cabrera

geboren op 29 february 1984 te Almería, España

Promotor: Prof. dr. C. U. Keller

Imagination is more important than knowledge.
Knowledge is limited.
Imagination encircles the world.

— Albert Einstein

To my parents. To my sister.

Contents

(...) And lastly, the unusual Refraction of Island-Crystal looks very much as if it were performed by some kind of attractive virtue lodged in certain Sides both of the Rays and of the Particles of the Crystal (...) as the poles of two Magnets answer to one another (...)
— Sir Isaac Newton (Question 29, Book III, *Opticks*)

Chapter 1

Introduction

1.1 Why Polarimetry

Imagine one rainy afternoon of May, in the Netherlands. You are cycling from the *Sterrekundig Instituut* of Utrecht University towards the city center. Because of the rain, there is a thin layer of water covering the road. Then, all of a sudden, the wind blows, and the clouds open allowing the sunlight to illuminate everything. Under certain conditions, the thin layer of rain water over the road will fiercely glare, reflecting (i.e., *scattering*) all the sunlight in the direction to your eyes. For a moment, you have to close your eyes, and you may regret not wearing a pair of *polarized* sunglasses.[1]

This example can help to understand what happens when trying to obtain images of the surroundings of a star. The light of the stars is typically four 4 orders of magnitude (a factor 10^4) brighter than the light coming from its immediate surroundings such as a circumstellar disk. In the case of exoplanets, the contrast achieved between star and (exo-) planet is even higher, reaching 10^9 for Jupiter-like planets, and 10^{11} or even higher for Earth-like ones (Burrows et al. 2004, Sudarsky et al. 2005, Burrows 2005). So, as it happens in the example given above, the light coming from a star is so intense that it is practically impossible to see anything but the star itself. To remove the intense starlight to detect the signatures produced by faint and close companions suppose a challenge for modern astronomy. High contrast imaging is the branch of the astronomy that aims to reach contrast ratios higher than five orders of magnitude (10^5) at small separations from a central object (Oppenheimer & Hinkley 2009). This a new, comparatively young, field of modern astronomy that has made great progress in the last years.

Since the discovery of the first exoplanet by Wolszczan & Frail (1992), a huge effort has been made by the astronomical community to develop techniques which could

[1] Polarized sunglasses can remove more light than the unpolarized ones. Reflected, scattered light, becomes polarized. If the polarized glass is oriented on the right direction, most of the scattered light is removed.

help to detect such faint companions and, eventually, image them. For instance, the "locally optimized combination of images" (LOCI) algorithm (Lafrenière et al. 2007) based on a locally optimized point spread function (PSF) subtraction, allows to effectively remove most of the (unwanted) star light. Important advances in coronagraphic techniques (see, for instance, Soummer et al. 2007, Hinkley et al. 2007, Soummer et al. 2009) are producing very good results in blocking the light from the central stars. Adaptive Optics (AO) systems, when combined with coronagraphs, can dramatically reduce the light from the central star, allowing to produce direct detections (images) in a few exoplanetary systems (see, for example, Chauvin et al. 2005, Marois et al. 2008a, Oppenheimer & Hinkley 2009). New techniques such as apodizing phase plates (Kenworthy et al. 2007, Quanz et al. 2010) can reduce the amount of starlight in one *half* of the field of view by a factor of almost two orders of magnitude without removing the flux from the close companions to the star. Furthermore, techniques such as the *nulling interferometry* (Martin et al. 2010) can also provide the high contrast ratios that are necessary to image faint companions such as exoplanets.

But there is also another technique, rarely used (when compared with the techniques mentioned above) in night time astronomy, which brings a more natural, elegant way to remove the light from the central star. It is *polarimetry*, and it has been widely used in the field of solar physics (i.e., Keller & von der Luehe 1992, Stenflo & Keller 1997, Trujillo Bueno et al. 2002) to reach contrast ratios of the order of 10^6 (Keller 1996). In most of the cases, both exoplanets and circumstellar environments are not hot enough to emit at optical wavelengths, and most of their light is actually scattered (and therefore polarized), star light. On the other hand, the light directly produced by the star is largely unpolarized. The electric field associated to the unpolarized light can be decomposed into two orthogonal states, each one of them carrying the same amount of energy. During the scattering process, the starlight becomes linearly polarized. This implies that there is now a preferred direction, or plane, in which the electric field associated to this scattered light is vibrating. Finally, and more important, the amount of polarized light will depend in more or less degree on the physical properties (i.e., size and shape) of the scattering particles and the scattering angle.

Polarimetry, or the study of the polarimetric properties of the light, can therefore provide a new way to remove the starlight, and to image and *characterize* the (polarizing) circumstellar environments, whatever their nature is.

1.1.1 Polarization Mechanisms and scattering

There are several physical mechanisms that can produce polarized light. Among them, the most studied one is the *scattering* process. Scattering is the physical processes in which photons or particles are deviated from their trajectory by another particle (atom, molecule or dust grain). One of the most famous consequences of scattering is the blue color of the sky, which is produced as a consequence of the dependence of Rayleigh scattering on the frequency.

In the scenarios that I study here, the scattering is produced by the small dust grains that are present in circumstellar disks and spherical shells. The scattering produced in those environments is *elastic*, i.e., the frequency of the light does not change during this process. What it changes is the *polarization state* of the light. As mentioned above, the electric field of the unpolarized light is vibrating in two orthogonal (polarization) planes. Therefore, it can be divided into two components that can be expressed in terms of an amplitude and a frequency. The amplitude of these two components is the same if the light is unpolarized. During the scattering process, one of these two components disappears or decreases its amplitude. In case the scattering angle is 90°, then the scattered light is fully polarized, and therefore the electric field associated to the scattered light only vibrates in one plane. This is linearly (fully) polarized light.

In general, and depending on the properties of the light, we can characterize the polarization state of the light as fully or partially polarized light, and as linearly, circularly or elliptically polarized. There are two formalisms in optics that describe the polarization of the light, which are the Mueller formalism and the Stokes-Mueller formalism. The former describes *fully* polarized light, and the latter describes *partially* polarized light. Because all the objects that we observe are partially polarized, our observations are described in terms of the Stokes formalism. In this notation, the state of the light is described by the four vectors I, Q, U and V.

In this thesis, I discuss the images produced by ExPo (described in detail below), an imaging polarimeter sensitive to linearly polarized light. Therefore, we do not measure the "V" component of the light, in case there is any circular polarization in the objects that we observe.

1.2 Circumstellar environments

Soon after the launch of the Infrared Astronomy Satellite (IRAS), the astronomical community had access to a new class of astrophysical objects, such as circumstellar disks. The infrared excess that some stars show in their spectra is the fingerprint of a dusty disk surrounding them. The first disks detected with IRAS were the ones around Vega (Harvey et al. 1984), β Pictoris (Smith & Terrile 1984) and Fomalhaut (Gillett 1986). From these three, two of them, β Pictoris and Fomalhaut, host planets which have been directly imaged (Lagrange et al. 2010, Bonnefoy et al. 2011, Kalas et al. 2005, Kalas et al. 2008). These three disks are classified as "debris disks". This type of disk are formed from the leftover material that has not been used during the (exo-) planet formation process. Their central stars are already burning hydrogen in their nucleus, so these stars are located in the main sequence of the Hertzsprung Russell diagram.

A different type of disk can be found around extremely young protostars. During the early stages of star formation, the star is not yet hot enough to produce nuclear reactions in its nucleus. The gravitational energy generated during the so-called "accretion phase" is released in the form of light. In this stage, the star is continuously

accreting material from a protoplanetary disk, and it usually suffers from episodes of strong outbursts and outflows. Depending on the masses and properties of these stars, they are classified as Herbig (those with masses above two solar masses, $M \geq 2M_{\odot}$), T Tauri, and FU Ori (these two with masses below two solar masses, $M \leq 2M_{\odot}$) stars. Amongst them, the FU Ori stars are the ones which produce the strongest outbursts (for a description of the FU Ori phenomenon, see Hartmann & Calvet 1995, Hartmann & Kenyon 1996a). These episodes are associated with violent thermal accretion events (Bell et al. 1995). T Tauri stars are believed to be more evolved than FU Ori stars (see, for instance Weintraub et al. 1991). Disks around Herbig AeBes stars (see Waters et al. 1998a, for a detailed description of these stars) are classified according to their shape into *flared* and *settled* disks (Meeus et al. 2001a, Dullemond & Dominik 2004a). Figure 1.1 shows the basic disks properties according to their state in this classification.

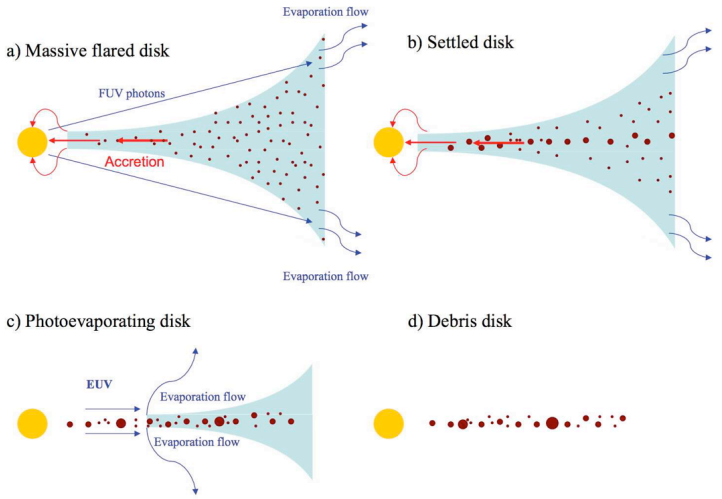

Figure 1.1: Example of different stages of the evolution of disk. The effect of the dust properties on the (polarimetric) observational features of flared and settled disks is investigated in Chapter 2 of this thesis. Credit: Figure 6, from Williams & Cieza (2011), to be published in the Annual Review of Astronomy and Astrophysics, vol. 49 .

The study of protoplanetary disks can help to understand how planet formation works, eventually leading to a better understanding of how our solar system was formed. The current picture of these systems shows that we are still far away from fully understanding all the physical processes that happen during the evolution of the protoplanetary disks (to mention some studies, Dullemond & Monnier 2010, Williams & Cieza 2011, Dullemond et al. 2007a, Armitage 2011).

Finally, a different kind of circumstellar environment can be found around post-

AGB (evolved) stars. In these cases, an intermediate-mass star ($1 - 8M_{\odot}$) is facing the final chapters of its life. During this stage of its life, the star is producing extremely strong stellar wind. As a consequence, it expels its outermost layers into the interstellar medium (Weinberger & Kerber 1997). At the early stages of the post-AGB phase, a proto-planetary nebulae is formed. Later on, and when the central star is hot enough to ionize all its surroundings, the PPN becomes a planetary nebulae (PN). The study of the dust properties around evolved stars can therefore lead to a better understanding of the evolution of these stars.

Figure. 1.2 shows, as an example, three different circumstellar environments observed by the Hubble Space Telescope (HST). All the cases mentioned before share a common scenario: there is a central source of light (either an evolved star or protostar) surrounded by dust. As explained above, the dust scatters the light from the star, (linearly) polarizing it. Because of this, imaging polarimetry is a very powerful tool to better diagnose the dust properties around these kind of objects. Furthermore, the high contrast ratios that can be achieved by means of imaging polarimetry can provide us with detailed images of the circumstellar environments.

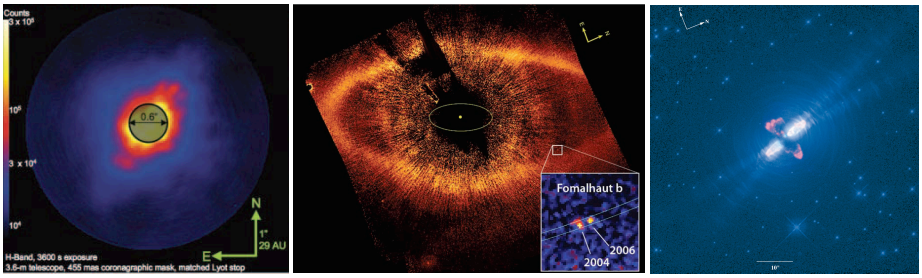

Figure 1.2: Different types of circumstellar environments, imaged with the Hubble Space Telescope (HST). The scale of each image is different. Left: Protoplanetary disk around AB Aurigae. Credit: Figure 1, from Oppenheimer et al. (2008). Center: Debris disk around Fomahault. Credit: Figure 1, from Kalas et al. (2008). Right: Proto-Planetary Nebulae (the "Egg Nebula"). Credit: Figure 1, from Sahai et al. (1998).

1.3 ExPo: high contrast imaging polarimetry

ExPo (the Extreme Polarimeter, see Rodenhuis et al. 2008a, 2011a) is the dorsal spine of this thesis. This instrument is a dual-beam imaging polarimeter, optimized for the (polarimetric) characterization of circumstellar environments at optical wavelengths.

It has been designed and built at Utrecht University. During the nearly four years since its first light, ExPo has assisted to five campaigns at the William Herschel Telescope (WHT) and it has provided us with Tera bytes of (imaging-polarimetric) data. ExPo has been designed as a modular, flexible instrument, so it can easily be modified to (for instance) change its field of view. Designed as a visitor instrument, it can go on different telescopes as long as there is an optical table onto which ExPo can be mounted.

The key concept of ExPo is the combination of fast modulation, which is attained by its ferroelectric liquid crystal (FLC), and the dual-beam capability, which is provided by a cubic beamsplitter. The FLC is a device that can rotate the polarization plane (the plane in which the electric field of the light is vibrating). In ExPo, the FLC switches between two different states (we call then "A" and "B" states). The polarization plane of the "B" state is rotated by 90° with respect to the polarization plane of the "A" state. The FLC switches between these two states every 0.028 seconds. The beamsplitter divides the beam of light into two beams with orthogonal polarization states. When the EM-CCD[2] of ExPo reads a frame, two simultaneous images, with opposite polarization states, are recorded. When the FLC changes its state, two new (simultaneous) images are recorded again. At the end of a cycle, when the FLC recovers its original state, four different images are produced. By subtracting these images, a final, polarization image is obtained.

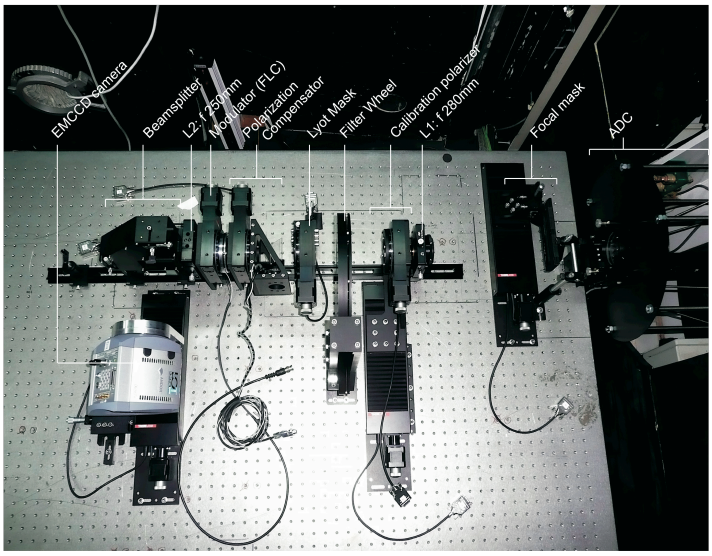

Figure 1.3: ExPo instrument mounted at the Nasmyth platform of the 4.2 m William Herschel Telescope (Observatorio del Roque de los Muchachos, La Palma). Courtesy of Michiel Rodenhuis.

[2]Electron Multiplying Charge Coupled Device. The main difference with respect to the "standard" CCD devices is that the EM-CCDs can amplify the signal without amplifying the readout noise.

The field of view of ExPo is 20″ × 20″, and its set of filters includes, among others, Sloan R and I filters, H_α and Na filters. The combination of dual-beam imaging with polarimetry allows ExPo to minimize the speckle noise, one of the major sources of error when generating high-contrast images (Racine et al. 1999, Sivaramakrishnan et al. 2002, Hinkley et al. 2009). ExPo can currently reach a maximum contrast ratio of 10^5 at 1.5″ from the central star (Rodenhuis et al. 2011a).

In September 2011 the AO system designed for ExPo will be commissioned at the McMath-Pierce telescope (Kitt Peak). This new capability, combined with a coronagraph mask, will increase the sensitivity of this instrument by a factor of, at least, 1.5 orders of magnitude. Furthermore, an integral field unit (IFU) specifically designed for ExPo is currently being built, so future versions of this instrument will be able to perform *spectropolarimetry*.

The analysis and understanding of this instrument have been the corner stone of my PhD. ExPo is an instrument that has seen its first light in less than two years since the beginning of its building. In the last four years, I have participated in five campaigns to observe with ExPo at the William Herschel Telescope, to perform imaging polarimetry of planets as Venus and Saturn, protoplanetary disks and evolved stars.

To date, ExPo is the only dual-beam imaging polarimeter working at optical wavelengths. The science produced by this instrument increases our knowledge about circumstellar environments in a variety of objects, from young to evolved stars. Furthermore, the experience acquired during the design and use of this instrument can help to understand the problems that arise when doing high contrast imaging by means of polarimetry. Part of the ExPo team is actively collaborating with the design of EPOL, the polarimetry part of EPICS, one of the "planet hunters" that will go onboard the European Extremely Large Telescope (E-ELT).

1.4 Outline of this Thesis

This work spins around ExPo results. The chapters 2 and 3 of this thesis are focussed onto the analysis and understanding of ExPo observations. In the second chapter we describe the data reduction techniques that must be applied to minimize instrumental artifacts when dealing with ExPo data. In the third chapter, simulations of different protoplanetary disks are combined with a numerical simulation of ExPo, to both understand the effect of the dust properties and instrumental effects on the real observations. The fourth chapter shows the result of ExPo observations of Z CMa, a young binary system. The fifth and last chapter analyzes the dust composition of the neutral envelope of BD+303639, a planetary nebulae with a Wolf Rayet [WC9] as a central star.

Data Reduction Techniques for High Contrast Imaging Polarimetry

ExPo is an instrument that has been designed and built "from scratch" at Utrecht University. It is important to rigorously understand the behavior of the instrument

and to know its strengths and weaknesses. Moreover, and due to the enormous amount of data that can be produced with ExPo [3] (around 500 Gb within one night at the telescope), it is crucial to have an automated and reliable pipeline. In this chapter we describe the data reduction approach that should be used when reducing data produced by ExPo. Some of the results that we obtain here are only applicable to ExPo observations, such as for the image alignment approach described in this analysis. In this chapter it is proven that, when reducing ExPo data, centering according to a reference image (template) produces less noisy results than centering on the brightest speckle, as it is usually done when very short exposure times are used.

Protoplanetary disk simulations

A proper interpretation of polarimetric observations is far from trivial. Depending on the grain properties, the properties of the objects observed (for instance, settled or flared disk), and the artifacts introduced by the instrument and/or telescope, it is possible to infer very different conclusions. In Chapter 2 we first simulate the effects of the dust grain properties in two different types of protoplanetary disks: flared and settled. We then combine this simulations with a numerical simulation of the ExPo instrument. This simulation includes a set of ExPo point spread functions (PSFs) with photon noise, and instrumental artifacts such as readout noise or instrumental polarization. The simulated-ExPo data is then reduced with the data reduction approach described in the first chapter of this thesis. These simulations allow us to better understand the data produced by this instrument, as well as the artifacts introduced during the data reduction (for instance, the effects of an incorrect estimation of the instrumental polarization). The numerical simulation of ExPo described here is used during the modeling of the observations of Z CMa, discussed in the Chapter 4 of this thesis, and BD+303639, discussed in the Chapter 5.

Z CMa: Constraining the properties of a young binary system via Imaging Polarimetry

In Chapter 4 we present the first imaging polarimetric data of Z CMa. This is a binary system of great complexity, where an asymmetrical dust cocoon surrounds the primary, a Herbig Be star. A huge jet associated with this star is carving out a cavity in the infalling envelope that surrounds both the primary and the secondary, a FU Ori star. With the data provided by ExPo, we detect three different polarized features on this target. Two of them have not been described in previous observations of this system, and we discuss their possible sources. We find that a hole in the dust cocoon surrounding the primary can explain one of the polarization features that we observe. We also confirm that the scattering on the walls of the cavity carved out by the jet is the source of the second polarization feature that we measure. We suggest that another hole on the dust cocoon, or a jet-cloud collision, can be the source of

[3] In its standard configuration, ExPo takes an image every 0.028 seconds. During a whole night, around $1 \cdot 10^6$ images can be recorded with ExPo.

the third polarized feature in our images. Finally, a comparison of our observations with a model obtained with a radiative transfer code allows us to obtain a first approximation to the falling rate of the infalling envelope that surrounds the whole system.

Characterizing the neutral halo of BD+303639 via imaging polarimetry

BD+303639 is a fascinating planetary nebulae (PN). Its central star is a carbon-rich, late-type Wolf-Rayet star [WC0]. This system called the attention of the astronomical community after the discovery of the presence of silicates (associated to an oxygen-rich chemistry) in the nebulae. Because of the youth of its nebulae, this implies that the central star of BD+303630 has changed its chemistry from O-rich to C-rich some time no longer than 1000 years ago. Measurements of the composition of the neutral halo around the central star are fundamental to explain the evolution, and change in chemistry of BD+303639. ExPo observations of this nebulae provide us with an accurate measurement of the dust properties in its neutral envelope. Comparison with models allow us to measure the outer radius of the O-rich ring around the star.

1.5 Overview of ExPo results

During its five campaigns as a visitor instrument at the William Herschel Telescope, ExPo has successfully observed more than 20 different objects. ExPo observations of protostars have produced polarized images of some of the most famous types of young stars such as T Tauri, AB Aurigae or FU Ori. The observations of evolved, post-AGB stars, have also provided us with a considerable amount of detections. Among others, CW Leo, R cRB, AFGL 2088 (the "'egg" nebula) and IRC 10420 show very clear polarized features. Some of these results are shown in Fig. 1.4 as an example of the zoo of images produced by ExPo.

Among all the types of objects observed by ExPo, only debris disks have failed to show polarimetric evidences of dust. This can be caused either by their projected size, which is typically bigger than the current ExPo field of view, or because they are intrinsically fainter than, for instance, protoplanetary disks. With the new capabilities of ExPo (AO system and coronagraphs), we will observe these systems again, in an attempt to produce imaging polarimetry of debris disks.

1.6 Future Directions

Polarimetry is a technique that can be combined with spectroscopy and/or photometry. Depending on the degree of polarization of the observed target, polarimetry can increase the sensitivity of an instrument by a factor of at least four orders of magnitude (10^4), and it can be combined with modern coronagraphs and AO systems to reach even higher contrast ratios. One of the most promising instruments onboard of the future european extreme large telescope (E-ELT) is EPICS (Vérinaud & EPICS

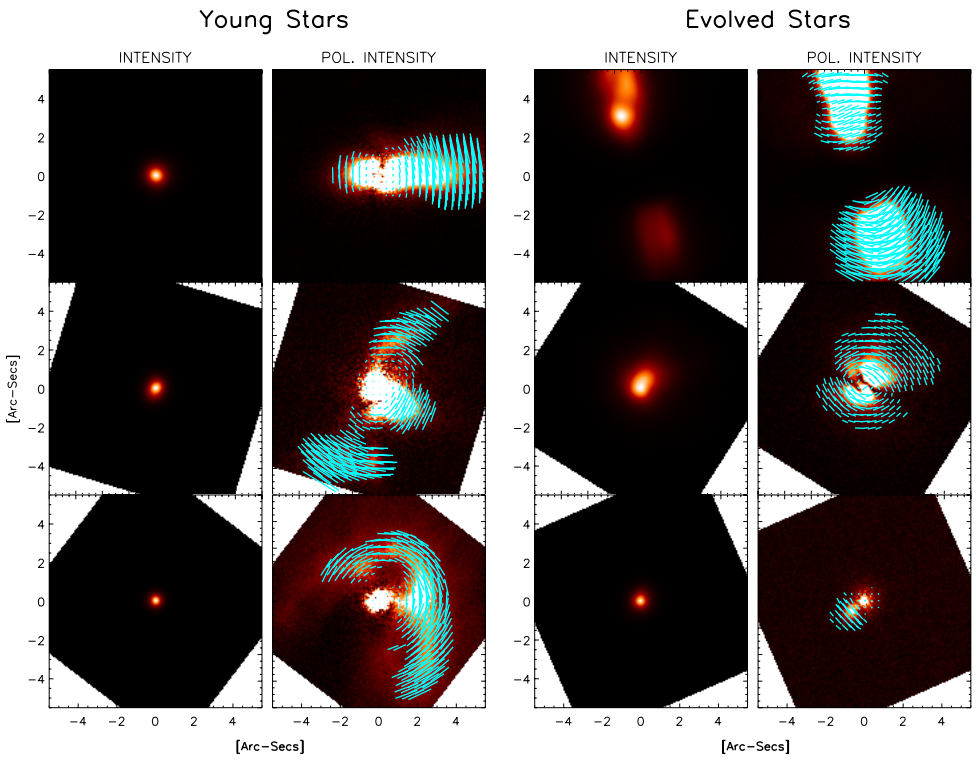

Figure 1.4: Examples of ExPo observations. Each image has been scaled to enhance its polarized features. The polarization angle is indicated by the blue-green vectors. Left Images: Some of the protoplanetary disks observed with ExPo. Top row: SU Aurigae, a T Tauri star. Center Row: the star T Tauri. Bottom row: MWC 147, a Herbig Ae star. Right images: some of the evolved stars observed during the fourth campaign of ExPo. Top row: AFGL 2688, the "Egg Nebulae". Center row: the Carbon star CW Leo. Bottom row: the star RCrB.

Team 2010, Vérinaud et al. 2010), which will make use of polarimetry to detect and characterize exoplanetary systems. Modern instruments such as HiCiao (Suzuki et al. 2009, 2010) at the Subaru telescope are already making use of a polarimeter, and future instruments such as SPHERE (Beuzit et al. 2010, Mesa et al. 2011), at the VLTs, and GPI (Graham et al. 2007) at the Gemini telescope will also introduce a polarimetric mode in their modus operandi.

Furthermore, polarimetry is ubiquitous in the Universe. It can be produced by very different physical mechanisms, such as synchrotron radiation, dichroism or Thompson scattering, to mention a few of them. Moreover, polarized light is produced at all wavelengths, from gamma rays to radio waves. Apart of circumstellar environments, which are the object of study in this thesis, polarimetry is used nowa-

days in completely different branches of astrophysics, as cosmology[4], black holes[5] or solar physics[6].

ExPo has proven to be an excellent instrument to observe circumstellar environments in general. Future versions of this instrument will include an AO system and an IFU, which will provide with higher quality and extremely exciting new results.

[4]the PLANCK satellite will study the polarization of the Cosmic Microwave Background.
[5]For instance, the future satellite GEMS will look at the X-rays polarized mission from black holes.
[6]As mentioned before, polarimetry has been used in Solar Astrophysics since long time ago.

It is a capital mistake to theorize before one has data. Insensibly one begins to twist facts to suit theories instead of theories to suit facts.
— Sherlock Holmes (Arthur Conan Doyle)

Chapter 2

Data-reduction techniques for high-contrast imaging polarimetry

H. Canovas, M. Rodenhuis, S. V. Jeffers, M. Min and C. U. Keller *

Abstract

Imaging polarimetry is a powerful tool for detecting and characterizing exoplanets and circumstellar environments. Polarimetry allows a separation of the light coming from an unpolarized source such as a star and the polarized source such as a planet or a protoplanetary disk. Future facilities like SPHERE at the VLT or EPICS at the E-ELT will incorporate imaging polarimetry to detect exoplanets. The Extreme Polarimeter (ExPo) is a dual-beam imaging polarimeter that can currently reach contrast ratios of 10^5, enough to characterize circumstellar environments. We present the data-reduction steps for a dual-beam imaging polarimeter that can reach contrast ratios of 10^5. The data obtained with ExPo at the William Herschel Telescope (WHT) are analyzed. Instrumental artifacts and noise sources are discussed for an unpolarized star and for a protoplanetary disk (AB Aurigae). The combination of fast modulation and dual-beam techniques allows us to minimize instrumental artifacts. A proper data processing and alignment of the images is fundamental when dealing with high contrasts. Imaging polarimetry proves to be a powerful method to resolve circumstellar environments even without a coronagraph mask or an Adaptive Optics system.

*Published in *Astronomy & Astrophysics*, 531, 102 (2011), reproduced with permission © ESO

2.1 Introduction

The direct detection and characterization of exoplanets is one of the main goals of the next generation of instruments and telescopes, such as the E-ELT (Hook 2009). Despite the increasing amount of detected exoplanets (e.g., *http://www.exoplanet.eu/*), only a few of them have been directly imaged (Marois et al. 2008b, Kalas et al. 2008, Lagrange et al. 2010, Todorov et al. 2010).

Polarization is a powerful tool for detecting and characterizing circumstellar environments, such as protoplanetary disks, debris disks, and exoplanets (Kuhn et al. 2001, Stam et al. 2005, 2006). While the light coming from the star is largely unpolarized, the scattered light from exoplanets and circumstellar environments is highly (linearly) polarized. This makes it easy to separate the planet signal from the unpolarized starlight, and reach the required high contrast ratios.

Future exoplanet instruments such as SPHERE (Thalmann et al. 2008), GPI (Graham et al. 2007) or EPICS (Vérinaud & EPICS Team 2010) will include imaging polarimetry, spectropolarimetry, or both, to characterize exoplanets. To reach the high contrast ratios that are necessary to detect an exoplanet, these instruments will combine coronagraphs, Adaptive Optics, and polarimetry. The combination of the firsts two elements can reduce the stellar light by a factor of 10^6 (Martinez et al. 2010), while polarimetry alone can reach contrast ratios of 10^5 (Rodenhuis et al. 2011a). The identification of instrumental artifacts and spurious signals that appear at these extremely high ratios is fundamental for understanding the data produced by the new generation of exoplanet imagers.

ExPo is a dual-beam imaging polarimeter that combines speckle imaging with dual-beam techniques, currently reaching contrast ratios of 10^5 without a coronagraph or adaptive optics system (Rodenhuis et al. 2008a, 2011a). The sensitivity reached by this instrument allows us to image circumstellar environments such as protoplanetary disks or dust shells with unprecedented accuracy (e.g. Canovas et al. 2011a,b)

In this paper we present the data-reduction approach for high dynamic range polarimetry. The whole data-reduction process is shown in Fig. 2.1. Results show that the dual-beam technique effectively minimizes systematic errors, leading to sensitive polarization measurements of different circumstellar environments.

In the following sections, the instrument is briefly described, followed by the analysis of the instrumental artifacts. The image-reduction process and a discussion of first results are presented at the end. Preliminary results of the well-known protoplanetary disk AB Aurigae and the diskless star HD12815 are shown.

2.2 Instrument description

ExPo is a dual-beam imaging polarimeter that currently reaches contrast ratios of 10^5. It is designed to characterize circumstellar environments, such as the disks around Herbig Ae/Be and T Tauri stars. ExPo is currently a visitor instrument at the William

Herschel Telescope (WHT), where it has been used for four successful observing campaigns.

ExPo has a wavelength range from $400-900$ nm, and its field of view is $20'' \times 20''$. It works with exposure times of 0.028 seconds to minimize the effects of atmospheric seeing. Systematic errors are minimized by modulating two opposite polarization states. The combination of dual-beam, short exposures times and polarization modulation allows us to reach contrast ratios of 10^5 without the aid of Adaptive Optics (AO) or coronagraphs.

As a dual-beam instrument, the incoming beam of light is divided into two orthogonally linearly polarized beams. As a result of this, two simultaneous images with opposite polarization states can be recorded on the CCD at the same time.

The schematic layout of the instrument is shown in Fig. 2.2. The light beam enters the instrument from the left. The dispersion introduced by the atmosphere (e.g., Wynne 1993) is reduced by an atmospheric dispersion corrector (ADC). The field stop prevents beam overlap on the detector. The filter wheel contains broadband and narrowband filters as well as an opaque filter to obtain dark measurements. The polarization compensator minimizes the instrumental polarization introduced by the telescope. The light beam is currently modulated by a single ferroelectric liquid crystal (FLC), which switches between two states (A and B) with orthogonal polarization states. Future versions of this instrument may use an achromatic 3-FLCs Pancharatnam modulator (Pancharatnam 1955, Keller 2002), but this will not influence the data-reduction approach described here. The beamsplitter divides the incoming light into two beams (left and right) with perpendicular polarization states. These two beams are finally imaged onto the EM-CCD camera, which records two simultaneous images with orthogonal polarization states. During the observation, the whole instrument remains static, with only the FLC switching from one state to the other.

2.2.1 ExPo images

With the FLC in two different states, two different frames (A and B) are recorded. A total of four images (i.e., two images per frame, corresponding to the *left* and *right* beams) are produced for each FLC cycle: A_L, A_R, B_L, B_R, where the subscripts L and R stand for left and right, respectively. Owing to the FLC modulation, A_L and B_R contain the same polarization information, as happens to A_R and B_L. To account for all components of these images, we use the following notation:

$T_{A,B}$	FLC transmission
$T_{L,R}$	Beamsplitter transmission
$Flat_{AL,AR,BL,BR}$	Flat Fields
I, P	Intensity, Polarization images
PSF	Point Spread Function
N	Noise

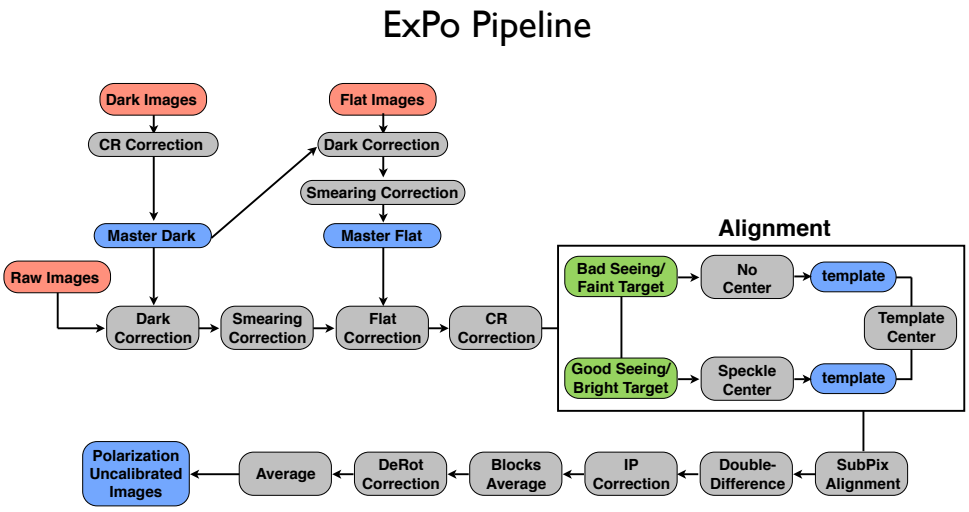

Figure 2.1: Pipeline Block Diagram.

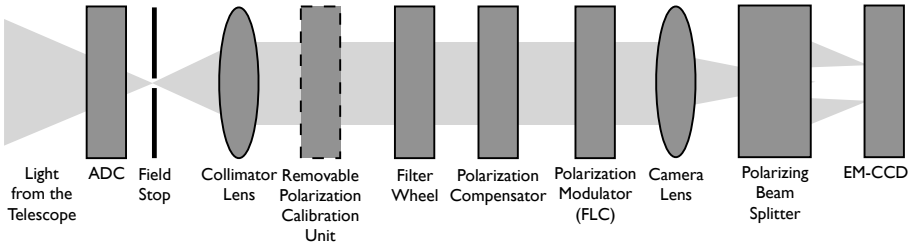

Figure 2.2: Schematic layout of the instrument in the Nasmyth focus of a telescope.

where $T_{A,B}$ accounts for the FLC transmission in its two possible states, and $T_{L,R}$ accounts for any transmission difference between the two beams. $Flat_{AL,AR,BL,BR}$ accounts for the different flat fields on the left and right sides of the CCD for the A and B images. The noise term includes the read-out and the photon noise. The polarization image includes any polarized light that enters the instrument, including sky polarization and polarization introduced by the telescope. The PSF can be expressed as the convolution of the "optics" and (PSF_{Opt}) and "seeing" (S) terms of the PSF (e.g. Roddier 2004):

$$PSF = PSF_{Opt} * S, \tag{2.1}$$

where $\mathrm{PSF_{Opt}}$ accounts for the static optical elements of the instrument and telescope, and S accounts for the dynamic atmosphere. Any small imperfection in the beam-splitter or difference in the optical path between the two beams will translate into different $\mathrm{PSF_{Opt}}$ for the left and right images: $\mathrm{PSF_L}$ and $\mathrm{PSF_R}$. On the other hand, the atmosphere will change with time, so S will also change for the A and B frames: S_A and S_B. Taking all of this into account, the four images recorded by the CCD in one FLC cycle can be described by

$$\begin{aligned} A_\mathrm{L} &= \mathrm{T_A} \cdot \mathrm{T_L} \cdot \mathit{Flat}_\mathrm{AL} \cdot 0.5 \cdot \Big((I+P) * \mathrm{PSF_L} * S_\mathrm{A} \Big) + N_\mathrm{AL} \\ A_\mathrm{R} &= \mathrm{T_A} \cdot \mathrm{T_R} \cdot \mathit{Flat}_\mathrm{AR} \cdot 0.5 \cdot \Big((I-P) * \mathrm{PSF_R} * S_\mathrm{A} \Big) + N_\mathrm{AR} \\ B_\mathrm{L} &= \mathrm{T_B} \cdot \mathrm{T_L} \cdot \mathit{Flat}_\mathrm{BL} \cdot 0.5 \cdot \Big((I-P) * \mathrm{PSF_L} * S_\mathrm{B} \Big) + N_\mathrm{BL} \\ B_\mathrm{R} &= \mathrm{T_B} \cdot \mathrm{T_R} \cdot \mathit{Flat}_\mathrm{BR} \cdot 0.5 \cdot \Big((I+P) * \mathrm{PSF_R} * S_\mathrm{B} \Big) + N_\mathrm{BR}, \end{aligned} \tag{2.2}$$

where A_L stands for the left image taken when the FLC is in its A state, and so on. N_{AL} refers to the noise associated with this image. Symbols "$\cdot$" and "$*$" stand for multiplication and convolution, respectively. The factor 0.5 comes from the beamsplitter: the total incoming beam is divided into two. A "pure" intensity image can then be generated by adding the left and right beams.

Once a data set is recorded, the FLC is rotated by 22.5°, and a new data set is acquired. Because ExPo does not have a de-rotator, the field rotation will rotate not only the image, but also the polarization plane of the incoming light. To avoid this, the images are calibrated according to the reference system of the observed target and are then transformed to the reference system of the instrument. The Stokes parameters Q and U are obtained after combining and calibrating (Rodenhuis et al. 2011a) four datasets with the FLC rotated by 0°, 22.5°, 45° and 67.5° (e.g. Patat & Romaniello (2006)). Two FLC positions (0° and 22.5° or 45° and 67.5°) are necessary to produce calibrated images, so two redundant data sets are obtained after calibrating. Random errors (e.g., uncorrected cosmic rays, FLC ghosts) are removed by comparing these two data sets.

2.3 Image preparation

In this section we describe the initial reduction steps that must be applied to the raw data. Once the images are corrected for dark, flat, and smearing effects, they are ready to be aligned and combined as explained in §4 and §5.

2.3.1 Dark reduction

A dark image is an image taken with a given exposure time and with the CCD shutter closed. However, this is not possible because of the short exposure times required by ExPo, as we will explain in the next subsection, and the CCD shutter must remain

open during the whole observation. An opaque filter is placed in the filter wheel to measure dark frames.

Every dark frame is checked to detect and remove cosmic rays (CR). They are identified as pixels showing values higher than a threshold value. This threshold is defined according to the characteristics of the dark observation, i.e., dark frames obtained with different CCD gain values will require different threshold values to detect the CR events. This process produces good results when reducing dark frames. Another approach is used when reducing the final science images, as is explained in §3.4. Finally, a very low-noise master dark is generated by combining at least 8000 dark frames (equivalent to a total integration time of roughly 4 minutes).

2.3.2 Smearing and second-order corrections

Owing to the short exposure times used by ExPo, the CCD runs in *frame-transfer* mode, which means that the detector is reading and recording frames at the same time. To achieve this, the CCD chip is split in half: one half for exposing and another half for reading. Once an image is recorded on the "exposing" half, it is shifted to the read-out area. The shutter remains open during the whole process, and this, unfortunately, introduces spurious effects that must be removed in the initial reduction of the raw images.

Each time a frame is transferred to the read-out area of the CCD, there is some leftover charge. As a result of this, an extra background is added to the next recorded frame. Moreover, if the observed target is too bright, a streak in the direction of the charge shifting will appear when exposing for a long time, or averaging many short-exposure images.

Owing to the field mask, some areas of the CCD are not illuminated (Fig. 2.3). Any signal measured in these non-illuminated regions must come either from the extra background mentioned above or from the read-out noise. The information contained in these "dark" pixels is used to remove these two effects. An example of this is shown in Fig. 2.4: the spurious signal is first measured outside of the field mask, and then subtracted from the raw image.

2.3.3 Flat reduction

A set of dome flats is taken at the beginning and the end of each observing night. A minimum number of 100 frames are recorded for each of the four FLC positions $(0°, 22.5°, 45°, 67.5°)$. Every frame is then corrected for dark and smearing effects. As with the images, it is convenient to distinguish between $Flat_{\mathrm{AL}}$, $Flat_{\mathrm{AR}}$, $Flat_{\mathrm{BL}}$ and $Flat_{\mathrm{BR}}$. Any polarization introduced by the dome lights, beamsplitter, and FLC transmission differences disappears when one normalizes each of these flats independently. All flat field images are combined to generate four master flats.

The analysis of the flat fields shows that the CCD has no dead pixels.

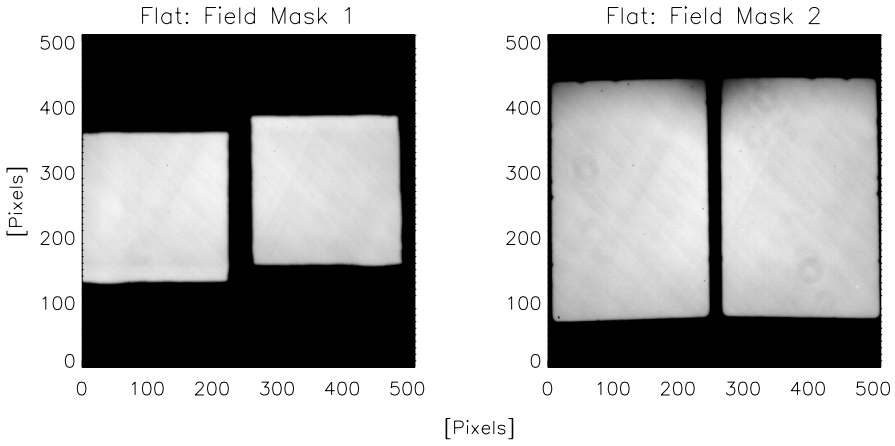

Figure 2.3: Normalized flat fields with two different field masks.

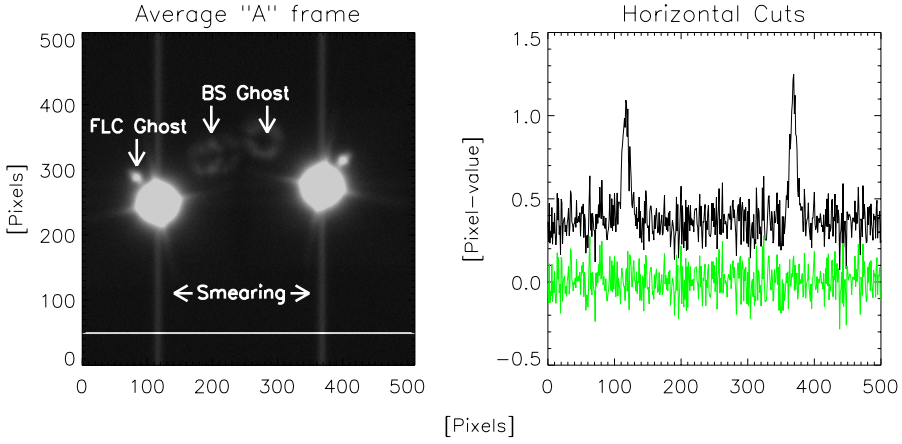

Figure 2.4: Left: Raw image, plotted at very high contrast. Two spurious ghosts can be seen above the star (discussed below in §6.4) The horizontal white line represents the plot that is shown on the right. Right: The black line shows the horizontal cut before the correction, the green line shows the smearing correction effect described in §3.2.

2.3.4 Cosmic ray correction

Before the images are combined and analyzed, they are corrected for cosmic rays. A standard ExPo data set comprises 20000 images (around 10 minutes exposure time) per FLC position. The CR contribution cannot be neglected because we are dealing with contrast ratios of $\approx 10^5$. Owing to the nature of the ExPo images, with very short exposure times and a FOV of $20'' \times 20''$, it is not trivial to distinguish between a real speckle and a CR. Standard CR rejection methods are based on comparing

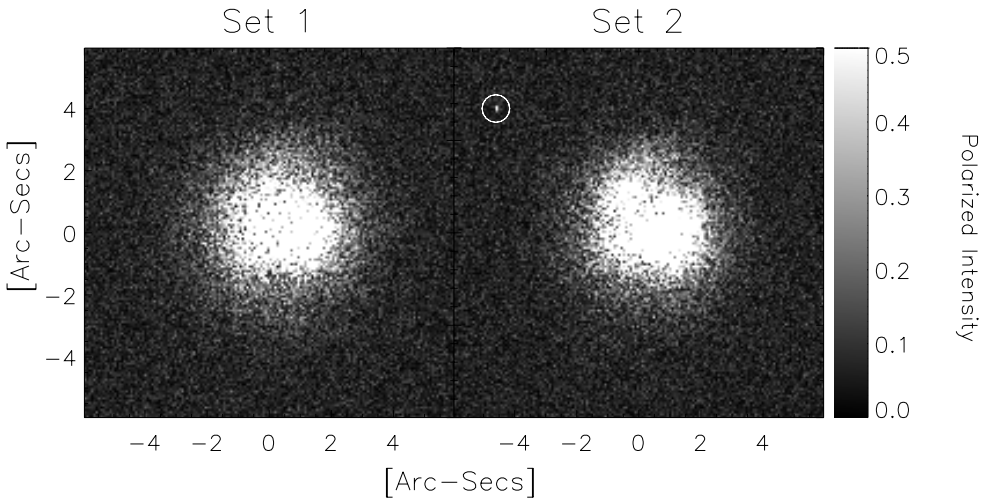

Figure 2.5: Polarized images of AB Aurigae (seeing was ~ 1.4″). Set 1 shows a calibrated image generated with the FLC placed at 0° and 22.5°. Set 2 shows the polarized image generated after placing the FLC at 45° and 67.5°. The white circle shows the position of a cosmic ray that does not appear in the first image.

an average image with the individual ones, and then applying a sigma-rejection algorithm. However, the speckle pattern disappears in the average; the average and individual images are indeed quite different. A different approach, based on the advantage of having two simultaneous images in the same frame, is used in this analysis. A box of 5×5 pixels is extracted around the brightest pixel of the left and right images. The standard deviations (σ) of these two boxes are then compared. Experimental results show that if the brightest pixel corresponds to a CR and not to a speckle, its associated σ will be at least three times greater than the σ of a true speckle. Cosmic rays are detected and corrected according to this threshold: if one of the boxes contains a CR, all its pixels are set to the mean value of the whole image.

If both the left and right images are affected by CRs, this method will still work because the probability that the cosmic rays have the same standard deviation is very low. Fainter CR can be divided into two categories: those that fall inside the speckle pattern and those that fall outside of it. The former are, in practice, impossible to distinguish from true speckles. The latter are removed from the final images at the end of the analysis. Figure 2.5 shows an example of this process: one uncorrected CR appears in one set but not on the other, so it can be easily identified and removed from the final image.

2.4 Image alignment

Once these corrections are applied, the images are aligned before they are combined. During the image acquisition, the telescope guides on the observed target (i.e., there is no *reference star* to be tracked). As a result of this, the accuracy of the guiding decreases, specially in the fainter ($m_v \geq 9$) targets. Because of the small field of view of ExPo, any small telescope misalignment can shift the image center by several pixels. Additionally, owing to the short exposures used, the PSF is a speckle pattern. All these contributions make image alignment one of the main sources of error in the processing of ExPo data. To reduce misalignment effects, two centering algorithms were tested: brightest speckle and template cross-correlation.

The brightest speckle-method (or shift-and-add method) is used in lucky imaging (e.g., Law et al. 2006). The images are aligned according to the position of the brightest speckle in each image.

The template cross-correlation method first requires a starting template or reference image. Once the template is provided, each single image is cross-correlated with it. The image center is now defined as the position of the maximum value of this operation. Different templates such as a simulated Gaussian-shaped point spread function (PSF) or an average speckle-centered real PSF were used in these calculations.

Once the images are centered, and before they are combined, they are again aligned to minimize any other source of misalignment, such as sub-pixel or flat-field gradients. These effects are corrected with a custom version of the drizzle code of Fruchter & Hook (2002). In this code, each pixel is expanded into several pixels, making it possible to shift and align images with sub-pixel accuracy.

The analysis shows that the best results are obtained when combining these three methods. First, a template is generated by centering each left and right image according to the brightest speckle. An average non-Gaussian shaped PSF is generated after combining all these images. Then, this PSF is used as the input template for the second method: each individual image is now cross-correlated with this template. Finally, each 'right' image is aligned with respect to the 'left' one by using the drizzle code. Each pixel is subdivided into nine sub-pixels, which results in an alignment accuracy of a third of a pixel. Any shift introduced by the FLC is also corrected by this centering process.

To check how misalignment affects the data reduction, several unpolarized (diskless) stars were analyzed. In these cases, no polarization pattern is expected to be measured. The accuracy of the alignment can be quantified in terms of the standard deviation σ of this pattern. Figure 2.6 shows the polarization pattern measured for the unpolarized star HD122815. The top row shows the difference between the template-center and the speckle-center. The bottom row shows the same result, but now including sub-pixel alignment with a third of a pixel accuracy. The combination of template center plus sub-pixel alignment shows almost no structure at all (Fig. 2.6, lower-left corner).

From Fig. 2.6 it is clear that most of the misalignment disappears when aligning

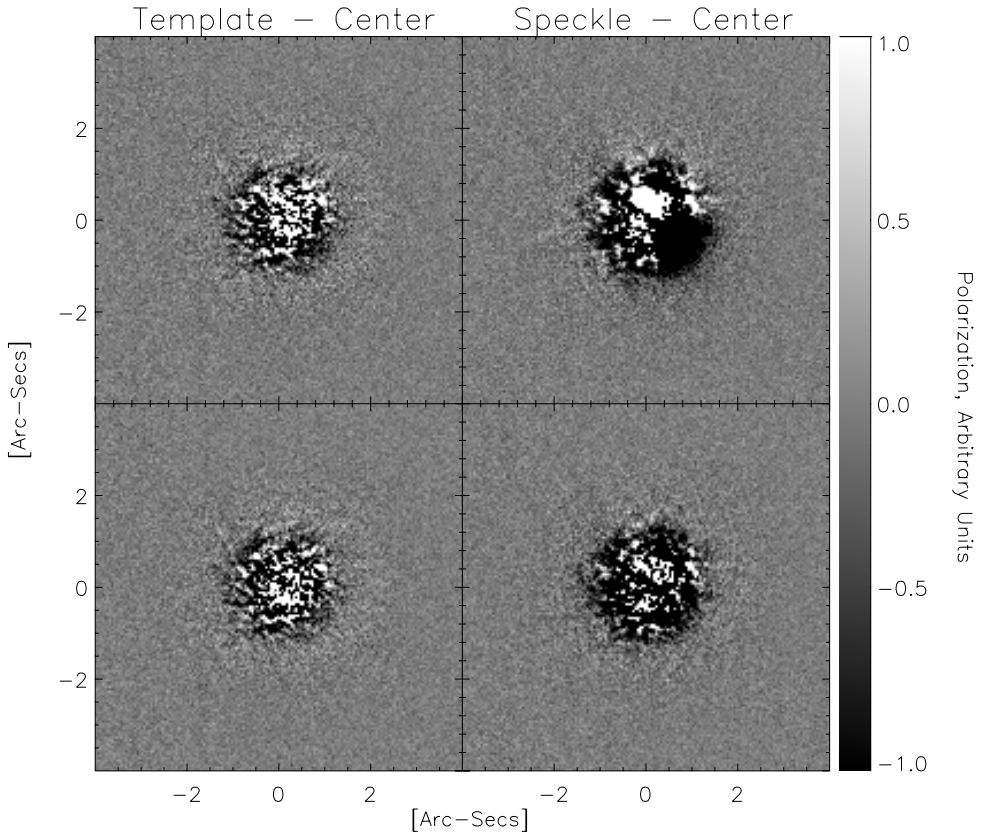

Figure 2.6: Polarized (uncalibrated) results for a diskless (unpolarized) star: HD122815. Four different alignment approaches are shown. Left column: images are aligned with a template. Right column: images re aligned according to the brightest speckle (shift-and-add). Top row: No sub-pixel alignment. Bottom row: sub-pixel alignment. Color bar: amount of (uncalibrated) polarization, P.

the images according to the cross-correlation method. No significant improvement is detectable when aligning with sub-pixel accuracy because of the lack of structure in a diskless star.

2.5 Image combination

As described by Bagnulo et al. (2009a), there are two methods of combining images produced with a dual-beam polarimeter to produce polarization images: one based on the image *ratios* and the other based on the image *differences*. For ExPo, these two

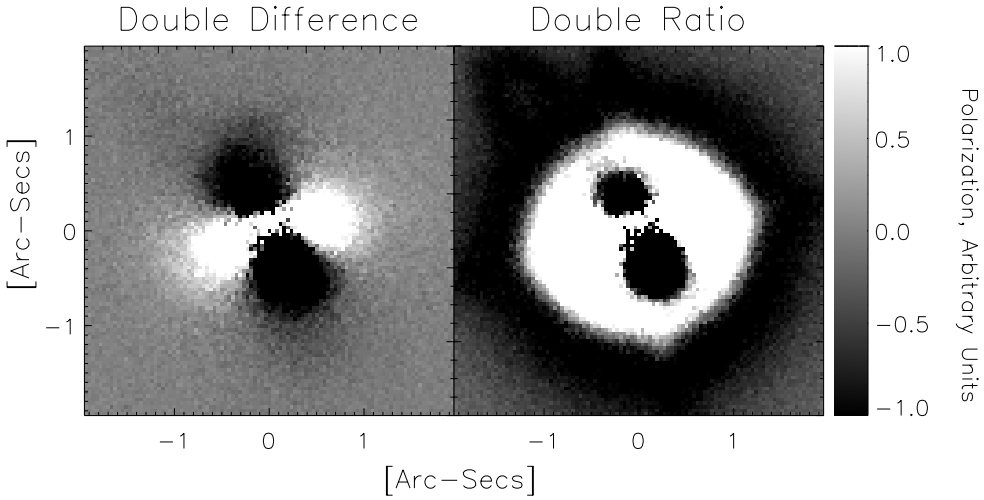

Figure 2.7: AB Aurigae images obtained after applying the double difference (left) and double ratio (right). Color Bar: amount of (uncalibrated) polarization, P.

approaches can be expressed in terms of Eq. 2.2 as

$$P = 0.25 \cdot \left(\frac{A_{\rm L}}{B_{\rm L}}\frac{B_{\rm R}}{A_{\rm R}} - 1\right) \cdot 0.5 \cdot (A_{\rm L} + A_{\rm R} + B_{\rm L} + B_{\rm R}) \tag{2.3}$$

for the *double-ratio* method, and as

$$P = 0.5\,(P_{\rm A} - P_{\rm B}) = 0.5\,((A_{\rm L} - A_{\rm R}) - (B_{\rm L} - B_{\rm R})) \tag{2.4}$$

for the *double-difference* method. Both methods were investigated. The results prove that better results are obtained when applying the *double-difference* method instead of the *double-ratio* explained in detail in Keller (1996) and Donati et al. (1997). This result is shown in Fig. 2.7, where the same data set was reduced applying the *double-differences* method (left) and the *double-ratio* method (right). This can be explained by the difference of the speckle pattern for each image. Even though $A_{\rm L}$ and $A_{\rm R}$ are recorded simultaneously, they show small differences in their speckle patterns from instrumental effects. Owing to the huge dynamic range of our images, the slightest difference between two images will produce a big effect when calculating a ratio. However, the difference method is less sensitive to this. Therefore, this method was chosen for ExPo. At this point the dual-beam + beam-exchange technique shows its advantages. The combination of the four images generated in each FLC cycle minimizes the systematic errors. Following the notation introduced in §2, all terms that appear when developing the equations are listed in Table 2.1. Once the images are corrected for dark, flat, and smearing effects, the following *differences* can be defined:

$$\Delta A = 0.5 \cdot {\rm T_A} \cdot \{I * \delta_{\rm I} + P * \delta_{\rm P}\} * S_{\rm A} + \Delta N_{\rm A}, \tag{2.5}$$

Notation	Expression
ΔA	$A_{\rm L} - A_{\rm R}$
ΔB	$B_{\rm L} - B_{\rm R}$
ΔL	$A_{\rm L} - B_{\rm L}$
ΔR	$A_{\rm R} - B_{\rm R}$
$\delta_{\rm I}$	$\mathrm{T_L} \cdot \mathrm{PSF_L} - \mathrm{T_R} \cdot \mathrm{PSF_R}$
$\delta_{\rm P}$	$\mathrm{T_L} \cdot \mathrm{PSF_L} + \mathrm{T_R} \cdot \mathrm{PSF_R}$
$\delta_{\rm I}^{'}$	$\mathrm{T_A} \cdot S_{\rm A} - \mathrm{T_B} \cdot S_{\rm B}$
$\delta_{\rm P}^{'}$	$\mathrm{T_A} \cdot S_{\rm A} + \mathrm{T_B} \cdot S_{\rm B}$
$\Delta N_{\rm A}$	$N_{\rm AL} - N_{\rm AR}$
$\Delta N_{\rm B}$	$N_{\rm BL} - N_{\rm BR}$

Table 2.1: Notation used during the development of the image analysis.

$$\Delta B = 0.5 \cdot \mathrm{T_B} \cdot \{I * \delta_{\rm I} - P * \delta_{\rm P}\} * S_{\rm B} + \Delta N_{\rm B}, \tag{2.6}$$

where $\delta_{\rm I}$ and $\delta_{\rm P}$ refer to differences between the left and right beams. The difference between $\mathrm{T_L}$ and $\mathrm{T_R}$ produces a bias between left and right images, while the difference between $\mathrm{PSF_L}$ and $\mathrm{PSF_R}$ differentially distorts the images. If the beamsplitter does not produce two identical beams (i.e., from optical imperfections) $\delta_{\rm I}$ will be non-zero. Because ExPo looks for polarized intensities of $P \approx 10^{-5} I$, this term should be on the order of $\approx 10^{-4}$ or smaller, as will be explained in the next paragraphs. As soon as this condition is not satisfied, the polarization values will be affected by the uncorrected intensity differences.

To evaluate the effect of $\delta_{\rm I}$ on the polarimetry results, two average intensity "left" and "right" images were produced by averaging left and right beams: $I_{\rm L} = A_{\rm L} + B_{\rm L}, I_{\rm R} = A_{\rm R} + B_{\rm R}$. Both images were aligned with a third of a pixel accuracy, then normalized, and finally subtracted. The noise contribution can be neglected in this calculation because its contribution is several orders of magnitude below the intensity level. The result is described by

$$I_{\rm L} - I_{\rm R} = (I * \delta_{\rm P}^{'} + P * \delta_{\rm I}^{'}) * \delta_{\rm I}, \tag{2.7}$$

where $\delta_{\rm I}^{'}$ and $\delta_{\rm P}^{'}$ refer to any difference between the A and B frames. The difference between $\mathrm{T_A}$ and $\mathrm{T_B}$ will affect the whole image like a bias value, and the difference between $S_{\rm A}$ and $S_{\rm B}$ will affect the image shape. The later will be averaged out when combining enough images, i.e., the *seeing* effect will affect the A and B frames in the same way. Ferroelectric liquid crystal transmission differences are not higher than 10^{-3} for our current FLC (Rodenhuis et al. 2011a), therefore $\delta_{\rm I}^{'} \approx 10^{-3}$, and $\delta_{\rm P}^{'}$ will be very close to unity $\delta_{\rm P} \approx 1$. Taking all of this into account, the first term of Eq. 2.7 is much larger than the second term: $I * \delta_{\rm P}^{'} \gg P * \delta_{\rm I}^{'}$, so Eq. 2.7 becomes

$$I_{\rm L} - I_{\rm R} \approx I * \delta_{\rm I}. \tag{2.8}$$

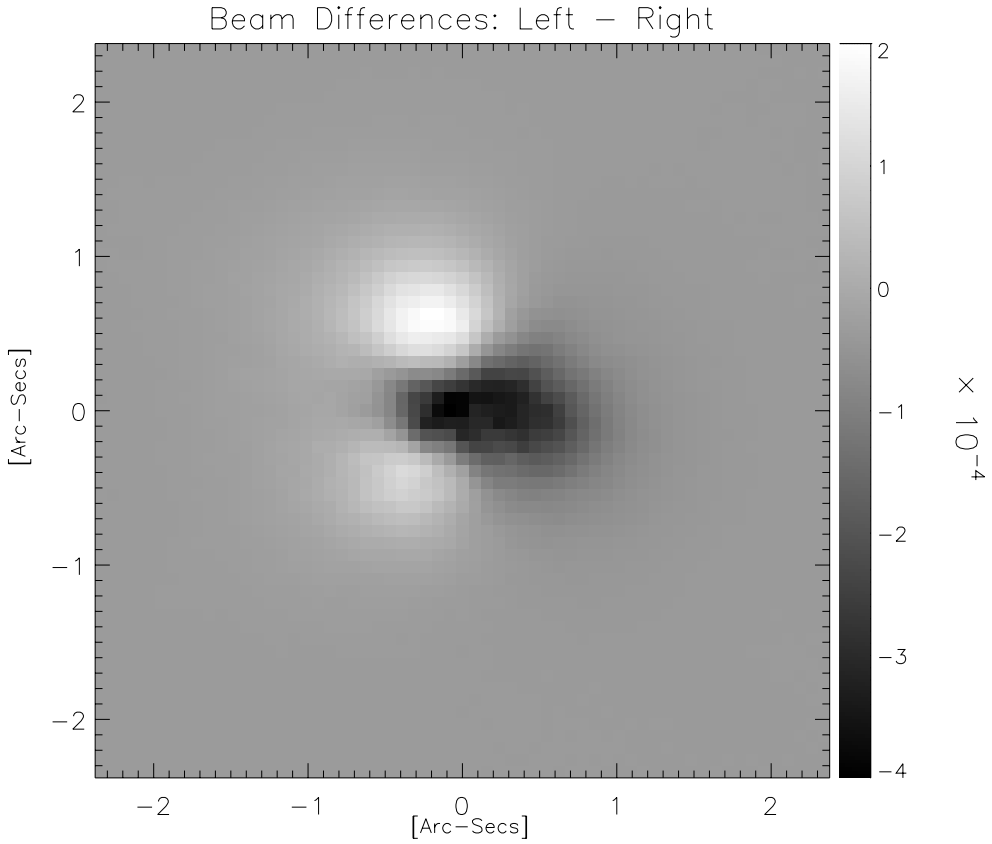

Figure 2.8: Normalized difference between left and right beams. The asymmetrical pattern around the center means *shape* differences (i.e., $\mathrm{PSF_L}$ and $\mathrm{PSF_R}$ produce different patterns). The color bar is in units of 10^{-4}, meaning that this is the magnitude of the beam differences.

Figure 2.8 illustrates this result for the diskless star HD122815, observed with the FLC oriented at 0°. The image is scaled to its maximum, i.e., the beam differences have an amplitude of $\approx \pm 4 \cdot 10^{-4}$, which means that this is the magnitude of δ_I. Similar values are found when repeating this experiment for different FLC orientations. As can be clearly seen from these results, beamsplitter imperfections are an important effect that needs to be taken into account when dealing with contrast ratios of 10^4 or higher. Any differences in the PSF of each beam can modify the final result when aiming for such high contrast ratios. This contribution is, however, minimized when working with the *double-difference* method:

$$\sum_i^n (\Delta A - \Delta B) = \sum_i^{n/2} \left(I * \delta_{\mathrm{I}} * \delta_{\mathrm{I}}^{'} + P * \delta_{\mathrm{P}} * \delta_{\mathrm{P}}^{'} + \Delta N_{\mathrm{A}} - \Delta N_{\mathrm{B}} \right). \tag{2.9}$$

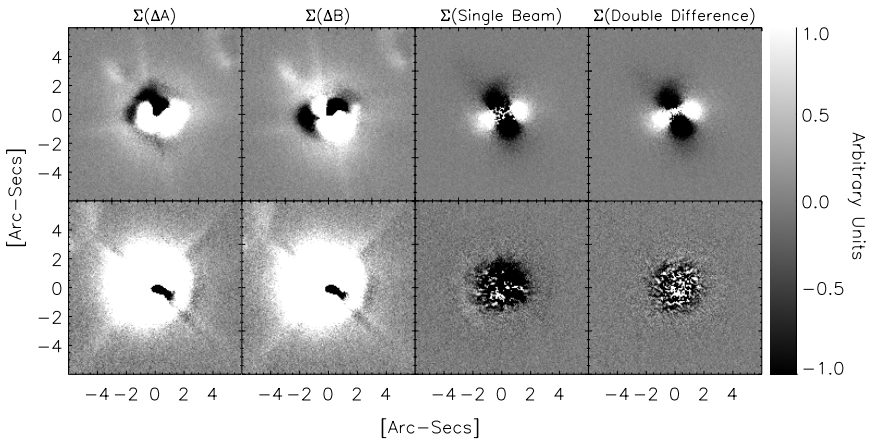

Figure 2.9: Uncalibrated polarized image. Top rows: AB Aurigae. Bottom rows: Unpolarized star. Color bar: (uncalibrated) polarization, P (arbitrary units). The results plotted in the left and center columns are contaminated by instrumental artifacts. These artifacts are minimized when applying the *double-difference*, as is shown in the right column.

In this case, the four images produced in each FLC cycle are first combined, and then averaged over the whole data set. Now the intensity term is convolved with the convolution of δ_I and $\delta_I^{'}$. The latter will have a magnitude of $\delta_I * \delta_I^{'} \approx 10^{-7}$, so the intensity will be decreased by this factor. Both δ_P and $\delta_P^{'}$ are close to unity, so their convolution will be also close to unity. The polarization term is then neither increased nor decreased. Finally, the noise term is not modulated by any *delta* factor. Its contribution is minimized by the *double-difference* and it will be averaged out. This term will define the maximum contrast attainable with ExPo.

Figure 2.9 summarizes the previous results for both a diskless star (HD122815) and a protoplanetary disk (AB Aurigae). The first two columns starting from the left show the result given by Eq. 2.5 and Eq. 2.6, respectively, when applied to these two targets. The result of a *single-beam* experiment is shown in the third column. In this case, the images produced by just one beam (the right one) are shown for comparison. The result of the *double-difference* described by Eq. 2.9 is shown in the right column. In the first and second columns the polarization pattern is contaminated by the intensity term described by δ_I, and the third column shows that the images are more noisy. The fourth column has no artifacts, showing a clean polarization pattern, with the lowest noise level.

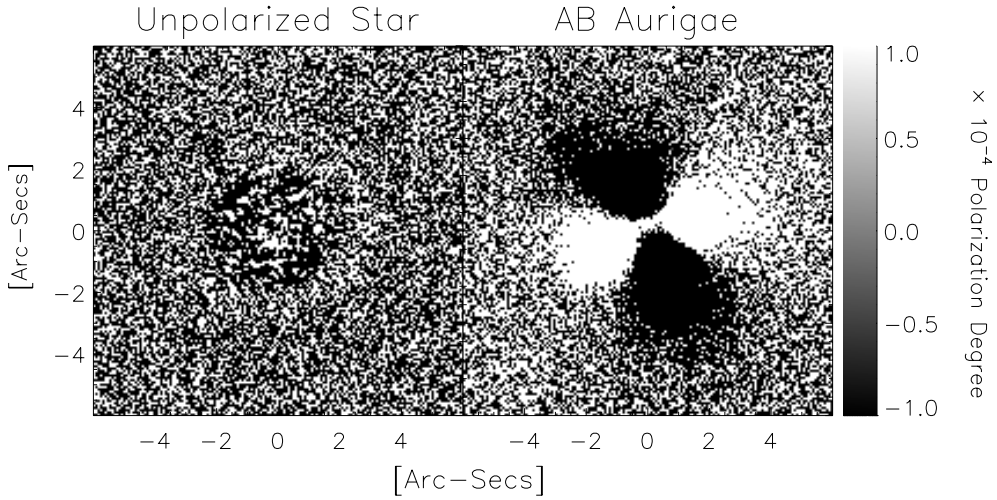

Figure 2.10: Polarization degree for the unpolarized (diskless) star HD122815 (left), and for AB Aurigae (right).

2.6 Additional corrections

2.6.1 Instrumental polarization

The polarized light measured by ExPo not only contains the polarized light coming from the circumstellar environment, but also telescope polarization (Miller 1963) and interstellar polarization (Hiltner 1949). Moreover, any small difference between the beamsplitter transmission coefficients (T_A, T_B) or the FLC transmission coefficients (T_L, T_R) introduces an artificial polarization signature. All these contributions are proportional to the intensity of the incoming light, so their effects can be measured by measuring the degree of polarization at the center of the (largely unpolarized) star. The polarization compensator used by ExPo minimizes these effects, but there is always some leftover instrumental polarization. Taking into account that $A_L + A_R \approx T_A \cdot S_A * I * \delta_P$, and $B_L + B_R \approx T_B \cdot S_B * I * \delta_P$, the polarization degree at the star's center for the A frame can be described as

$$\left.\frac{A_L - A_R}{A_L + A_R}\right|_{center} \approx \frac{\delta_I}{\delta_P} + \frac{P^i}{I} = A_{Bias}, \tag{2.10}$$

and for the B frame:

$$\left.\frac{B_L - B_R}{B_L + B_R}\right|_{center} \approx \frac{\delta_I}{\delta_P} - \frac{P^i}{I} = B_{Bias}. \tag{2.11}$$

P^i refers to any polarization feature that does not come from the circumstellar environment. As explained in Rodenhuis et al. (2011a), the polarization compensator is

working for all observations (including unpolarized diskless stars), and it is impossible to set a true zero or reference level for our polarimetric observations. Therefore, all calculations are based on the assumption that the starlight is unpolarized. However, this is not true if there is a circumstellar disk with strong inner disk polarization (Min et al. 2011a). In these cases, a degree of polarization on the order of a few per cent is expected to be measured at the star's position. On the other hand, the expected instrumental polarization is a few percent as well, so in practice it is impossible to distinguish inner disk polarization from instrumental polarization. The $A_{\rm Bias}$ and $B_{\rm Bias}$ are then subtracted from the *degree of polarization* for the A and B frames:

$$\frac{P_{\rm A}}{I_{\rm A}} = \frac{A_{\rm L} - A_{\rm R}}{A_{\rm L} + A_{\rm R}} - A_{\rm Bias}, \tag{2.12}$$

$$\frac{P_{\rm B}}{I_{\rm B}} = \frac{B_{\rm L} - B_{\rm R}}{B_{\rm L} + B_{\rm R}} - B_{\rm Bias}, \tag{2.13}$$

where $dP_{\rm A}$ and $dP_{\rm B}$ are the instrumental polarization-corrected degree of polarization for the A and B frames, respectively. The (uncalibrated) polarization image $P_{\rm A}$ is then calculated as the product of the degree of polarization times the intensity:

$$P_{\rm A} = \frac{P_{\rm A}}{I_{\rm A}} \cdot (A_{\rm L} + A_{\rm R}), \tag{2.14}$$

$$P_{\rm B} = \frac{P_{\rm B}}{I_{\rm B}} \cdot (B_{\rm L} + B_{\rm R}). \tag{2.15}$$

Figure 2.11 shows the effect of this correction. An artificial bias appears in the polarization images when the IP correction is not applied. If the star is unpolarized (bottom row), a bias level appears as a consequence of the imperfect compensation. In the case of AB Aur (top row) the polarization pattern is distorted when no correction is applied.

2.6.2 Field rotation

All alt-azimuth telescopes are affected by *field rotation*. This term describes the amount of sky rotation, and it depends on the altitude (h) and azimuth (a) of the observed target, as well as on the latitude (ϕ) of the observer. It will reach its maximum value when pointing toward the zenith, and it will be almost negligible when pointing to very low altitudes. If the observations are made at the Nasmyth focus, an extra rotation must be taken into account, caused by the relative rotation between the telescope tube and the Nasmyth platform (see Marois et al. 2006, Joos 2007, chapter 4):

$$\dot{G} = \frac{\cos\phi \cdot \cos a}{\cos h} \cdot \omega_0, \tag{2.16}$$

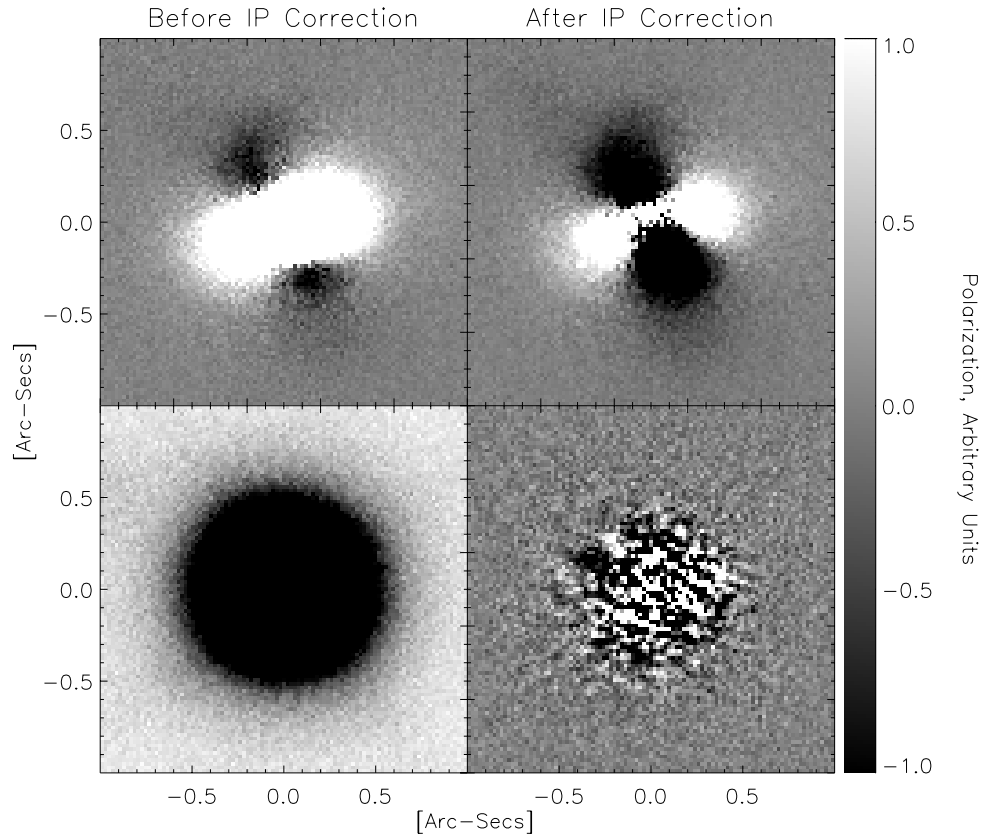

Figure 2.11: Effect of the instrumental polarization (IP) on the final images. Top: AB Aurigae. Bottom: Unpolarized star. Color bar: Polarization (P), arbitrary units.

$$\dot{H} = -\sin a \cdot \cos \phi \cdot \omega_0, \tag{2.17}$$

$$\dot{F} = \dot{G} \pm \dot{H}, \tag{2.18}$$

were ω_0 is the *sidereal rate*. $\dot{G}$ represents the rotation rate caused by the sky movement, and $\dot{H}$ accounts for the rotation rate caused by the telescope movement. Equation 2.18 is the total amount of field rotation rate at the Nasmyth platform. The ± is related to the two platforms at the telescope. In the case of ExPo, the instrument has been placed at the "B" platform of the William Herschel Telescope, so the "+" applies.

While most of the instruments incorporate a de-rotator to remove this effect, the design of ExPo does not include one. It is necessary to calculate $\dot{F}$ and then

numerically rotate each observed target. Owing to the short exposure time of the ExPo images, the amount of de-rotation between one image and the next image is too small to correct ($\leq 0.5^\circ$), so rotating each frame individually is not necessary. A rotation *per image blocks* is performed instead. $\dot{F}$ is assumed to be constant within a certain interval. If the observed target is not close ($\leq 15^\circ$) to the Zenith, this interval can be set to 30 seconds. Otherwise, shorter time intervals must be taken to minimize errors. Different rotation routines were tested. To test this, different template images were first rotated and then de-rotated by using different codes. The standard deviation σ of the difference between the original template and the de-rotated version is a measurement of the accuracy of the rotation procedure. This analysis shows that the best results are obtained when the image is first resampled to one fifth of a pixel. The rotation is then performed with the IDL routine *rot*, using cubic interpolation.

2.6.3 Sky-background polarization

The polarization of the sky (Bailey et al. 2008) is variable, depending on the position of the target as well as the position of the Moon (because scattered moonlight is polarized). Unlike the instrumental polarization discussed in §6.1, this contribution does not depend on the brightness of the observed target, but it behaves like a polarization bias over the whole image. Therefore, the background polarization cannot be calculated by measuring the degree of polarization at the star's center. The background polarization is subtracted at the very last stage of the data analysis by measuring the polarization in the sky regions of the image. The median value of at least four different sky regions is calculated and subtracted from the reduced polarization images.

2.6.4 Ghosts

Three different sources of optical ghosts are identified in ExPo: the filters, the beam-splitter and the FLC. While the latter produces ghosts that move according to the FLC angle, the ghosts produced by filters and the beamsplitter remain in a fixed position (an example of these ghosts can be seen in Fig. 2.12). Filter ghosts are minimized by tilting the filters. All these ghosts appear are contrast ratios of 10^{-4}.

To analyze the effects caused by the ghosts on the polarized images, the mean and standard deviation (σ) was calculated around the position of the ghosts and around sky (empty) regions in the polarization images. This test was performed for several (ghost-affected) images, with the result that it is impossible to distinguish between ghosts and sky regions when looking at the polarized images, i.e., ghosts do not contribute to the polarization image any more than the sky background. However, special care has to be taken when looking at the degree of polarization of the images. In this case, because the ghost appears in intensity (at contrast ratios of $\sim 10^{-4}$), it can contribute to the degree of polarization.

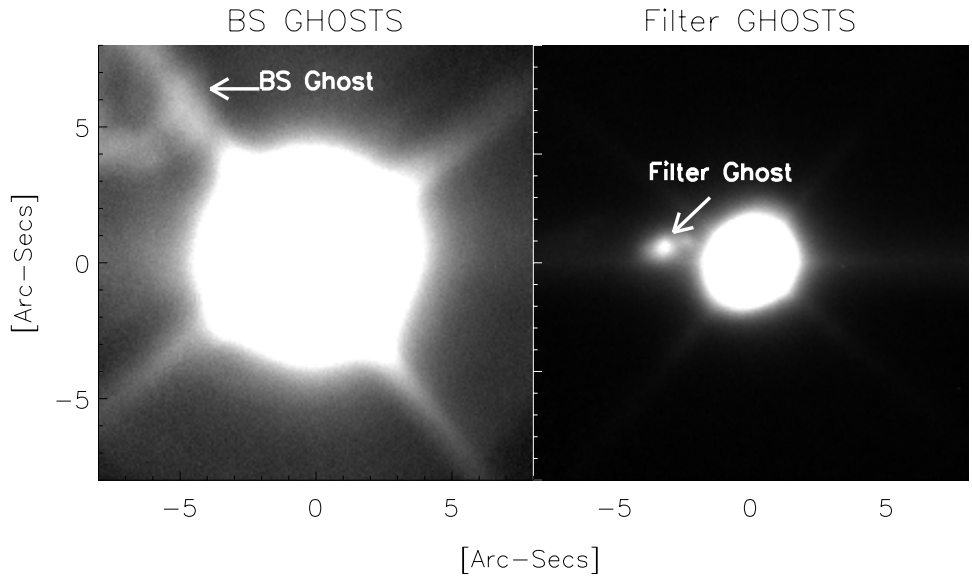

Figure 2.12: Intensity images of the same star observed without (left) and with (right) H_{acont} filter. The images are plotted at different contrast to enhance the ghost image. The diffraction caused by the telescope spiders is clearly visible in the left image.

2.7 Discussion

Flat-field errors (i.e., pixel-to-pixel sensitivity variations) are not limiting ExPo. Because each image is shifted individually before averaging, flat-field effects are averaged out. However, flat-field effects might play an important role when an AO system is added to the instrument. In this case, the PSF is expected to remain in a fixed position on the CCD, with no need to re-center the images.

Brightest-speckle alignment is not as good as template-alignment for our images. This result, which disagrees with previous work (Law 2006, Christou 1991), can be explained by the characteristics of this instrument. The small field of view used by ExPo combined with the four different PSFs generated in each FLC cycle makes a big difference with respect to the standard lucky-imaging observations. The speckle pattern produced by a single star is distributed over several pixels, and the beam differences make this pattern to be slightly different in the left and right images, even though they correspond to simultaneous observations. As a result of this, the brightest speckle on the left image is not necessarily the same as the brightest speckle on the right image. Therefore, the template center method produces better results than the speckle center method. However, in case of good *seeing* (below 0.7”), both methods converge, leading to very similar results. This can be explained by taking into account that in those cases, the PSF peak is concentrated in very few pixels, so

the region covered by the speckle pattern is very small. Under these conditions, the center defined by the template-center method and the brightest speckle are about the same.

While theoretically both the *ratio* and the *difference* method should produce similar results, this analysis shows that the first one fails when applied to a dual-beam imaging polarimeter like ExPo. The photon noise variance is signal-dependent, i.e., it is proportional to the amount of photons in each image. On the other hand, each image produced by this instrument is affected by a different combination of beamsplitter and FLC transmission coefficients, which means that the total amount of light in each of the four images produced in one FLC cycle is slightly different. This also applies to the photon noise, resulting in different levels of noise in each image. The *double-difference* minimizes this effect, while the *dual-ratio* can increase it. This is a particular result for this experiment, but it can be generalized to any dual-beam polarimeter.

Numerical simulations show that the bias correction described in §6.1 must be applied even when there is no instrumental polarization (Min et al. 2011a). The strong polarization produced by the inner rim of a protoplanetary disk dominates the polarized intensity, making it much harder to detect the remaining circumstellar polarization.

As mentioned in §2, future versions of ExPo may make use of 3 FLCs in a Pancharatnam configuration to minimize the chromatic effects introduced by the current single-FLC configuration. This change will not affect the current data-reduction process, but it will improve the instrument polarimetric performance.

The inclusion of an AO system in ExPo will lead to a much sharper PSF. The amount of speckles in these new PSFs will be considerably smaller than in our current PSFs. Real speckle-sized polarized features (i.e., exoplanets) might be removed as a result of the current CR rejection algorithm. One possible solution to this problem might be a new technique based on the comparison of the two *differences* (ΔA and ΔB) described by Eq. 2.5 and Eq. 2.6. A polarized speckle-sized feature such as an exoplanet is expected to appear in both images at the same coordinates, while in case of a CR, it will appear in only one of these differences.

Chromatic effects introduced by the FLC and the BS are outside the scope of this paper, but must be taken into account in future instruments such as SPHERE or EPICS.

Finally, lucky-imaging techniques (i.e., frame selection) do not produce significant improvements in our observations because the standard exposure time for a target is around one hour (around 20 minutes per FLC position). In this regime, the amount of "lucky images" is not enough to produce a good signal-to-noise ratio.

2.8 Conclusion

Dual-beam polarimeters are becoming more and more popular among the astronomical community, such as the ones described by Packham et al. (2005), Masiero

et al. (2008) and Nagaraju et al. (2008). The high contrast ratios achieved by polarimetry make this technique a promising tool to characterize exoplanets as well as circumstellar environments.

ExPo can currently reach contrast ratios of 10^5 at a four-meter class telescope by means of polarimetry. As we showed in this analysis, instrumental artifacts can be minimized by properly combining the data produced by a dual-beam instrument. The template-centering method produces better results than the speckle-centering method. The main limitations of the instrument are the beamsplitter imperfections and the FLC transmission differences, as explained in §5. Future versions of this instrument will include an Adaptive Optics system as well as a coronagraph, which will require new approaches to the data reduction.

Acknowledgments

We are grateful to the staff at the William Herschel Telescope for their support when commissioning of ExPo. We also thank the referee for his/her useful comments and recommendations.

All exact science is dominated by the idea of approximation.
— Bertrand Russell

Chapter 3

Imaging polarimetry simulations of protoplanetary disks

M. Min, H. Canovas, G. D. Mulders and C. U. Keller *

Abstract

Imaging polarimetry is a powerful tool to image faint circumstellar material. It is a rapidly developing field with great promises for diagnostics of both the large scale structures and the small scale details of the scattering particles. For a correct analysis of observations it is needed to fully understand effects of dust particle parameters as well as effects of the telescope, atmospheric seeing and assumptions about the data reduction and processing of the observed signal. Here we study the major effects of dust particle type, particle size, disk structure and telescope properties. We perform radiative transfer modeling using different dust particle models and disk structures. To study the influence of seeing and telescope diffraction we run the models through an instrument simulator for the ExPo dual-beam imaging polarimeter mounted at the 4.2m WHT. Particle shape and size have a strong influence on the brightness and detectability of the disks. In the simulated observations the central resolution element contains besides the unpolarized central star also contributions from the inner regions of the protoplanetary disk. This causes the central resolution element to be polarized making simple corrections for instrumental polarization difficult. This effect strongly depends on the spatial resolution, and adaptive optics systems are thus needed for proper polarization calibration.

For a proper analysis of the wealth of data available now or in the near future, it is needed to properly take into account the effects of particle types and disk structure. We find that the commonly employed homogeneous sphere model gives results that differ significantly from more realistic models. The observed signal depends strongly on the properties of these more realistic models, thus providing a potentially powerful diagnostic. We conclude that it is important to correctly understand telescope depolarization and calibration effects for a correct interpretation of the degree of polarization.

*Submitted to *Astronomy and Astrophysics*

3.1 Introduction

High spatial resolution imaging polarimetry is a rapidly developing field. It is now recognized that imaging polarimetry is a powerful tool for imaging faint matter around a bright star. Polarimetric differential imaging (PDI) is used to suppress the glare of the central star, which is unpolarized, to be able to see the faint reflected light from the material surrounding the star, which by scattering becomes polarized. This has already been successfully used to image circumstellar disks around young stars (see e.g. Close et al. 1997, Hashimoto et al. 2011), circumstellar dust shells around evolved stars (e.g Gledhill et al. 2001), and it is proposed for imaging the light reflected from exo-planets (Stam et al. 2004). Images in polarized intensity contain not only information on the geometry of the circumstellar material, but also carry information on the particles scattering the light from the central star. In the general case these two characteristics are intertwined and not easily separated.

Perhaps the most challenging case for interpreting polarimetric images is that of optically thick circumstellar disks around newly born stars. First, these disks are optically thick, causing multiple scattering, which alters the degree of polarization (see Dullemond et al. 2007b, for a review of the theoretical picture of the structures of protoplanetary disks). The geometry of the surface of these disks can cause scattering at unexpected angles, causing features in polarization (Perrin et al. 2009a). These effects can complicate the interpretation of polarimetric images in terms of planet-disk interactions. Besides these geometrical effects on a large scale a second complicating factor arises when these images are used to derive general information about the composing dust particles. Dust particles are expected to be highly complex in shape, and might be quite large in size. They are expected to be a mixture of small grains and large, complex fluffy aggregates (Dominik 2009). Computing the optical properties of such particles is very difficult and computationally demanding, if feasible at all. In addition, the different grain sizes are not expected to be well mixed with the gas, but size-dependent settling of the dust particles causes a size distribution of the grains that changes with height in the disk (Dullemond & Dominik 2004b). To conclude this chain of complications, dust properties, i.e. grain size and composition, are expected to vary radially (see e.g. van Boekel et al. 2004).

An additional complication is the effect of the finite resolution of real telescopes on the final image. The most powerful diagnostic, the degree of polarization of the scattered light, is highly influenced by the glare from the central star. Also, blurring of the high intensity, polarized, inner regions of the disk will affect the appearance of the disk in polarized intensity. Furthermore, data reduction techniques that correct for instrumental polarization using the central star as unpolarized calibration point might suffer from the non-zero innermost disk polarization.

In this paper we present computations of polarimetric images of protoplanetary disks around young, intermediate mass stars, so-called Herbig Ae stars. We study how the images depend on the properties of the disk and the composing dust particles. We vary the size of the dust particles, the geometry of the disk, and the shape of the dust particles. This is done using state-of-the-art models for the optical

properties of the dust particles, combined with a highly efficient radiative transfer code. A numerical simulation of ExPo (the *Extreme Polarimeter*, a dual-beam imaging polarimeter at a 4 m class telescope) is used to study the effects of atmospheric seeing and data reduction artifacts.

3.2 Computational approach

In this section we describe the setup of the models in terms of dust grains and disk geometry. The radiative transfer model used to create the polarimetric images and the instrument simulator are also described.

3.2.1 Dust grain model

Composition

The composition of protoplanetary dust is far from trivial (for a recent review see Min & Flynn 2010). In order to come to a simple, yet quite accurate, model of the composition we follow the procedure also adopted by Min et al. (2011b). First we define the abundances of all available dust forming elements to be the same as the Solar composition derived by Grevesse & Sauval (1998a). In meteorites and interstellar dust particles (IDPs) in our solar system all of the available sulfur is in the form of ironsulfide. Therefore, we first put all S in FeS thereby taking away about half of the available Fe atoms. From the remaining Fe, Mg and Si we produce an amorphous Fe/Mg silicate with a stoichiometry in between olivine and pyroxene. We model this mixture by averaging the optical properties of different types of amorphous silicates. In addition to this ironsulfide/silicate mixture we add a contribution from carbonaceous matter. It is found that in our solar system about half of the carbon atoms is in the solid phase (Geiss 1987), and we thus add this abundance in the form of amorphous carbon grains. The composition resulting from this contains by mass 58% silicates, 18% iron sulphide, and 24% amorphous carbon.

To compute the opacities of the dust grains, we need the refractive index as a function of wavelength. This has been measured in the laboratory. For the silicates we use the measurements by Dorschner et al. (1995a) and Henning & Stognienko (1996a), for the iron sulfide we take the laboratory data from Begemann et al. (1994) and for the carboneceous material we take the measurements from Preibisch et al. (1993a).

Grain structure

We distinguish between two extreme types of particle types using the above composition:

1. Compact, homogeneous grains
2. Fluffy, inhomogeneous aggregates.

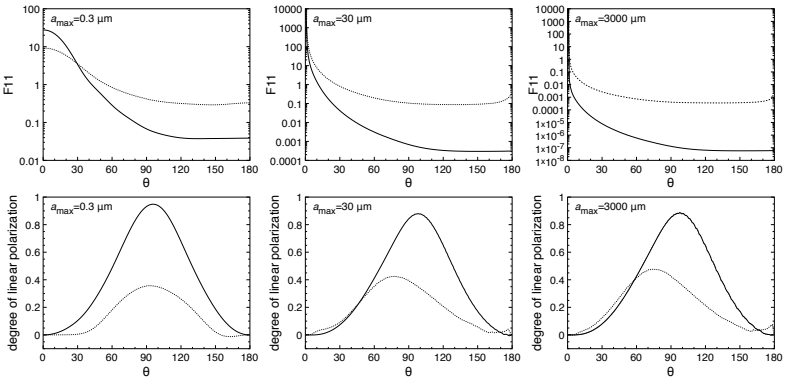

Figure 3.1: The scattering properties of the dust particles for different values of the maximum particle size, $a_{\max}$. Upper panels: the normalized phase function, F_{11}, as a function of scattering angle, θ. Lower panels: the degree of linear polarization as a function of scattering angle. The wavelength is $\lambda = 600$ nm. Solid lines are for the fluffy aggregates, dashed lines for the compact grains.

These two different particle types require different ways of computing the optical properties. In order to correctly estimate the scattered light intensity and degree of polarization, the model used for the optical properties of the grains is crucial. Homogeneous spherical grains cause resonances at certain scattering angles and generally behave differently from more natural, irregular shapes. However, for reference and comparison to other work, we have also computed several models using compact, homogeneous spheres.

Compact, homogeneous grains: This model considers a mixture of grains, each composed of a single material. The optical properties of such a mixture can be obtained by simply averaging the optical properties of homogeneous grains using the given abundances of the various materials. We chose here to model the optical properties of the dust grains using the statistical approach. In this approach we take a wide distribution of simple particle shapes to simulate the variety of irregularities occurring in nature. We use the Distribution of Hollow Spheres (DHS; see Min et al. 2005a) with an 'irregularity parameter' $f_{\max} = 0.8$. It turns out that this choice of this grain shape model, together with our choices for the grain sizes and compositions, provides a scattering matrix quite similar to cometary dust.

Fluffy, inhomogeneous aggregates: When small dust grains collide they can form large, aggregated structures. The optical properties of such aggregates display characteristics of both the constituents as well as of the size of the aggregate as a whole (see e.g. Volten et al. 2007). We use here the approximate method by Min et al. (2008) to compute the optical properties of large, inhomogeneous fluffy aggregates. In this method we use effective medium theory to mix the dust material with vacuum and thus obtain a highly porous, fluffy structure. The vacuum fraction can be computed

parameter	symbol	value
mass of the star	$M_\star$	$2.5\,M_\odot$
effective temperature	$T_{\rm eff}$	10000 K
radius of the star	$R_\star$	$2\,R_\odot$
dust mass in the disk	$M_{\rm dust}$	$1 \cdot 10^{-3}\,M_\odot$
distance to the star	D	150 parsec
outer radius of the disk	$R_{\rm out}$	2000 AU
surface density turnover point	R_0	200 AU
minimum grain size	$a_{\rm min}$	$0.03\,\mu$m
maximum grain size	$a_{\rm max}$	$0.3, 30, 3000\,\mu$m
turbulence parameter	α	10^{-4} (settled), ∞ (flared)
gas to dust ratio	$f_{g/d}$	120

Table 3.1: Values for the model parameters

from the aggregate size and fractal dimension. Though this method was not primarily designed to simulate scattering at optical wavelengths, we find that many of the characteristics attributed to fluffy aggregates are well simulated. In general we find that the grains computed using these methods with the parameters as given by Min et al. (2008) are extremely fluffy and as such give an extremely forward peaked scattering phase function and a very high degree of polarization at 90° scattering angle.

Grain size

To address the effects of grain growth on the observable polarimetric signal we use a parameterized grain size distribution. We adopt a power law size distribution with $n(a) \propto a^{-3}$. Here a is the volume equivalent radius of the grains and the distribution runs from $a_{\rm min}$ to $a_{\rm max}$. We fix $a_{\rm min}$ to $0.03\,\mu$m and vary $a_{\rm max}$ from $0.3\,\mu$m to 3 mm. The different grain sizes are treated separately in the radiative transfer. This implies that they can have different temperatures and a different vertical distribution caused by grain settling.

Fig. 3.1 displays the single scattering phase function and the degree of linear polarization as functions of the scattering angle, θ, for different values of $a_{\rm max}$ at a wavelength of $\lambda = 0.6\,\mu$m.

3.2.2 Disk model

For the disk model we try to avoid parameterization as much as possible. Therefore we compute the vertical scale height of the disk self-consistently. In addition we compute the radial location and structure of the inner rim using evaporation and sublimation physics as described in Kama et al. (2009).

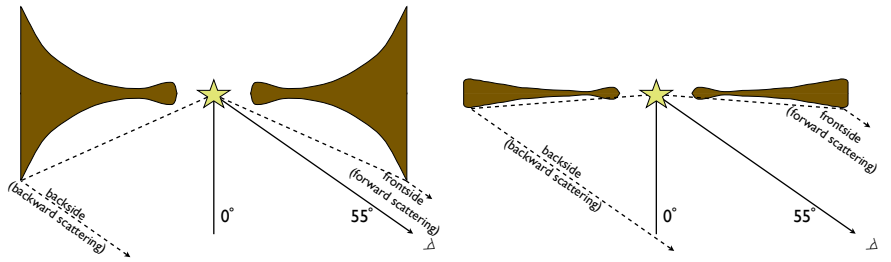

Figure 3.2: Sketch of the two disk geometries. The left panel shows the flaring, well mixed disk structure, while the right panel depicts the settled, flat disk. Note that the scattering angles in the surface layers of the disk depend strongly on the opening angle of the disk.

For the central star we take a Herbig Ae star. We use two different disk types, a flaring disk, where we assume gas and dust to be perfectly coupled, and a settled disk, where we use the settling prescription from Dubrulle et al. (1995) as described above. These two disk types approximately represent the Group I and II sources as defined by Meeus et al. (2001b). All star and disk parameters are listed in Table 3.1.

As the grains grow to larger sizes they decouple from the gas and settle towards the midplane (Dullemond & Dominik 2004b). This is thought to be a possible explanation for the flatter disk structures observed around some stars. A full treatment of settling is beyond the scope of this paper and will be implemented in the future in the MCMax radiative transfer code. Here we parameterize settling using the approximate method by Dubrulle et al. (1995). In this way we do simulate the dependence of settling efficiency on grain size, grain density, gas density and gas temperature. To distinguish between effects of grain settling and grain optical properties we take for the grain settling parameters always those of the material volume equivalent sphere. In principle settling is more efficient for homogeneous compact grains and less efficient for fluffy aggregates. This is simply because the larger surface area of the fluffy grains allows them to couple much easier to the gas. However, since we want to be able to separate disk structure effects as much as possible from effects of grain properties we have chosen to let this effect not influence the settling efficiency and determine the settling properties of all grains as if they were spherical homogeneous grains with the same mass. The description of grain settling we use has one free parameter, which is the strength of the turbulence, α. This parameter defines the balance between settling and vertical mixing. For the settled disk models we take $\alpha = 10^{-4}$, while for the well mixed models we set $\alpha = \infty$.

The radial density distribution of the dust disk was parameterized using a radial surface density (Hughes et al. 2008)

$$\Sigma(r) \propto r^{-p} \exp\left\{-\left(\frac{r}{R_0}\right)^{2-p}\right\}, \tag{3.1}$$

for $r < R_{\rm out}$. Here R_0 is the turnover point from where an exponential decay of the

surface density sets in and p sets the power law in the inner region. We fix this to $p = 1$ which is a commonly used value (see e.g. Dullemond et al. 2006). Note that although we take the outer radius of the disk to be 2000 AU, the surface density of the disk is already highly diminished after the turnover radius $R_0 = 200$ AU.

In Fig. 3.2 we depict the two different disk structures considered. This figure illustrates the fact that the scattering angles of the surface layers of the disk depend strongly on the opening angle. In the case of a very flat disk the scattering angles observed at the frontside and the backside of the disk are symmetric around 90°. With i the inclination angle of the disk the scattering angles at front and backside for a very flat disk are $\theta = 90° - i$ and $\theta = 90° + i$ respectively. In the case of a strong flaring disk with a large opening angle ψ the scattering angles at front and backside are symmetric around $90° - \psi$ and become $\theta = 90° - \psi - i$ and $\theta = 90° - \psi + i$.

3.2.3 Radiative transfer

The transfer of radiation through the disk is done in full using the 3D axisymmetrical radiative transfer code MCMax (Min et al. 2009a). This code uses Monte Carlo radiative transfer to compute the disk temperature structure and from this the vertical density scale-height and the sublimation state of the dust (see also Kama et al. 2009). The scattering of radiation is done using the full scattering matrix acting on the Stokes vectors. The grains in the disk are assumed to be in random orientation so symmetry arguments can be used to simplify the scattering matrix.

Often images and other observables are extracted from Monte Carlo radiative transfer methods by simply collecting the escaping photons after they are traced through the disk. Although this is an elegantly simple way, we adopt a different technique to construct the images which allows us to obtain accurate results even in the very faint parts of the image. After the temperature structure of the disk is obtained, images are constructed by integrating the formal solution to the radiative transfer. For this, also the local scattering source function is needed. This is again constructed using a Monte Carlo approach. In combination with the local thermal source function, obtained from the temperature, the formal solution can be easily integrated to obtain smooth images. The advantage of this method over 'classical Monte Carlo' photon collecting methods is that the information accumulated during the Monte Carlo photon tracing process is used to the fullest to obtain smooth images also in regions where only a small fraction of the photons arrive. This is especially important for imaging polarimetry where one of the main purposes is to gain a very high dynamic range in the image.

3.2.4 Instrument simulation

Ground-based observations are affected by atmospheric and instrumental effects such as seeing and instrumental polarization. To account for these effects, a numerical simulation including readout noise, photon noise, instrumental polarization and different seeing conditions has been performed. These simulations model the dual-

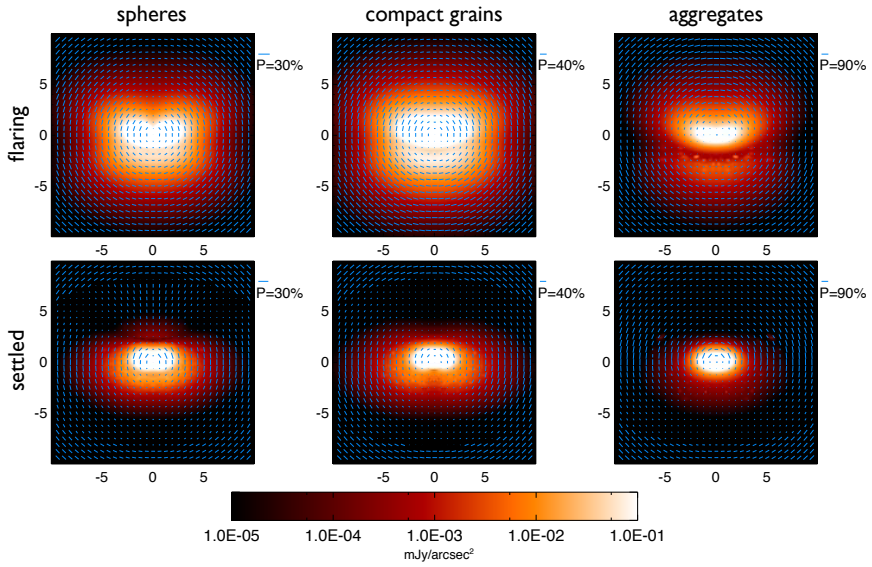

Figure 3.3: Comparison of the polarized intensity maps for different grain types. Upper panels are for the flared disks, lower panels for the settled disks. Left panel: homogeneous spheres, middle panels: compact, irregularly shaped grains, right panels: fluffy aggregates. For all images the maximum size of the particles is 30 μm. Spatial scale is in arcseconds. The length of the vectors is proportional to the degree of polarization. The inclination of the disk is 55° with respect to pole on.

beam imaging polarimeter ExPo (Rodenhuis et al. 2008a, 2011a), currently a visitor instrument at the 4.2 meters William Herschel Telescope (WHT). ExPo measures linear polarization at optical wavelengths, and combines very short exposure times with the dual-beam technique to minimize systematic errors. In a standard observation thousands of single exposure frames are combined to obtain a total exposure time of $\sim$ 15 minutes.

The Point Spread Function (PSF) for the Extreme Polarimeter (ExPo) is calculated as

$$\mathrm{PSF}(\lambda) = \left|\mathcal{F}\{A \cdot e^{i\varphi(\lambda)}\}\right|^2, \tag{3.2}$$

where $\mathcal{F}$ stands for *Fourier Transform*. A and ϕ refer to the amplitude and phase of the incoming wavefronts, respectively. A set of short-exposure-time wavefronts is calculated for different seeing conditions. We assume a Kolmogorov spectrum for the phase fluctuations of the wavefront (for details see Appendix 3.6.2). Broadband PSFs are obtained from these sets of wavefronts combined with the aperture of the telescope after which they are convolved with full resolution simulated images. Readout noise, photon noise, instrumental polarization and guiding errors are added to these images. This set of simulated-raw images is then reduced with the *ExPo*

Pipeline, described in detail in Canovas et al. (2011c).

The characteristics of this simulation are summarized in Table 3.3. The simulation of the atmosphere, telescope and instrument is detailed in Appendix 3.6.1.

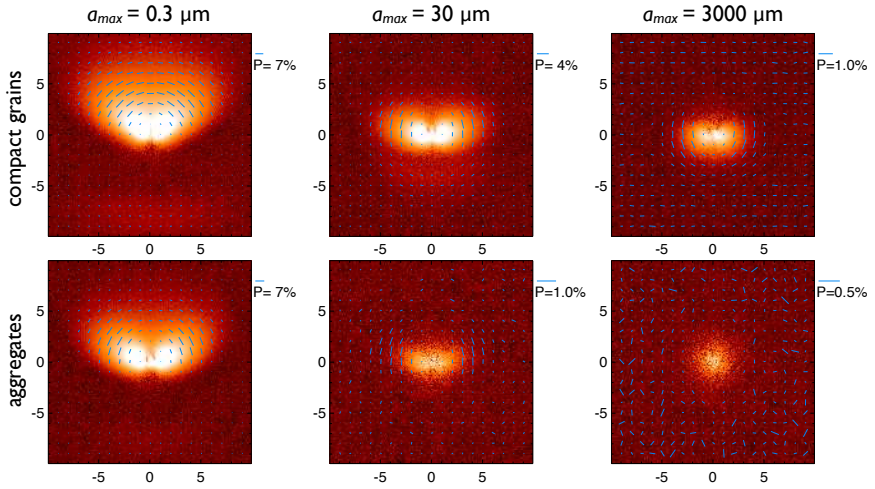

Figure 3.4: Comparison of the polarized intensity maps for different grain sizes. All panels are for the well mixed, i.e. flaring, disk models. Upper panels are for the compact grains, lower panels for the fluffy aggregates. The maximum particle size in the size distribution increases from left to right. Spatial scale is in arcseconds. The length of the vectors is proportional to the degree of polarization. The inclination of the disk is 55° with respect to pole on. Color scale is the same as in Fig. 3.3.

3.3 Resulting full resolution images

In this section we discuss the intrinsic polarimetric images of the disks and the effects of the different dust properties and disk parameters. All full resolution model images are generated at a wavelength of $\lambda = 600\,\mathrm{nm}$. Though detailed studies of the color behavior of the polarized images can be a useful diagnostic, the general monochromatic behavior of the images is not very sensitive to the exact wavelength. We use these single wavelength images to represent the average broadband signal. So the broadband effects are fully taken into account for the simulation of the telescope and instrument, but the full resolution model disk images are computed at a single wavelength.

In Fig. 3.3 we present polarization maps for the different dust types. Besides the dust grain types discussed above, we also include images for homogeneous spherical grains. It is clear from this figure that the type of dust grain has a large influence on the appearance of the disk. Especially in the upper part of the image the homogeneous spherical dust grains display a behavior not seen for the more realistic dust models.

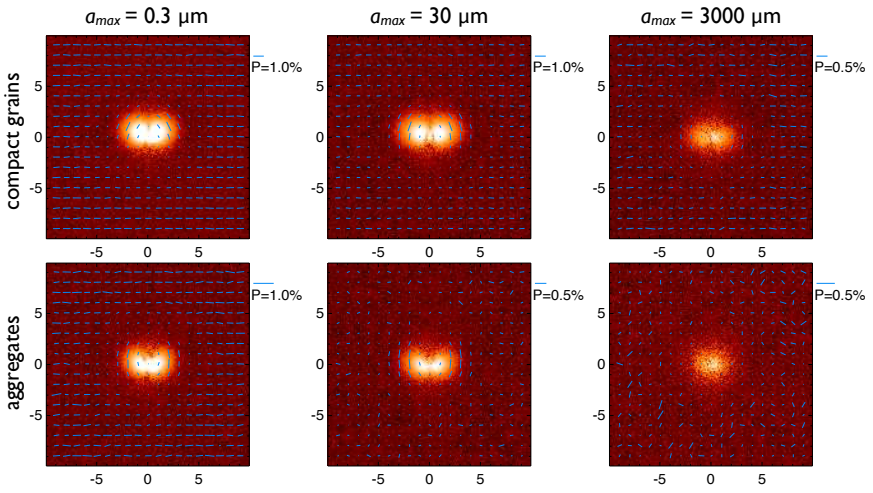

Figure 3.5: Same as Fig. 3.4, but for the settled disk models.

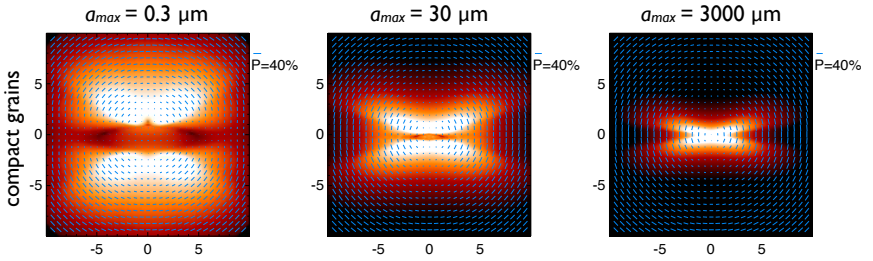

Figure 3.6: Comparison of the polarized intensity maps for different grain sizes in the nearly edge on case. All panels are for the flared disk models with compact dust grains. The settled disks display only a very thin signature. The maximum particle size in the size distribution increases from left to right. Spatial scale is in arcseconds. The length of the vectors is proportional to the degree of polarization. The inclination of the disk is 85° with respect to pole on. Color scale is the same as in Fig. 3.3.

Also, it is clear that the fluffy aggregates are fainter than the compact grain models. This is caused by the extremely forward scattering nature of the fluffy aggregates, where only a small fraction of the light is scattered towards the observer.

In Figs. 3.4 and 3.5 we show the polarized intensity maps for the compact grains and the fluffy aggregates for different values of the maximum grain size in the size distribution. For the flared disk models (Fig. 3.4) it is clear that the brightness and spatial extend of the disk decreases when the particle size is increased. This is caused by the reduced opacity of the larger particles, which decreases the flaring angle of the disk. For the settled disk models we see a slightly different trend. Because the surface layer of the disk is here already in the shadow, the decrease of the height of the disk is

not so important. More important in this case is the increase in the scattering albedo, causing the disk to become brighter and appear larger at first when the particle size is slightly increased. When the particle size is increased further, the decrease of the total opacity becomes dominant and the disk becomes fainter again.

Murakawa (2010) discusses the 'roundabout effect' for edge-on disks in near infrared polarimetric imaging. In the dark lane of an edge-on disk no first order scattering can be observed since no starlight can reach these regions in the disk. Second order scattering causes the polarization vectors to be aligned not perpendicular to the direction towards the central star, but parallel to the dark lane of the disk. We observe this effect also in our optical polarization images of the most flaring edge-on disks. Figure 3.6 shows the polarized intensity maps for the disks seen edge-on for different grain sizes. We only show the compact grain models, but the fluffy aggregate models show similar behavior. Clearly we see the roundabout effect in the flaring disk with only small grains. As soon as the grain size is increased, or the disk is settled, the effect disappears because the dark lane becomes too narrow. The region where the effect can be observed is very weak in polarized intensity as compared to the region above and below. This implies that in observations with a limited spatial resolution the effect will be washed away by PSF smearing.

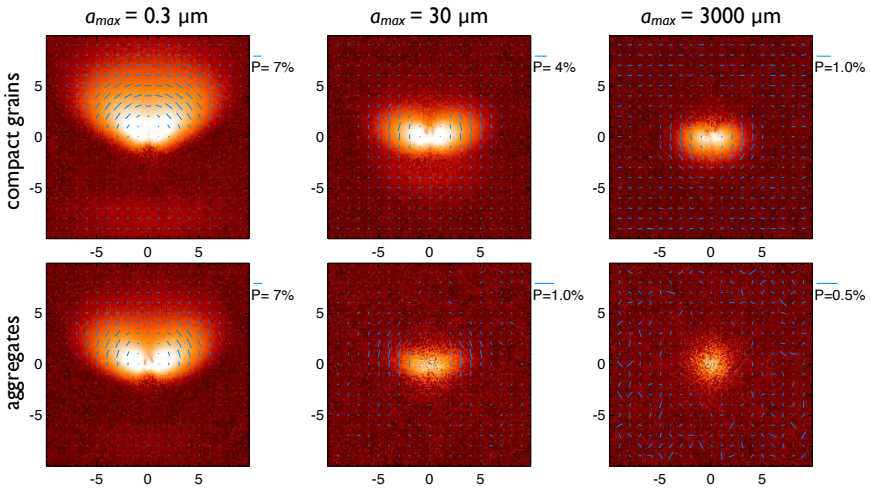

Figure 3.7: Same as Fig. 3.4, but simulated as observed with ExPo at the WHT. Color scale is logarithmic, in arbitrary flux units, and the same in all images.

3.4 Simulated observational images

We present images simulated for the ExPo instrument mounted at the 4.2 m William Herschel Telescope (WHT). The aim here is to get a feeling for the effects of atmo-

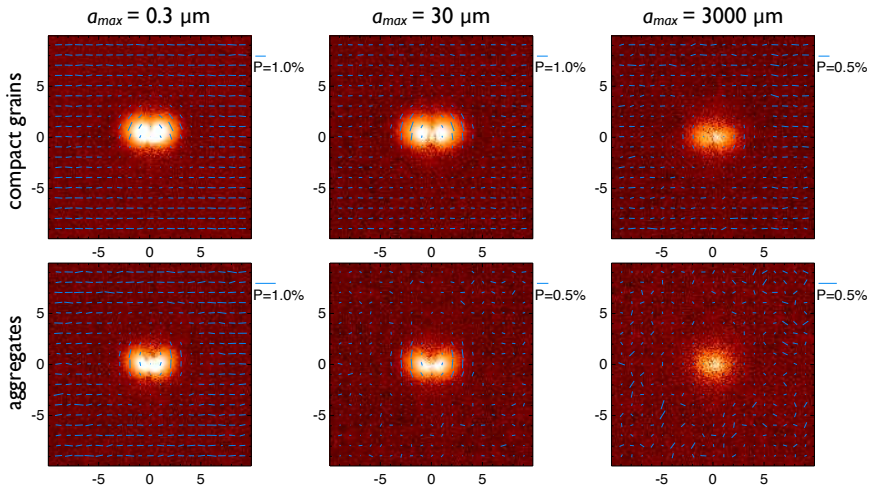

Figure 3.8: Same as Fig. 3.5, but simulated as observed with ExPo at the WHT.

spheric seeing, telescope diffraction and noise on the interpretation of polarimetric images.

The final image observed through a telescope in polarization from a protoplanetary disk depends not only on the intrinsic degree of polarization caused by the grains but is also influenced by the depolarizing effects of the point spread function of the central star. How strong this depolarizing effect is depends on the intensity of light scattered off the disk. Below we discuss the effects of the different grain types on the intrinsic polarization image as well as how these different models are affected by telescope effects like diffraction, seeing and noise.

In Figs. 3.7 and 3.8 we show the different disk and dust types as they would be observed with ExPo at the WHT under good seeing conditions, i.e. a seeing at 500 nm of 0.8″. The arcs that can be seen in some of the images are a numerical effect caused by the grid of the models in combination with diffraction effects due to the spiders of the telescope. There is a clear dependence of the detectibility on the particle size distribution and the vertical disk geometry. The settled disks are much harder to detect, since they are intrinsically fainter.

The polarized intensity is the product of the total intensity and the degree of polarization. Due to the opening angle of the disk, the backside of the disk is closer to 90° scattering angle and thus has a higher degree of polarization (see also Fig. 3.2). This can be seen in the high resolution images by the longer vectors in the upper parts of the images. The front side of the disk is, however, much more forward scattering and thus has a higher total intensity. Because the central star is the dominant intensity source in the observational images, the degree of polarization now (in the extreme case) is basically the polarized intensity divided by the total intensity of the central star, and not by the total intensity of scattered light. Looking at the observed settled

disk models (i.e. Fig. 3.8), it can be seen that in the images for the compact grains, the degree of polarization still wins (also see the length of the polarization vectors), and the backside of the disk is somewhat brighter in polarized intensity. Due to the highly forward-scattering nature of the fluffy aggregates, in that case the differences in total intensity dominate, and the front side of the disk is brighter in polarized intensity and in degree of polarization.

Since we run the full ExPo data analysis pipeline as discussed in Canovas et al. (2011c) we also correct for any instrumental polarization. This is done by assuming that the signal from the central resolution element, i.e. the central star, should be unpolarized. In the simulation of the instrument we do not add polarization caused by the telescope, but we include instrumental polarization due to different transmission coefficients (see Appendix). Nevertheless, the central resolution element is polarized because of scattering from the innermost regions of the disk. Since the disk is inclined, scattering by this innermost region has a non-zero integrated polarization (see also Fig. 3.10). This polarization is then 'corrected' under the assumption that it is instrumental, and thus subtracted from the entire image. This causes the vertical depolarized region in the images where the outer disk is weak. This also causes the well oriented polarization vectors in the noise regions of the images for the cases where the disk is very weak (especially clear in Fig. 3.8). The amplitude of this effect strongly depends on the seeing conditions. In Fig. 3.9 we show two disk models under different seeing conditions. It is clear that the appearance is different and the overcorrection of the instrumental and inner disk polarization is larger in the case of worse seeing.

In Fig. 3.10 we show the degree of polarization of the inner resolution elements as a function of the size of the resolution element. We do this by integrating both Stokes I and Q out to a distance R from the central star. The degree of polarization shown in Fig. 3.10 is the ratio of these two integrated values. This shows that increasing the spatial resolution also significantly reduces the effect of polarization from the central resolution element. In the case of images limited by atmospheric seeing of $\sim 1''$ we see that the inner resolution element can be polarized by up to $\sim 0.8\%$. Adding an extreme adaptive optics system increasing the spatial resolution to $0.02''$, this degree of polarization can be reduced significantly. In the case of fluffy aggregates that have grown to significant sizes we see that the integrated degree of polarization is very small. This is caused by the fact that in these cases the total scattered intensity is very much dominated by forward scattering, which has a very low degree of polarization. Hence although the polarization of the central resolution element is small, the spatially resolved degree of polarization is also extremely low. The large variations of the curves in Fig. 3.10 show that when we have sufficient resolution and the images are properly calibrated we do have a good diagnostic for the grain and disk properties.

$a_{\max}$	0.3 μm	30 μm	3000 μm
Good seeing (r_0 = 10 cm)			
Flared disk, compact grains	+	+	+
Flared disk, fluffy aggregates	+	+/-	-
Settled disk, compact grains	+	+	-
Settled disk, fluffy aggregates	+	+	-
Bad seeing (r_0 = 5 cm)			
Flared disk, compact grains	+	+	-
Flared disk, fluffy aggregates	+	-	-
Settled disk, compact grains	+	+/-	-
Settled disk, fluffy aggregates	+	-	-

Table 3.2: Detectability of the different disk and dust types used in this simulation with ExPo at the WHT. See Table 3.1 for the details of the model.

3.4.1 Detectability

In order for a disk to be detectable with an imaging polarimeter at a 4m class telescope without adaptive optics we need the disk to be extended enough to escape the PSF of the central star and bright enough to rise above the photon and readout noise. Treating the models as observations we have determined which disk and dust parameters allow detection with this instrument. For this we assumed a total integration time of $\sim$ 5 minutes per polarization state. The visual magnitude of the star, as derived from the input parameters in Table 3.1, is $V = 7$. The results are summarized in Table 3.2. We see that disks that have undergone significant grain growth are hard to detect, especially when the turbulence in the disk is not strong enough to mix up the larger grains to the disk surface layers, i.e. in the settled disk models. Also, we notice that the seeing conditions play a major role in the detectability. An adaptive optics system, eliminating this factor, will greatly increase the detection capabilities of imaging polarimeters.

3.4.2 Disk gaps

Many systems have been observed, directly or indirectly, to have depleted inner disks, or cleared out gaps (see e.g. Bouwman et al. 2003, Brown et al. 2007, Espaillat et al. 2008, Thalmann et al. 2010, Merín et al. 2010, Andrews et al. 2011, Verhoeff et al. 2011). One of the possible causes for this is clearing by a planet in the disk, and thus direct detection of such disk gaps is of great importance for constraining planet formation scenarios and timescales. To see if we can detect such disk gaps and globally what it would look like in a polarimetric imaging observation we ran a disk model with a cleared out gap from 120 to 180 AU and an inner disk with a depletion of a factor of 10 for radii smaller than 120 AU (a parameterization very similar to the one adopted by Andrews et al. 2011). Note that we do not aim to span parameter space for this case but rather provide an example of inner disk clearing.

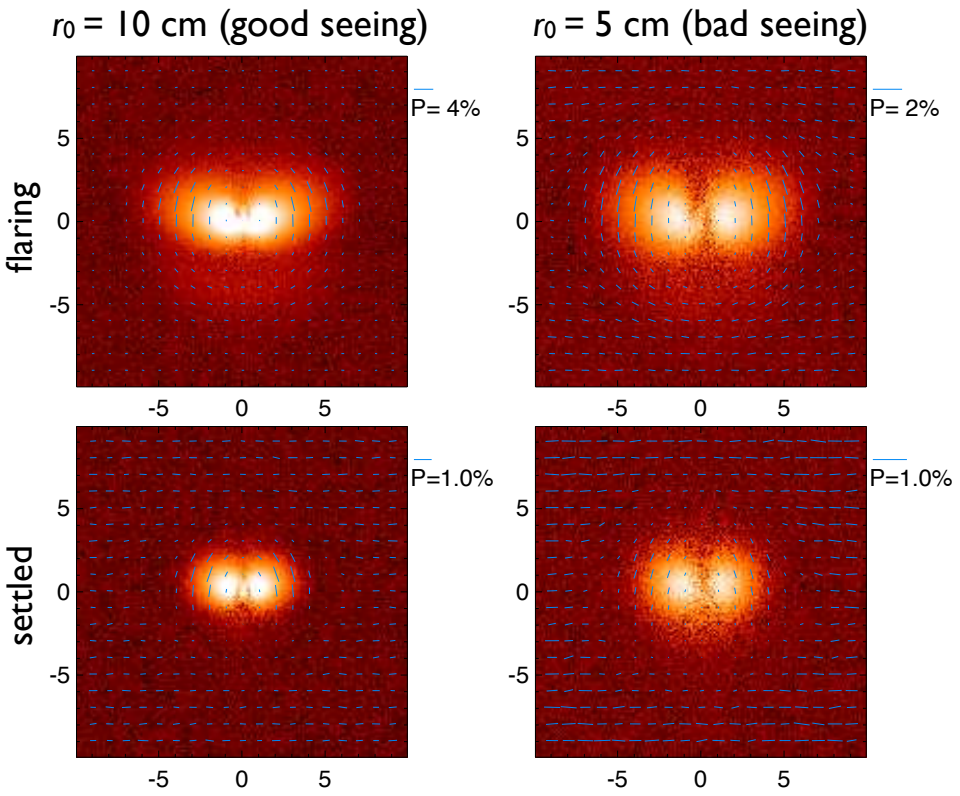

Figure 3.9: Comparison of the polarized intensity maps as obtained under different seeing conditions. Upper panels are for a flared disk, lower panels for a settled disk. All images are using $a_{\max} = 30\,\mu$m and compact grains.

The images for compact grains with $a_{\max} = 30\,\mu$m are shown in Fig. 3.11, where we show both the full resolution images (left) and the simulated observations (right). For the instrument simulations we increased the integration time by a factor of 10 to suppress the photon noise in the inner disk regions. As we can see the depletion of the inner region is clearly detected. Comparing to the left panels of Fig. 3.9 (which shows the same models without depleted inner disks), we see a very clear difference. We do note that for the flaring disk case in the simulated observations the inner disk is undetectable, while it is still clearly visible in the full resolution images. This is caused by the fact that the entire inner disk is inside the central resolution element (0.8″ seeing). As a consequence the polarization signal caused by the inner disk is considered instrumental by the data reduction pipeline and is subtracted. We have also computed images where we placed the gap closer in and we find that an inner radius of the outer disk of ~ 180 AU (or 1.2″) is close to the limit where we are still able to clearly identify the disk gap in the image. For radii of the inner edge of the

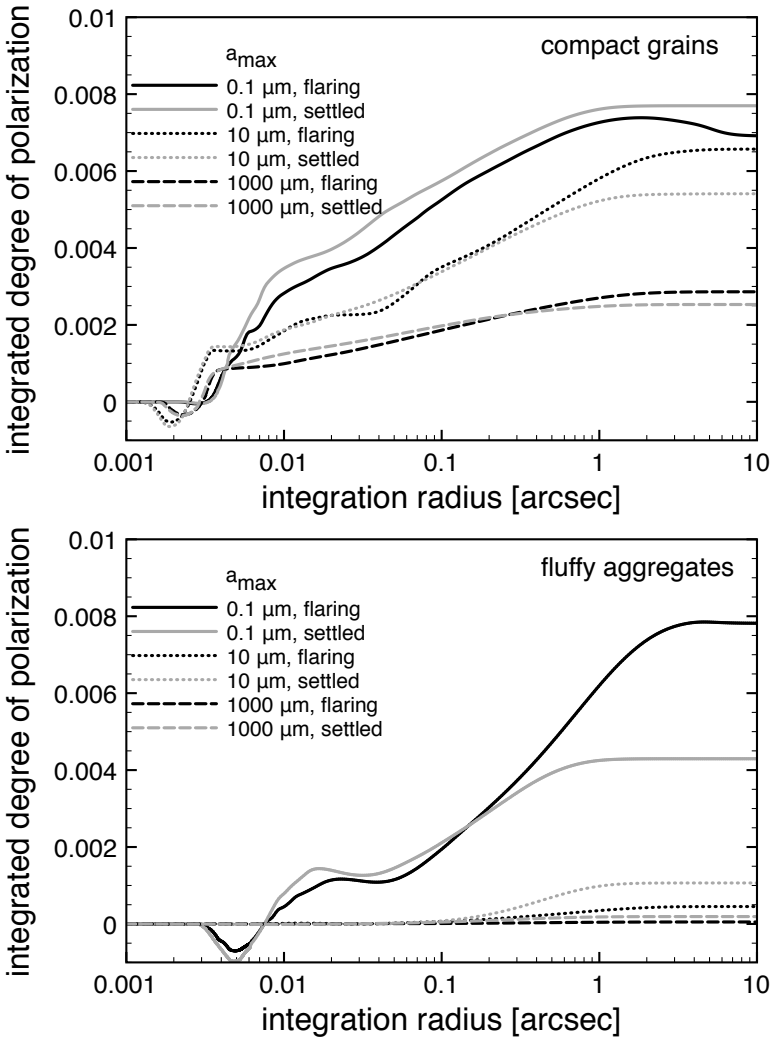

Figure 3.10: The integrated degree of polarization as a function of the radius of integration. Upper panel is for the compact grains, lower panel for the fluffy aggregates. Black curves are for the flared disk models, grey curves for the settled disk models.

outer disk larger than ~ 100 AU we do see significant changes to the image, but they become increasingly more difficult to identify as a clear signal from a disk gap as the radius decreases.

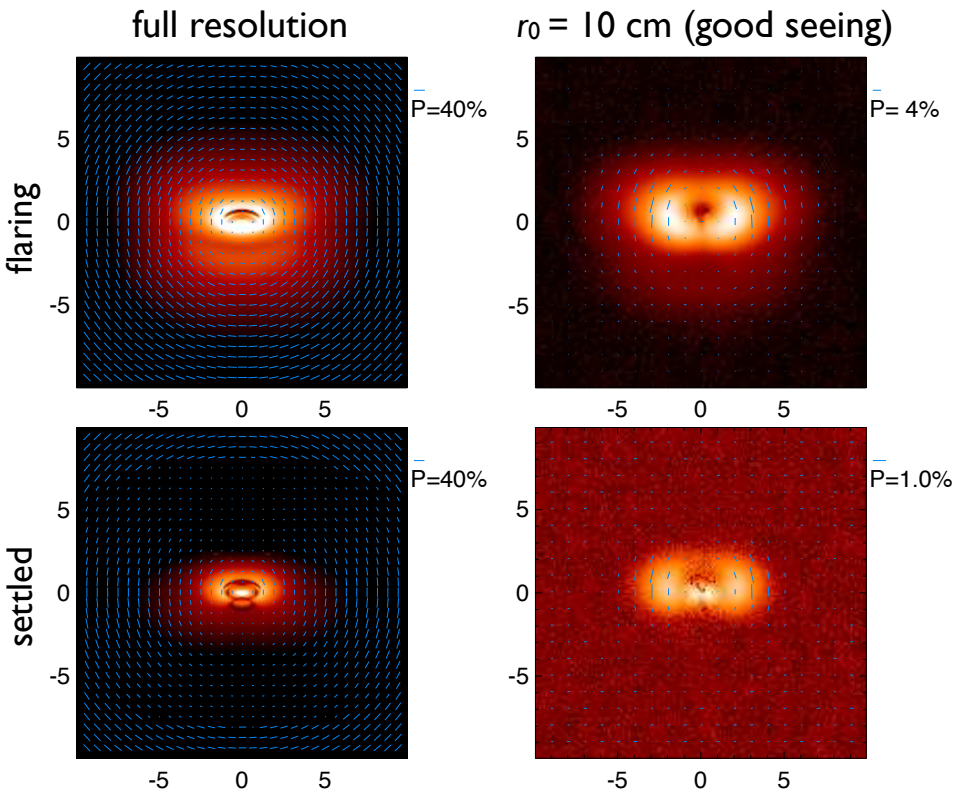

Figure 3.11: Full resolution images (left panels) and simulated observations (right panels) of models with a depleted inner disk. The innermost regions (radii < 120 AU) are depleted by a factor of 10, while from 120 to 180 AU the disk is cleared of dust. Upper panels are for a flared disk, lower panels for a settled disk. All images are using $a_{\max} = 30\,\mu$m and compact grains. Note that the color scale is altered with respect to the previous images to enhance details in the bright inner disk region.

3.5 Discussion and conclusions

The appearance of circumstellar disks in polarized light depends heavily on both the properties of the disk and of the composing dust particles. We model the observable signature of protoplanetary disks surrounding young, intermediate mass stars with varying dust and disk properties. We conclude that:

- Imaging polarimetry is a powerful technique to image the disks surrounding young, intermediate mass stars. Computations show that even with a seeing-limited instrument at a 4m class telescope we are able to image circumstellar structures for a variety of dust and disk properties.

- Studying different dust particle types we conclude that there is a significant difference between the appearance of a disk with only compact grains and a disk containing fluffy aggregated dust particles. We find that the commonly employed homogeneous sphere model gives results significantly different from more realistic models. The observed signal depends on the properties of these more realistic models quite significantly, thus providing a potentially powerful diagnostic. We note here that a proper use of this diagnostic is not always trivial.
- Due to the extreme forward scattering nature of fluffy aggregates, where only a small fraction of the radiation is scattered towards the observer, a disk containing these kinds of particles appears significantly dimmer in scattered light.
- The diagnostic power of imaging polarimetry is a strong function of spatial resolution. Atmospheric seeing blurs out many details needed for a thorough analysis of dust properties, and thus allows mainly the global disk parameters to be deduced.
- The 'roundabout effect' for edge on disks as discussed by Murakawa (2010) for near-IR polarimetry was in our study only found for an extremely flaring disk containing only small grains. Since the effect appears in the very low intensity regions of the image it disappears when we consider observations with limited spatial resolution.
- The accuracy of the correction for instrumental polarization using the central star as calibration source strongly depends on the spatial resolution. In the seeing-limited case, the central resolution element can have a degree of polarization of up to $\sim 0.8\%$. This degree of polarization quickly decreases when the spatial resolution of the observations is increased.

3.6 Appendix

3.6.1 Instrument simulation

Here we discuss the details of the instrument simulations. The instrument simulator was developed to simulate observations with the Extreme Polarimeter (ExPo), which is a visitor instrument of the 4.2 m WHT.

3.6.2 Wavefront Generation

To generate wavefronts, we make use of a model of turbulence first proposed by Kolmogorov (1941) and later developed by Tatarski (1961) and Fried (1966). According to this model, a flat wavefront travelling through the turbulent atmosphere will modify its phase, while the change in its amplitude is negligible compared to the phase fluctuations. The amplitude of the wavefront, after it travels through the

telescope, is proportional to the telescope's aperture. The power spectrum of the phase fluctuations of a wavefront travelling through the atmosphere is given by

$$\Phi(k) = \frac{0.023}{r_0^{5/3}} k^{-11/3}, \tag{3.3}$$

where r_0 is *Fried's Parameter* and k is the wave number. The parameter r_0 represents the circular aperture over which the wavefront phase variance is equal to 1 rad^2 for the case of Kolmogorov turbulence. Therefore, the higher r_0, the more stable the atmosphere, or, in other words, the better the *seeing* is. For instance, a value of r_0 of about 10 cm produces 1 arcsec seeing at $\lambda = 500$ nm (i.e. Nightingale & Buscher 1991). The value of r_0 depends on the wavelength, following a power law: $r_0 \propto \lambda^{6/5}$. Figure 3.12 shows an example of an *uncalibrated* wavefront phase generated from Eq. 3.3.

The timescale at which one of these wavefronts remains constant, the *coherence time*, at optical wavelengths is of the order of a few milliseconds (Vernin & Munoz-Tunon 1994, Law 2006, García-Lorenzo et al. 2009). The single frame PSF has two main components:

- *Tilt,* producing random motion of the whole image.
- *Roughness,* producing the observed speckle pattern.

When the exposure time is similar to the coherence time, the image motion due to the tilt component can be removed in the data processing by proper centering of each frame. Noll (1976) showed that the variance σ^2 of the wavefronts can be expressed in terms of the telescope diameter, D, and the Fried Parameter, r_0

$$\sigma^2 = 0.134 \left(\frac{D}{r_0}\right)^{5/6}. \tag{3.4}$$

The standard deviation σ of the wavefront phase φ, expressed in wavelength units, can be obtained from the variance as $\sigma_\lambda = 2\pi\sigma$

$$\sigma_\lambda = \frac{0.134^{1/2}(D/r_0)^{5/6}}{2\pi} = 0.0582 \left(\frac{D}{r_0}\right)^{5/6}. \tag{3.5}$$

In our simulation, D is the diameter of the WHT main mirror (4.2 meters), and three different values of r_0, (5,7 and 10 cm) are used to account for bad, medium and good seeing at a reference wavelength of 500 nm, λ_{500}. From Eq 3.4 and the dependence of r_0 with wavelength, σ_λ can be computed at different wavelengths from our reference as

$$\sigma_\lambda = \sigma_{\lambda_{500}} \cdot \frac{\lambda_{500}}{\lambda}. \tag{3.6}$$

Wavefronts at different wavelengths are calibrated according to Eq. 3.4 and Eq. 3.6. A set of wavefronts at different wavelengths is then generated for each of the three different r_0 values used in this simulation.

Parameter	Value
Telescope diameter	4.2 [m]
Wavelength range	450-700 [nm]
Exposure time	0.028 [seconds]
Pixel size	0.078 [″/pixel]
Grid size	2048×2048 [pixels]

Table 3.3: Simulation Parameters

3.6.3 PSF Generation

To generate a PSF, we first simulate the aperture of the WHT, taking into account the spiders of the telescope and the central obscuration of the main mirror. Once the telescope aperture and the wavefront are computed, a monochromatic PSF is calculated according to Eq. 3.2. A broadband PSF (PSF_{bb}) is calculated as the sum of monochromatic PSFs calculated over the range of 400 nm to 700 nm, in steps of 10 nm:

$$\mathrm{PSF}_{bb} = \sum_{\lambda=400,10}^{700} \left| \mathcal{F}\{A \cdot e^{i\varphi(\lambda)}\} \right|^2. \tag{3.7}$$

This PSF produces the speckle pattern obtained when observing at exposure times of the order of the coherence time (a few milliseconds). The PSF measured when observing at longer exposure times will be the sum of the short-exposure broadband PSFs. To simulate ExPo-like PSFs we set the coherence time to 9.3 millisecond, and then generate a 28 milliseconds exposure PSF as the sum of three statistically independent short-exposure broadband PSFs:

$$\mathrm{PSF}_{\mathrm{ExPo}} = \sum_{i=1}^{3} \mathrm{PSF}_{bb}^{i}. \tag{3.8}$$

These calculations are computed on a 2048×2048 pixels grid. The pixel size of this simulation is determined by the Nyquist frequency: $N_\nu = (\lambda/2D) \cdot 206265$, which produces a pixel size of 0.0122 [″/pixel], for a 4.2 meters telescope and a central wavelength of 500 nm. The original 2048×2048 pixel grid is then binned to an smaller grid to produce simulated images at the ExPo pixel size (0.078 [″/pixel]). Fig. 3.13 shows an example of a PSF for both simulated (left) and a real (right) data (0.8″ seeing, 0.028 seconds exposure time).

A total of 100 different $\mathrm{PSF}_{\mathrm{ExPo}}$ are produced for each of the three different seeing conditions tested here. Fig. 3.14 shows an example of three different broadband PSF's calculated for bad (left), normal (center) and good (right) seeing.

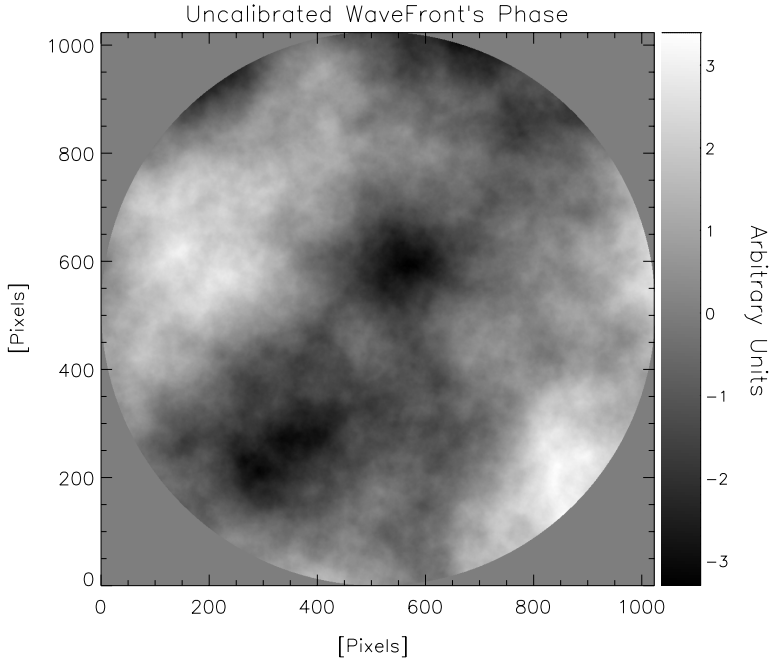

Figure 3.12: Phase of a wavefront following the Kolmogorv model of turbulence.

3.6.4 Dual Beam Simulation

As a dual beam instrument, ExPo produces two simultaneous images with opposite polarization states which are imaged onto a CCD. We will refer to these two images as *left* and *right* images. These measurements are modulated by a Ferro-electric Liquid Crystal (FLC), which switches between two orthogonal polarization states (A and B). Two different frames, containing four different images are produced at the end of one FLC cycle:

$$A_L = 0.5(I + P)_0 * PSF_A, \tag{3.9}$$

$$A_R = 0.5(I - P)_0 * PSF_A, \tag{3.10}$$

$$B_L = 0.5(I - P)_0 * PSF_B, \tag{3.11}$$

$$B_R = 0.5(I + P)_0 * PSF_B, \tag{3.12}$$

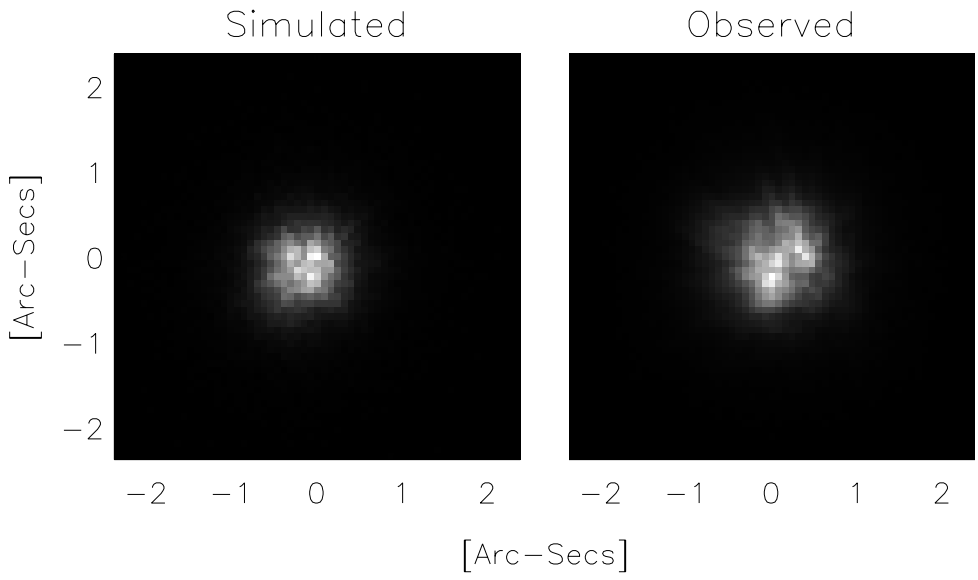

Figure 3.13: Left: Simulated PSF with seeing $\approx 0.8''$, 0.028 seconds exposure time. Right: Observed PSF under the same conditions.

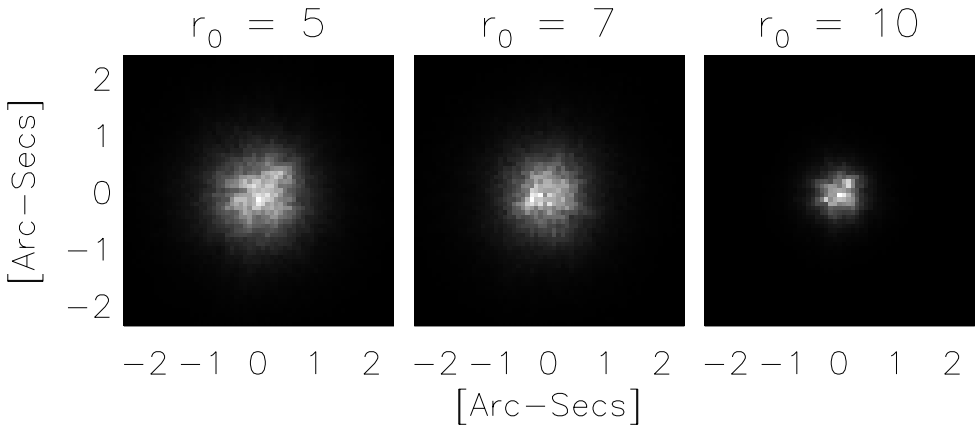

Figure 3.14: Simulated speckle pattern for different values of r_0, given in centimeters.

Coefficient	Value
T_L	0.48
T_R	0.52
T_A	0.998
T_B	1.002

Table 3.4: Transmission Coefficients measured from ExPo instrument.

where, for the sake of simplicity, neither instrumental polarization nor instrumental effects are considered. I_0 and P_0 represents the total intensity and polarization (Stokes Q or Stokes U) of the observed target, as seeing without atmosphere and diffraction effects, respectively. PSF_A and PSF_B are the short exposure PSF for the A and B frames, respectively. These images are given in mJy units, and they are converted to *counts* by taken into account the telescope area, exposure time,filter transmission (Johnson V filter is used here), atmospheric + instrument absorption and CCD efficiency.

The POIDEV function from the NASA IDL library is used to simulate the photon noise for each of these images. Real readout noise from ExPo measurements is added to the simulated data. Instrumental polarization is simulated by including two transmission coefficients for each of the beams (T_L, T_R) and another two coefficients to account for the FLC transmission (T_A, T_B). The value of these coefficients is listed in Tab. 3.4. To mimic guiding problems, a random shift with a maximum amplitude of 10 pixels is applied to each of the simulated images. The final simulated images are then described by:

$$A_L = T_A \cdot T_L \cdot (I + P)_0 * PSF_A \cdot M(x, y) + Ph_{AL} + RO_{AL}, \tag{3.13}$$

$$A_R = T_A \cdot T_R \cdot (I - P)_0 * PSF_A \cdot M(x, y) + Ph_{AR} + RO_{AR}, \tag{3.14}$$

$$B_L = T_B \cdot T_L \cdot (I - P)_0 * PSF_B \cdot M(x, y) + Ph_{BL} + RO_{BL}, \tag{3.15}$$

$$B_R = T_B \cdot T_R \cdot (I + P)_0 * PSF_B \cdot M(x, y) + Ph_{BR} + RO_{BR}, \tag{3.16}$$

where $M(x, y)$ represents the image shifting function, Ph is the photon noise and RO represents the readout noise.

We finally run the full data reduction pipeline for the simulated observations to obtain the final images presented in Figs. 3.7, 3.8, and 3.9.

Science... Never solves a problem without creating ten more.
— George Bernard

Chapter 4

Constraining the nature of Z CMa via imaging polarimetry

H. Canovas, M. Min, S. V. Jeffers, M. Rodenhuis and C. U. Keller *

Abstract

Z CMa is a complex binary system, composed by a Herbig Be and an FU Ori stars. The Herbig star is surrounded by a dust cocoon of variable geometry, and the whole system is surrounded by an infalling envelope. Previous spectropolarimetric observations have reported a preference orientation of the polarization angle, perpendicular to the direction of a large, parsec-sized jet associated with the Herbig star. We aim to constrain the properties of Z CMa by means of imaging polarimetry at optical wavelengths. The variability in the amount of polarized light has been associated to changes in the geometry of the dust cocoon that surrounds the Herbig star. Using ExPo, a dual-beam imaging polarimeter which operates at optical wavelengths, we have obtained imaging (linear) polarimetric data of Z CMa. Our observations were secured during the return to quiescence after the 2008 outburst. We detect two polarized features which have not been reported before. Our results suggest the presence of a hole in the dust cocoon that surrounds the primary star of this system. According to our simulations, this hole has to be pointing towards the West side of Z CMa, producing a pencil beam of light directed towards us, which we see scattered off the low-density envelope surrounding the system. Comparison with numerical models allow us to constrain the nature of this hole, and to obtain an approximation for the mass infalling ratio of the the dust envelope around Z CMa.

*Submitted to *Astronomy and Astrophysics*

4.1 Introduction

Z CMa is one of the most complex young binary systems known to date. Originally identified as an FU Ori star (Hartmann et al. 1989), recent studies show a much more complicated scenario where a Herbig Be star inside a dust cocoon cohabits with an FU Ori star and an in-falling envelope surrounding the binary system (Alonso-Albi et al. 2009). Furthermore, a 3.6 parsec-sized optical jet and a micro-jet are associated to the Herbig and the FU Ori stars, respectively (Whelan et al. 2010). Z CMa belongs to the CMa OB1 association, with distances estimates ranging from 930 pc to 1150 pc (Clariá 1974, Herbst et al. 1978, Ibragimov & Shevchenko 1990, Kaltcheva & Hilditch 2000).

Koresko et al. (1991) first showed the presence of an infrared companion to the FU Ori star. In this work, near infrared (NIR) speckle interferometry revealed a companion located at 0.1" from the FU Ori star at a position angle of 305° ± 2°, east of north. This object showed a cool infrared excess, which suggested the presence of an *spherical dust distribution* around it. The possibility of a stellar photosphere or an accretion disk as the source of this cool excess was rejected because of the youth of the system. Two-dimensional speckle interferometry at K band (Christou et al. 1992) and speckle masking at optical wavelengths (Christou et al. 1992) confirmed the presence of this object. Near infrared diffraction-limited images indicated the presence of a massive disk surrounding both components (Malbet et al. 1993).

The nature of the infrared source was first discussed by Whitney et al. (1993). Spectropolarimetry of Z CMa showed that its polarized spectrum at quiet stages was *remarkably* similar to its spectrum at eruptive stages. Furthermore, the polarized spectrum of Z CMa was also very similar to that of MWC 1080, a Herbig Ae/Be star. These two results were interpreted as a consequence of the existence of an asymmetrical, geometrically variable, *dust cocoon* around the infrared, more massive, Herbig-like star (hereafter *primary*). The variability of Z CMa could then be explained by changes in the state of the secondary and the variable geometry of the dust cocoon (Hartmann & Kenyon 1996b). The primary was first imaged at optical wavelengths via speckle masking observations (Barth et al. 1994, Thiebaut et al. 1995). These observations supported the previous idea that some of the light from the primary is scattered towards our line of sight by a dust cocoon around the primary. From the SED measured by Thiebaut et al. (1995), a first characterization for Z CMa was obtained. The best fit for the secondary star produced $L_{acc} = 1300 \pm 20 L_{\odot}$ and $R_{\star} = 13 \pm 1 R_{\odot}$, where L_{acc} is the luminosity of the accretion disk associated to the secondary, and $R_{\star}$ is the stellar radius. According to these calculations, an accretion rate of $\dot{M} \sim 1.5 \cdot 10^{-4} M_{\odot} \mathrm{yr}^{-1}$ was obtained, assuming $M_{\star} = 3 M_{\odot}$ (see van den Ancker et al. 2004), where $M_{\star}$ is the mass of the secondary. Speckle polarimetry at mid-infrared wavelengths showed that both components of Z CMa are actually polarized (Fischer et al. 1998). According to their models, an inclined thick flared disk with a small opening angle can produce a significant amount of polarization at near infrared and a small amount of polarization at optical wavelengths.

Comparisons between observations and new evolutionary models (van den An-

cker et al. 2004) produced a different scenario, with an accretion disk with atmosphere surrounding the primary. This disk must then be inside of the dust cocoon that surrounds the primary. According to these calculations, the secondary is a $3M_{\odot}$, $L = 28L_{\odot}$ FU Ori star, and the primary is a $16M_{\odot}$, B0 IIIe star on the birthline with an age of 3×10^5 years, a radius of 7.6 $R_{\odot}$ and a luminosity of $L \approx 47L_{\odot}$. Alonso-Albi et al. (2009) obtain a mass of $12M_{\odot}$ for the primary star, and suggest the existence of a possible circumbinary (inclined) disk.

Poetzel et al. (1989) reported the first detection of the large jet associated to Z CMa. This jet has a position angle of 240° from north to east and a total length of 3.6 parsecs (assuming a distance to Z CMa of 1150 pc). Its south-west and north-east sides are blue and red -shifted, respectively. Integral field spectroscopy at optical wavelengths showed a micro-jet associated to the primary star (Garcia et al. 1999). Velázquez & Rodríguez (2001) presented interferometric measurements with the Very Large Array (VLA) at 3.5 cm and 6 cm, showing that, at these wavelengths, the large jet has its origin on the secondary star. High resolution images at J and H band (Millan-Gabet & Monnier 2002) showed an extended feature which was attributed to the walls of the cavity carved out by the large jet, were the light is scattered towards our line of sight. Furthermore, it was found that the primary was dominating at H band, in contrast to previous measurements, where the primary dominated only longwards of K band. Finally, as another proof of the complexity of Z CMa, Whelan et al. (2010) finds out that there are two jets associated to this system: the parsec sized one, which now is clearly associated to the primary, and another micro-jet, associated to the secondary. Moreover, these new measurements suggest the presence of a third companion, yet undetected.

In 2008 Z CMa suffered the strongest outburst ever reported for this target. After increasing its visual apparent magnitude by a factor of 3, the system decreased its brightness to its *quiet* (m_v = 10.2) level. The nature of this outburst is still under debate, and it is not clear wether its origin was a real outburst associated to the primary (Benisty, M. et al. 2010), or the increase in luminosity at optical wavelengths is due to the presence of a new hole in the dust cocoon, pointing at our line of sight (Szeifert et al. 2010). A very simplified scheme of the current picture of Z CMa is shown in Fig. 4.1. Currently Z CMa is experiencing a new, stronger outburst, which started at mid 2010 and last until current date (see Fig. 4.2).

The complex nature of this system, with two close young stars, makes imaging polarimetry a very interesting tool to better characterize it. While several authors have reported polarization images of circumstellar environments around young stars (i.e., Kuhn et al. 2001, Hinkley et al. 2009, Oppenheimer et al. 2008), there are not imaging polarimetric observations of Z CMa to date. In this paper we present imaging polarimetry of Z CMa obtained with ExPo, currently a visitor instrument at the 4.2 meters William Herschel Telescope (WHT). At the time of our observations, Z CMa was again at its minimum state (see the light-curve shown Fig. 4.2), having an apparent visual magnitude of about $m_v \approx 10.2$. We describe the observations, the instrument and the data reduction in §2. The image analysis and models are discussed in §3. The discussion and conclusion are written in §4 and §5, respectively.

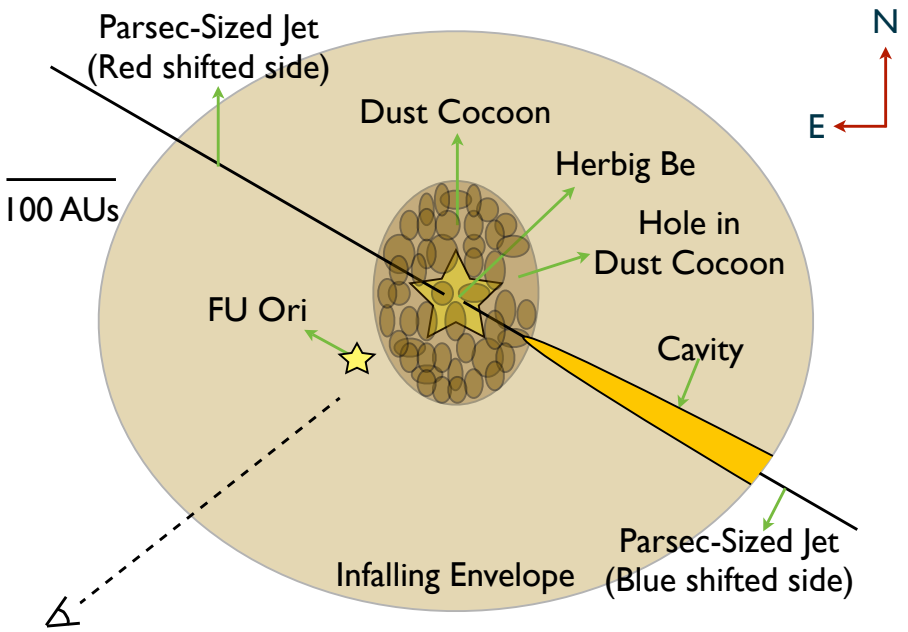

Figure 4.1: Schematic picture of the Z CMa system. The two stars are separated by ~ 0.1″. The two stars are separated by 100 AUs (based on a distance to Z CMa of 1150 pc).

4.2 Observations and Data Processing

Z CMa was observed on the 30th of December, 2009 (Night 1) and the 4th of January, 2010 (Night 2), during the third campaign (27/12/2009 – 04/01/2010) of ExPo as a visitor instrument at the WHT. The seeing during these two nights was fairly bad, with an average of ~ 1.47″. An unpolarized, diskless star (G 91-23) was observed the night of the 31st of December, 2009 for comparison purposes. No filter was used during all these measurements, so the full optical range was covered (the ExPo EM-CCD is sensitive to the wavelength range from 400 to 900 nanometers). Table 4.1 summarizes these observations. A set of calibration flat-fields was taken at the beginning and the end of each night, and a set of dark frames was taken at the beginning of each observation.

Target	Date	No Exp.	Average Seeing [″]
Z CMa	30 Dec 2009	4×18000	1.51
	4 Jan 2010	4×20600	1.44
G 91-23	31 Dec 2009	4×4095	0.95

Table 4.1: Summary of ExPo observations. The exposure time for each single frame was 0.028 seconds in all cases. No filter was used in any of these observations. G 91-23 is an unpolarized, diskless star, observed to compare with our Z CMa data.

4.2.1 Instrumental Description

ExPo is a dual-beam imaging polarimeter working at optical wavelengths. It combines a fast modulating ferroelectric liquid crystal (FLC), a cube beamsplitter (BS) and an EM-CCD. The FLC modulates the polarization state of the incoming light by 90° every 0.028 seconds, switching between two states "A" and "B". The beamsplitter divides de incoming light into two beams (*left* and *right* beams) with orthogonal polarization states, which are then imaged onto the EM-CCD. At the end of one FLC cycle, four different images, $A_{\rm left}, A_{\rm right}, B_{\rm left}, B_{\rm right}$ are produced. By subtracting the two simultaneous images recorded at the "A" and "B" states a "difference", linearly polarized image, is produced:

$$\Delta A = A_{\rm left} - A_{\rm right}, \tag{4.1}$$

$$\Delta B = B_{\rm left} - B_{\rm right}. \tag{4.2}$$

Because of the fast modulation of the FLC and the combination of two simultaneous images with opposite polarization states, most of the instrument systematic errors such as the highly static speckle noise (see, for instance, Racine et al. 1999, Sivaramakrishnan et al. 2002, Soummer et al. 2007) are removed, allowing us to increase our sensitivity to faint features. ExPo is sensitive to whole optical range, from 400 to 900 nm. A set of narrowband and broadband filters is implemented by a filter wheel, though none of these filters were used in the observations presented here.

4.2.2 Data Analysis

All our observations were processed according to the data reduction approach described by Canovas et al. (2011c). Each one of the four images produced after one FLC cycle is finished are individually corrected of dark, bias, flat-field and cosmic rays. These images are then aligned according to a template point spread function (PSF). The short exposure time used by ExPo (0.028 seconds) allows us to minimize the tip-tilt error of the wavefront by properly aligning our images. The final full width half maximum (FWHM) of our average PSF after centering is then $\sim 1.2''$, which supposes an improvement of about $\sim 20\%$ with respect to the average seeing during our

observations. A polarization image is obtained from a "double-difference" (Hinkley et al. 2009, Canovas et al. 2011c):

$$P_I^{'} = 0.5\,(\Delta A - \Delta B) = 0.5\Big((A_{\rm left} - A_{\rm right}) - (B_{\rm left} - B_{\rm right})\Big). \tag{4.3}$$

$P_I^{'}$ is a polarized, yet uncalibrated, image. Most of the unpolarized light and systematic errors are effectively removed in this double-difference image. Instrumental and sky polarization are corrected afterwards. The intensity image is calculated as the sum of the four images:

$$I = 0.5\Big(A_{\rm left} + A_{\rm right} + B_{\rm left} + B_{\rm right}\Big). \tag{4.4}$$

Because of ExPo does not have a de-rotator, sky rotation must be corrected during the data reduction so that the Stokes parameters Q and U can be calculated in a reference frame fixed to the observed target. A standard ExPo observation comprises at least 4095 images (~2 minutes) recorded at one fixed FLC position. Four sets of measurements with the FLC oriented at 0°, 22.5°, 45°, and 67.5° were recorded during each observation. Two calibrated datasets, Set 1 and Set 2, were produced after combining and calibrating the FLC positions 0°, 22.5° and 45°, 67.5°, respectively. The calibration procedure is described in detail in Rodenhuis et al. (2011a). The polarized intensity (linearly polarized light) was calculated as $P_I = \sqrt{Q^2 + U^2}$, and the degree of polarization as $P = P_I/I$, where I is the total intensity. To minimize the sky contribution when computing P, the sky intensity was calculated as the median value of three different sky areas of our images, and then subtracted from the intensity images. The polarization angle, $P_\Theta = 0.5 \cdot \arctan\left(\frac{U}{Q}\right)$ defines the orientation of the polarization plane. The error on the polarization angle depends on the error of the calibration process, but also on the region of the image where it is calculated. To minimize errors, the stokes Q and U images are binned with a 5×5 pixel box before P_Θ is computed. Furthermore, P_Θ is calculated only in the regions of the image with a signal-to-noise ratio (SNR) higher than 3 to reduce the error introduced by the noise. The accuracy of P_Θ depends then on the position of the image where it is calculated. For Z CMa, the maximum error that we obtain for P_Θ is of the order of ±3.8° in the regions with SNR above 3.

4.3 Results

A total amount of four calibrated datasets for Z CMa (two per night), and two calibrated datasets for the diskless, unpolarized star were obtained. Data from Night 2 shows a better SNR than data from Night 1: the Moon was closer to Z CMa in Night 1, increasing the amount of sky background noise. Therefore, we will focus our analysis on the first of the two datasets obtained during Night 2, which is the set with higher SNR.

Figure 4.3 shows a comparison between Z CMa and a diskless, unpolarized star (G 91-23). The first column, starting from the left side, shows the intensity for both stars.

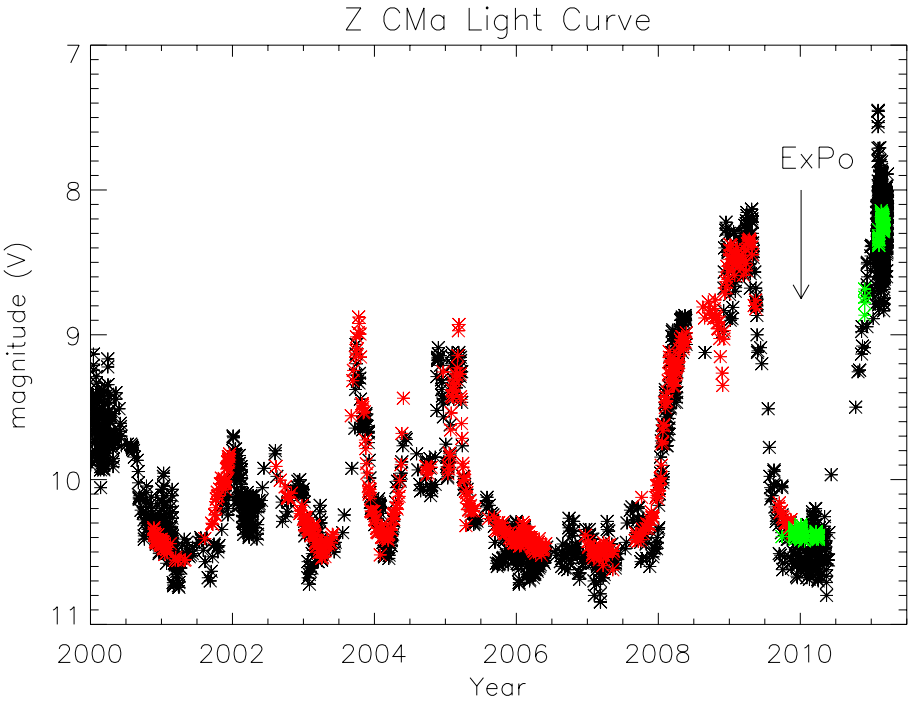

Figure 4.2: Light Curve of Z CMa. Black and red asterisks correspond to data from the American Association of Variable Star Observers (AAVSO) and the All Sky Automated Survey (ASAS) (Pojmanski 2002), respectively. Green asterisks correspond to data from the Czech Astronomical Society (CAS).

The two components of Z CMa appear unresolved in our images. There is almost no difference between Z CMa and G 91-23 in this image, apart from the difference in brightness. The second and third columns show the stokes Q and U parameters, respectively. In the case of Z CMa, an extended, butterfly-like pattern is evident, while in the case of G 91-23 these two images are dominated by remnant noise. The fourth column shows the polarized intensity, P_I, in which a very different pattern for each star is also clear. In the case of G 91-23, the P_I image is dominated by photon noise. This noise is signal-dependent, which means that its amplitude is proportional to the amount of photons. Therefore, the photon noise is higher at the center of the image, where the intensity is higher as well. This appears as the polarized signature that we see in this image. The pattern that we see here is very similar to a PSF, being centrosymmetric, and with its higher values at the center position. This is expected in case there is not any polarizing structure in the observed star. However, the P_I image looks very different in Z CMa. In this case, P_I shows a very strong asymmetry, with two extended features towards the West direction (to the right side of the image), and the South-West (to the bottom-right corner of the image). Because of the small

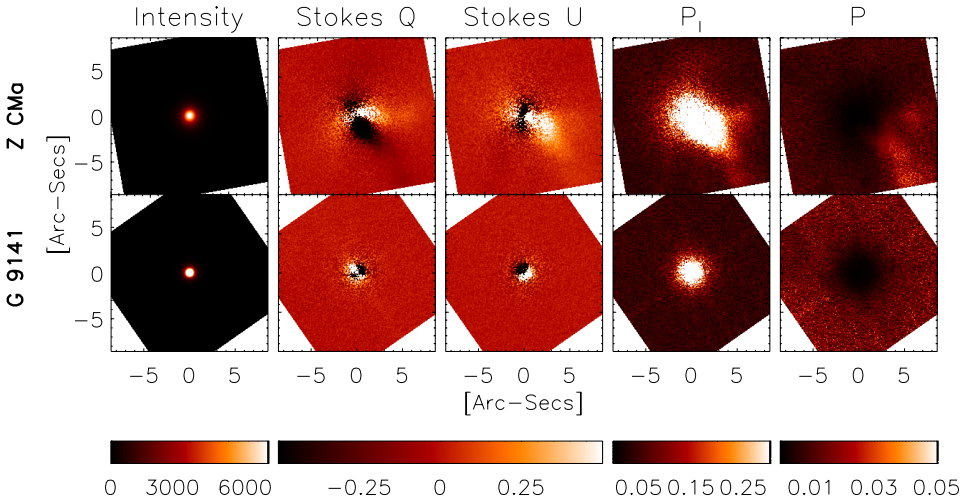

Figure 4.3: Comparison of Z CMa (top row) and G 91-23 (unpolarized, diskless star, bottom row). Starting from the left, the first column shows the total intensity image. The second and third column show the Stokes Q and U parameters, respectively. Both images show an extended butterfly pattern in Z CMa, produced because of the circumstellar (polarizing) dust around this object, while in the case of G 91-23 there is just remnant noise. The polarized intensity (P_I) is shown in the fourth column. G 91-23 shows a centrosymmetric pattern, as expected for an unpolarized, diskless star. Z CMa shows an extended, asymmetrical structure, with two extended features towards West (right side of the image), and South-West (bottom-left corner). The fifth column shows the degree of polarization (P). Z CMa shows again these two extended, polarized features, while G 91-23 does not show any polarizing feature, as it happens with its P_I image. The units of the color bars are given in arbitrary units. Our images are calibrated with respect to the reference system of the observed object (see §2). North is up and East is left in all the images.

separation of the two stars, it is impossible to resolve the dust cocoon around the primary in our images. Therefore, the extended polarized pattern that we see in Z CMa is probably caused by the circumbinary disk and infalling envelope. The fifth column shows the degree of polarization ($P = P_I/I$) of Z CMa and the comparison star. As it happens with the polarized intensity, the unpolarized star does not show any spatial structure but a centrosymmetric pattern. P uniformly increases from the center, where I is higher, to the outermost regions where I is much lower and the image is dominated by noise. The image of Z CMa, however, shows again two polarization features, oriented to West and South-West, respectively.

Further analysis shows that these two polarized structures appear at the same position in all the observations of Z CMa, as is shown in Fig. 4.4. Z CMa was observed at a different altitude during Night 2, resulting in the same polarization image. In

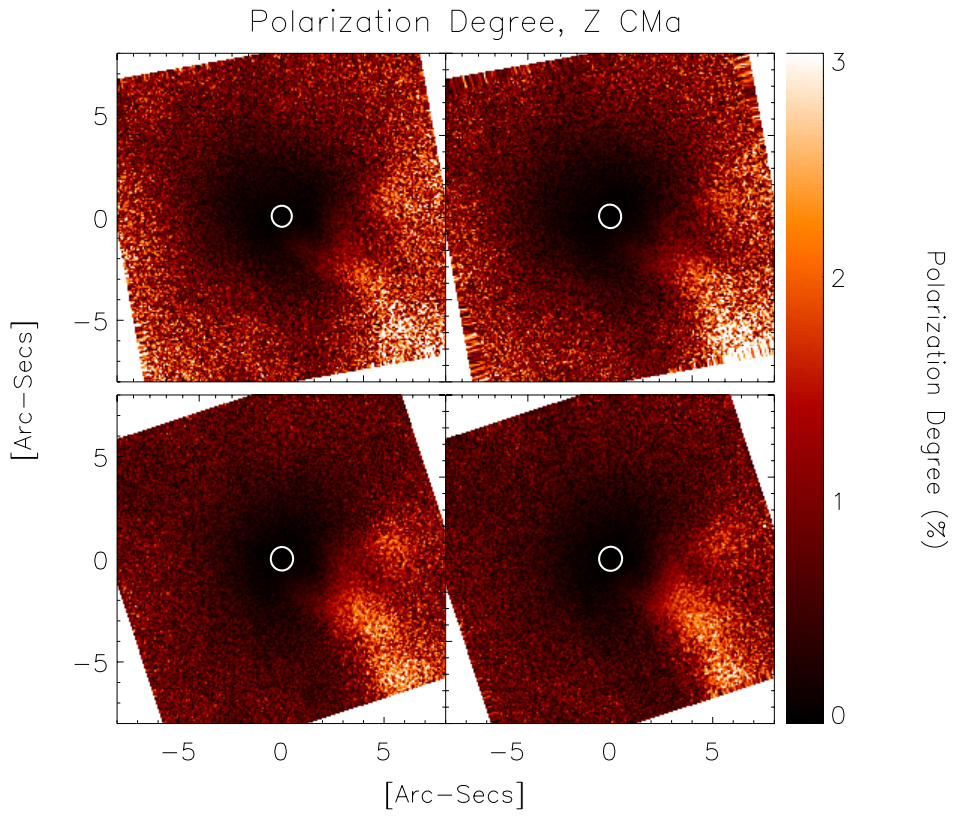

Figure 4.4: Degree of Polarization of Z CMa in four datasets. Top: data from Night 1. Bottom: data from Night 2. For all images: North is up, East is left. All the images are re-scaled to better show the common polarization jet-like features. White contours show the FWHM of the PSF for each image. The Moon was closer to Z CMa in Night 1, this explain the higher amount of noise in the data from that night.

case these two polarized features were caused by internal reflections or another instrumental artifacts, they should appear in different positions when comparing images from Night 1 with images from Night 2. This rules out the possibility that these two features are caused by any instrumental or data processing artifact.

The left side of Fig 4.5 shows P, P_Θ, and the trajectory of the large jet in Z CMa, indicated by the white dashed line. The position of the primary and the secondary is marked by the two green crosses at the center of the image. The polarization angle (P_Θ) is calculated only in the regions of the image with SNR higher than 3. This image shows that there are three distinct regions in Z CMa which each have very different values of P_Θ, in contrast to previous spectropolarimetric studies which reported only the spatially integrated value for P_Θ (Whitney et al. 1993, Szeifert et al. 2010).

This result is illustrated in Fig. 4.5, where three different areas are contoured by black (labelled as "1"), green (labelled as "2") and white (labelled as "3") lines. The white and black areas indicate the regions where P_Θ has a mean value of 133° and 147°, respectively. The green line defines a region with lower degree of polarization than the other two, but with a SNR still well above the noise. P_Θ inside this area has a mean value of 186°. The mean and standard deviation, σ, of P and P_Θ was calculated separately for each one of these three regions. This is shown in Table 5.2.

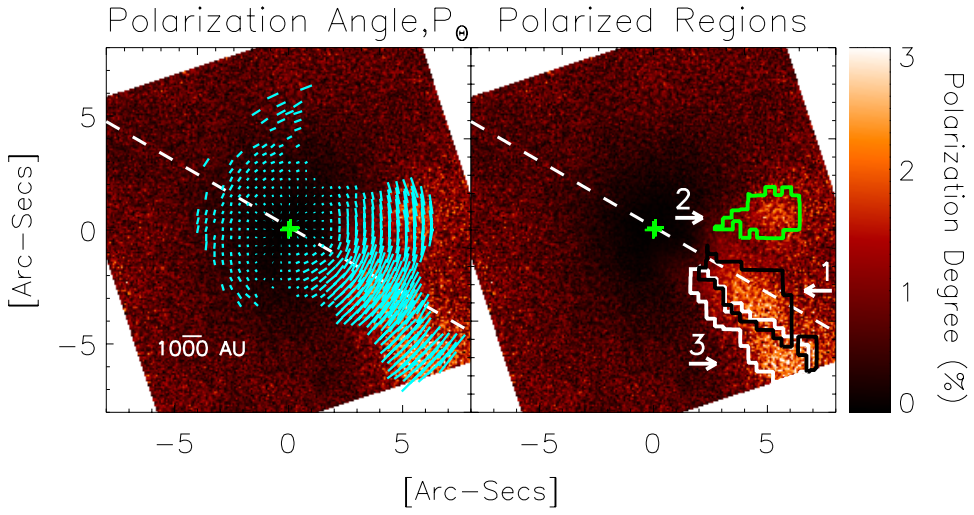

Figure 4.5: For both images: degree of polarization of Z CMa. The white line shows the trajectory of the optical jet, at a P.A. of 240° measured from North to East, and the two green crosses show the position of the primary (top-right) and the secondary (center). Left image: The polarization angle (P_Θ) is shown by the the bluish-green vectors. Only regions with SNR higher than 3 are taken into account when calculating P_Θ. The distance scale shown by the white line was calculated assuming a distance to Z CMa of 1150 pc. Right image: the regions with higher SNR (labeled by the numbers 1,2,3), according to their average values of P_Θ are shown. The black contour (labelled as "1') shows the region where the average P_Θ is 147° ±4.3°. P_Θ in this area is almost perpendicular to the large jet. The green area (labelled as "2") shows the region where P_Θ has an average value of 186° ± 3.6°. White contours (labelled as "3") contain the region where the average P_Θ is 133° ± 3.5°.

4.4 Discussion

Z Cma was observed with ExPo during its last minimum. According to the current model (see Fig. 4.1), this implies that the primary star is obscured from sight, i.e., the medium is optically thick in the line of sight between the primary and us. At this

Label	Color	P[%]	σ	P_Θ [°]	σ[°]
Region 1	Black	2.1	0.7	147	4.3
Region 2	Green	1.1	0.6	186	3.6
Region 3	White	1.8	1.2	133	3.5

Table 4.2: Mean and standard deviation, σ, of P and P_Θ in the three different regions shown in the right image of Fig. 4.5. The angles are calculated from North (up) to East (left).

stage, the primary contributes about 20% of the total flux at optical wavelengths, and all its light is linearly polarized by the dust cocoon which surrounds it.

Our images show three different regions, which are classified according to their polarization angle (P_Θ). The regions labeled as "2" and "3" (green and white areas, respectively) have a polarization angle that have not been reported in previous spectropolarimetric measurements. We discuss possible sources of these three polarized features below.

4.4.1 Region 1

The polarization angle (P_Θ) inside this area is almost perpendicular to the direction of the blue-shifted side of the parsec-sized jet, as it is shown in the left image of Fig. 4.5. Moreover, this region follows the trajectory of the jet, as it can be seen on the right image of Fig. 4.5 (black contoured area). Whitney & Hartmann (1993) show that the polarization pattern that we measure in this region, with P_Θ perpendicular to the jet direction, is indeed the expected pattern when observing an infalling dust envelope with a cylindrical cavity carved out by a well-collimated jet.

Previous spectropolarimetric studies at optical wavelengths (Whitney et al. 1993, Szeifert et al. 2010) have reported a polarization angle perpendicular to the direction of the parsec-sized jet. The average P and P_Θ that we measure in this region are in good agreement with these previous observations, as it is shown in Table 4.3. However it should be noted that previous measurements were done with a different technique (i.e., we are comparing *spectropolarimetry* with *imaging polarimetry*)

These results clearly suggest that this polarized feature is caused by the jet, which is carving out a cavity on the dust envelope which surrounds the whole system. We therefore point to the large jet associated to the primary as the origin of the polarization pattern observed along the Region 1 of our images.

4.4.2 Region 2

The polarization angle of this area (Fig. 4.5, green contour) is very distinct from the polarization angles measured in previous observations. The location of this region is not close to the the jet trajectory, and there is a *depolarization* lane (where P is almost negligible when compared with any of the three regions discussed here) between Region 1 and this region. Therefore, we argue that this polarized feature is not

Measurement	P[%]	P_Θ [°]
Whitney et al. (1993)	2.0 ± 0.005	150 ± 1.5
Szeifert et al. (2010)	2.6 ± 0.1	160 ± 1
ExPo (Region 1)	2.1 ± 0.7	147 ± 4.3

Table 4.3: Comparison of previous spectropolarimetric measurements of Z CMa and ExPo results for *Region* 1 (black contoured region). P and P_θ are average values in all cases. Notice that the ExPo values come from *imaging polarimetry*, while the other values come from *spectropolarimetric* observations.

related to the large jet. To explain its origin, we consider here the possibility of a hole in the dust cocoon surrounding the primary star pointing to the West. Some of the outbursts of Z CMa, as well as the spectropolarimetric measurements of this system, can be explained (Whitney et al. 1993, Szeifert et al. 2010) by the formation of holes in the dust cocoon surrounding the primary: in case there is a hole in the dust cocoon in our line of sight, then an increase in the amount of light from the primary as well as a decrease on its polarization degree is expected.

To understand the impact of a hole in the optically thick dust cocoon surrounding the Herbig Be star, we model, using the MCMax radiative transfer code (Min et al. 2009b), a pencil beam of light emerging from the dust cocoon which then is scattered towards the observer by a surrounding infalling molecular cloud.

Model Setup

We have simulated a binary system placed at a distance of 1150 pc (a value which agrees to the approximate distance to Z CMa), comprising an FU Ori star ($M = 3M_\odot, L = 27.5L_\odot$) and a Herbig Be star ($M = 13M_\odot, L = 55000L_\odot$) surrounded by an optically thick dust cocoon. The binary system is surrounded by a large infalling molecular envelope. The dust cocoon surrounding the Herbig Be star is modelled as an optically thick spherical shell with a hole with an opening angle (ϕ) varying from $\phi = 5°$ to $\phi = 10°$. This cocoon is 50 AUs in radius, starting at a distance of 20 AUs from the primary, which is the dust sublimation radius for this star. Two different orientations for this hole were computed, one producing *forward* scattering and the other producing *backward* scattering. The infalling envelope is modelled as an optically thin spherical shell with a density distribution described by Dominik & Dullemond (2008), based on the work of Ulrich (1976) and Terebey et al. (1984). In this model, the infalling envelope is made from the leftovers from the collapse of a rotating cloud. The angle between a point on the envelope, the center of the envelope, and the rotational axis defines de polar coordinate θ. According to this model, the gas density ρ at a polar angle $\mu = \cos\theta$ and a distance to the center r is given by:

$$\rho(r,\theta) = \frac{\dot{M}}{4\pi\sqrt{GMr^3}}\left(1+\frac{\mu}{\mu_0}\right)^{-1/2}\left(\frac{\mu}{\mu_0}+\frac{2\mu_0^2 r_{centr}}{r}\right)^{-1}, \tag{4.5}$$

where μ_0 is the solution of the equation

$$\mu_0^2 = 1 - \frac{r}{r_{centr}}\left(1 - \frac{\mu}{\mu_0}\right). \tag{4.6}$$

$\dot{M}$ represents the infall rate and r_{centr} is the centrifugal radius, which here is fixed at a distance of 200 AU, as it happens in the model of Dominik & Dullemond (2008). Four different values of $\dot{M}$ ($1, 2, 4, 8 \times 10^{-7}$ $M_\odot$ yr^{-1}) were computed in our simulations. To easily distinguish between the different models we use the following notation: "Model 1(5b)" refers to the model with $\dot{M} = 1 \cdot 10^{-7} M_\odot \mathrm{yr}^{-1}$, $\phi = 5$, backward scattering; "Model 4(10f)" refers to the model with $\dot{M} = 4 \cdot 10^{-7} M_\odot \mathrm{yr}^{-1}$, $\phi = 10$, forward scattering, and so on. The composition of the dust in the infalling envelope is described by Min et al. (2011c), which is based on the Solar composition inferred by Grevesse & Sauval (1998b). The infalling envelope is composed by, in mass, 58% silicates, 18% iron sulphide and 24% amorphous carbon. The dust size distribution follows the standard MRN size distribution (Mathis et al. 1977). In this distribution the number density of the grains is equated by the following power-law with

$$n(a)\mathrm{d}a \propto a^{-3.5}\mathrm{d}a, \tag{4.7}$$

where a is the radius of the grains which ranges from 5 nm to 250 nm. The shape of the dust grains follows the distribution of hollow spheres (DHS, Min et al. 2005b), assuming an "irregularity parameter" $f_{max} = 0.8$.

The radiative transfer images of the Z CMa system modelled by MCMax are then convolved with the modelled Point Spread Function (PSF) of ExPo from Min et al. (submitted). The PSF is modelled with an average seeing of 1.4" and includes contributions from photon noise, readout noise, and instrumental polarization. To better reproduce the ExPo observations, the exposure time used for these PSFs is 0.028 seconds. The resulting PSF is then a speckle pattern, similar to what we obtain with ExPo observations. A set of 100 statistically independent PSFs was generated. A total amount of 10000 images, each one of them with different photon noise, were simulated by convolving the images produced by the MCMax code with the set of simulated ExPo-PSFs. The resulting images were reduced in the standard manner with the ExPo data reduction approach described in §2.2 of this paper and Canovas et al. (2011c). After reducing these simulated images, the averaged PSF has a FWHM of $\sim$ 1.2", very similar to what we obtain after reducing our data. Both stars appear unresolved in the simulation, as it happens in our observations. The simulated images produce a polarized pattern consistent with the polarized feature observed in Region 2 of our images (green contoured area in Fig. 4.5).

To compare with the real images and decide which model is the more realistic, the mean value of the polarized regions in the simulated images was computed. As we did with the observations, only pixels of the image with SNR higher than 3 were used in this computation. Table 4.4 shows the average P of the final simulated-image for each one of the models described above. The average P that we obtain in Region 2 of our observations is 1.1% (see Table 5.2). After convolving our models with a

	Forward [%]		Backward [%]	
$\dot{M}[10^{-7}M_{\odot}\mathrm{yr}^{-1}]$	$P_{\phi=5}$	$P_{\phi=10}$	$P_{\phi=5}$	$P_{\phi=10}$
1	0.99	2.76	0.62	3.22
2	2.23	3.24	1.27	4.83
4	3.17	3.07	2.44	6.67
8	3.58	4.67	3.80	7.58

Table 4.4: Mean values of P for the different simulations performed here. ϕ stands for the opening angle (in *degrees*) of the hole in the dust cocoon. The simulated images are produced after convolving different models of Z CMa with a set of simulated ExPo PSFs. The average (simulated) PSF used for these simulations has a FWHM of 1.2″ after been realigned with the ExPo data reduction approach.

realistic PSF, the simulation which fits our observations best (i.e., the model which produces the more similar average P) corresponds to the model "Model 1(5f)". This model, shown in Fig. 4.6, produces an average P of 0.99% (see Table 4.4).

The two more similar results, corresponding to the models "Model 1 (5b)" and "Model 2 (5b)" are shown in Fig. 4.7. "Model 1 (5b)" produces an average P of 0.62%, which is below the value that we obtain in our observations in Region 2. "Model 2 (5b)" produces an average value of P of 1.27%, slightly higher than the value that we measure in Region 2. This model actually produces a very similar polarization pattern to what we observe. With the data that we have it is very difficult to decide which model is the more realistic when fitting our observations; both "Model 2 (5b)" and "Model 1(5f)" produce a very similar result. What we can conclude from both models is that the mass infall rate is in any case higher than $\dot{M} = 2 \cdot 10^{-7} M_{\odot}\mathrm{yr}^{-1}$.

To better understand to which degree does the seeing affect our images, the models were also convolved with a set of PSFs with $\sim$ 1.6″ FWHM (i.e., worst seeing than in our observations) and with a set of PSFs with $\sim$ 0.8″ FWHM (i.e., better seeing than in our observations). The models run with different seeing conditions fail to reproduce our observations. In the case of very poor seeing (average seeing $\geq$ 1.6″), the polarized feature produced by the hole in the dust cocoon becomes too weak, and it is undetectable in all the models. On the other hand, some of the models calculated with the good seeing PSF (FWHM of $\sim$ 0.8″) produce polarized patterns that fit well our observations, but this case is unrealistic given the seeing conditions that we had during our observations.

4.4.3 Region 3

Region 3 appears related to the optical jet, but is elongated in a direction that clearly deviates from the jet direction, specially close to the South-West edge of our image. The average polarization angle in this region (P_{Θ} = 133°) is not perpendicular to the jet, which also suggest a different nature than the polarized feature of Region 1. One possible explanation of the origin of this feature might involve a jet-cloud interaction. Adaptive optics assisted [Fe$_{\mathrm{II}}$] spectro-images (Whelan et al. 2010) show

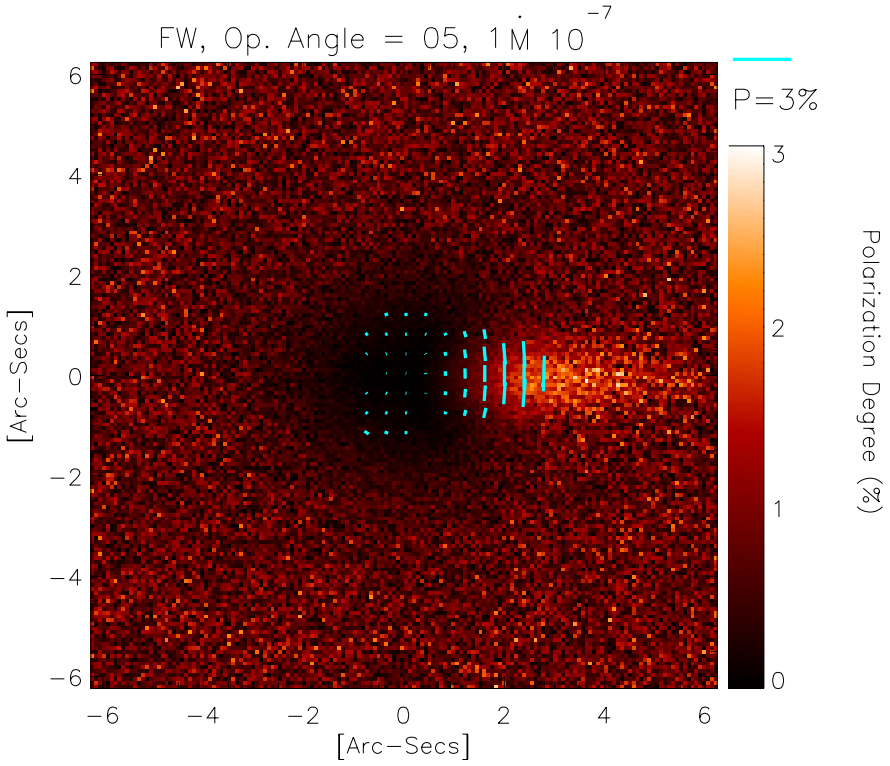

Figure 4.6: Best fit for the Z CMa-Region 2 simulation. The polarization pattern is the product of a hole on a dust cocoon surrounding a Herbig Be star. Because of this , a pencil of light scapes and gets scattered towards our line of sight by the dusty infalling envelope which surrounds the system. The mass infalling ratio is $\dot{M} = 2 \cdot 10^{-7} M_{\odot} \mathrm{yr}^{-1}$. The hole in the cocoon has an opening angle of 10° and it is oriented towards us (i.e., there is forward scattering).

the existence of several "knots" aligned with the large jet, very close the position of the primary, which supports the possibility of jet-cloud interactions. Previous studies of these kind of interactions (de Gouveia Dal Pino 1999, A. C. Raga et al. 2002) predict that during a jet-cloud collision, the jet can be deflected. As a consequence of this collision, the deflected jet can carve out a new cavity on the surroundings of the cloud. This scenario is then similar to the one proposed by Whitney & Hartmann (1993), but considering that the trajectory of the jet is now different, since it describes a curved trajectory. After certain time the cloud dissipates, and the jet recovers its original trajectory, but the effects of this collision on the cloud surrounding the jet can last according to the models mentioned above. The signature of an empty cavity close to the jet trajectory is then expected to be observed in polarized light, producing a polarization feature very similar to the one observed in Region 3 of our images.

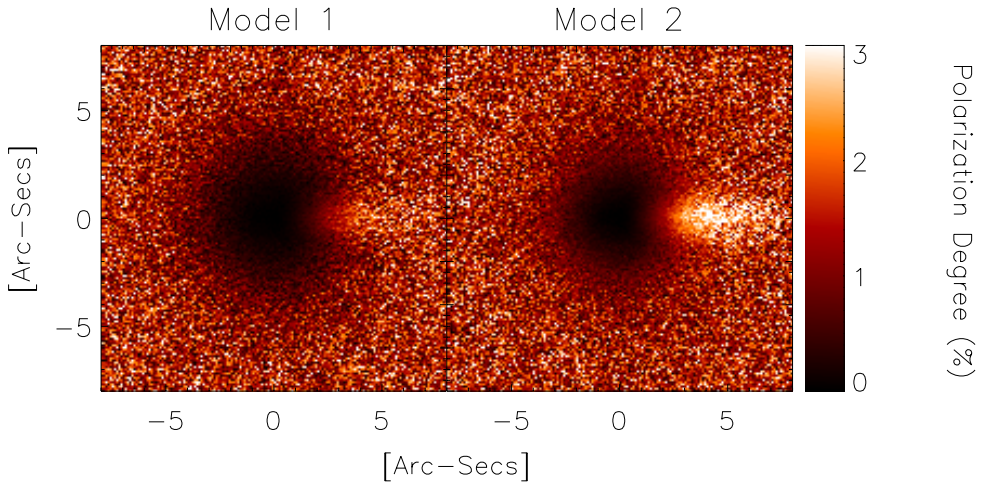

Figure 4.7: For both images: Model of binary system, with a dust cocoon around the more massive star. There is a hole on the dust cocoon, and the whole system is surrounded by an infalling mass envelope. Left: "Model 1(5b)". Right: "Model 2(5b)".

Another possible explanation for this feature is related to the collimation of the jet. According to the models of Whitney & Hartmann (1993), a more collimated jet will produce a cylindrical-shaped cavity, while a less collimated jet will produce a more open, conical-shaped cavity. In this case, the trajectory of the jet defines the axis of symmetry of P_Θ, which is perpendicular to the jet over this axis. The regions aside from the jet trajectory have a P_Θ which depends on the angular distance to the jet trajectory. However, this symmetry is not apparent in our images, and there is not a counterpart for Region 3 on the opposite side of the jet. Furthermore, because of the physical length of this jet which has been observed up to a distance of 1.6 pc in its blue shifted side (the side from center to the bottom-right corner in our images), it is very likely that this jet is highly collimated, favoring the cylindrical-shaped cavity against the conical-shaped one.

Finally, it is also possible that this polarized feature has its origin in another hole on the dust cocoon, as we suggest it is happening to explain Region 2 (see discussion above). The average P in this area is 1.8% (see Table 5.2). According to the values that we find in our simulations, listed in Table 4.4, the model "Model 2(5f)" can produce an average P of 2.23%. This is the closest value for the average P that we find in our simulations. If this is the case, Region 2 has to be caused by a hole facing away from us (i.e., causing backward scattering).

The nature of this feature makes it difficult to discriminate between the two possible explanations discussed here. While the similar values for the average P in Region 1 and Region 3, 2.1% and 1.8%, respectively, suggest a similar nature, pointing

towards the large jet as the source of this feature, the high standard deviation of this region (σ = 1.2%) advices us to be careful with this argument.

4.5 Conclusions

Our measurements, obtained with ExPo after the 2008 outburst, show three different features in polarization. Two of them, labeled here as "Region 2" and "Region 3" have not been reported before. This is due to the high polarimetric sensitivity of ExPo, and the different nature of our data, which employ imaging polarimetry rather than spectropolarimetry. We interpret our data as a new evidence of the presence of holes in the dust cocoon that surrounds the primary star.

The polarized feature labeled here as "Region 1" (black contoured area) shows an average polarization angle of $P_\Theta = 147° \pm 4.3°$, which is almost perpendicular to the direction of the large jet and it is very similar to the value found by Whitney et al. (1993) and Szeifert et al. (2010). The average degree of polarization, $P = 2.1 \pm 0.7\%$, is also very similar to the value found by Whitney et al. (1993) ($P = 2.0 \pm 0.005\%$), and slightly different to what it was found by Szeifert et al. (2010) ($P = 2.6 \pm 0.1\%$). However, this difference can be explained by the different methods used in previous studies, and due to the different state of Z CMa in these observations: Szeifert et al. (2010) observed Z CMa *during* its 2008 outburst, while our observations were done *after* that outburst. The orientation of P_Θ indicates that this polarized feature is indeed produced by the walls of a cavity carved out by the large jet. Furthermore, the orientation of this jet indicates that, in case it is produced by a disk, this disk is tilted with respect to our line of sight (i.e., there is not an edge-on disk around the primary). Benisty, M. et al. (2010) shows evidences of a tilted accretion disk around the primary, by analyzing the Br_γ emission line produced on the hot gas around this star. If this is the case, then the disk has to be inside of the dust cocoon which surrounds this star, to explain all the previous evidences of a dust cocoon around the primary.

Our analysis suggests that the polarized feature that we detect in Region 2 (green contoured area in Fig. 4.5) is caused by a hole in the dust cocoon surrounding the primary star. The idea of a hole in the dust cocoon is not new and it has been used to explain the variability and polarimetric properties of this system. However, in previous discussions, the hole in the cocoon was assumed to be in our line of sight to explain some of the outbursts of Z CMa. To fit our observations, a hole with a different orientation must be used: a hole in one side of the cocoon can produce a pencil beam of light that will be scattered to our line of sight, producing a polarized signature similar to what we observe in Region 2. To simulate this, we have run different models with different hole sizes, orientations, and different mass infall rates for the surrounding infalling envelope. According to our calculations and models, the mass infall rate of the infalling envelope cannot be higher than $\dot{M} = 2 \cdot 10^{-7} M_\odot \mathrm{yr}^{-1}$, and there is one hole in the dust cocoon oriented in our direction, producing forward scattering.

The nature of the polarized feature that we label as "Region 3" still remains unclear. Because of its average P, and its position close to the jet trajectory, it might be caused by an empty cavity carved out some time ago by the jet after an off-axis collision with a cloud. However, we cannot rule out the possibility that this feature has its origin on a different hole on the dust cocoon, which produces a pencil beam of light, in a similar way to what we think happens in Region 2.

Regions 2 and 3 require more observations for a proper analysis of our results. By combining polarimetric observations with different filters, we can better constrain the dust parameters, as well as the geometry of the scattering process (i.e., backward scattering versus forward scattering). Furthermore, future versions of ExPo will include an AO system, which will translate in a much better polarimetric performance. As discussed in §.4.2.1, the seeing is a very important factor to consider when comparing real data with our simulations. While the polarization angle, P_Θ is insensitive to it, the degree of polarization (P) is a quantity which is extremely dependent on the seeing conditions.

Z CMa is a very interesting system to perform imaging polarimetry studies. If the dust cocoon around the primary is rapidly modifying its geometry, then new holes (i.e., new polarized features) are expected to appear.

4.6 Acknowledgements

We are grateful to the staff at the William Herschel Telescope for their help during the during the observations.

I've loved the stars too fondly to be fearful of the night.
— Galileo Galilei

Chapter 5

Characterizing the neutral halo of BD+303639 via imaging polarimetry

H. Canovas *

Abstract

BD+303639 is a young Planetary Nebula with a Carbon-rich, Wolf Rayet central star. It shows evidence of a change in its chemistry: it was O-rich in the recent past, but at certain point its chemistry changed, and now it is a C-rich star. Here we present observations of BD+303639 with ExPo, a dual-beam imaging polarimeter that works at optical wavelengths. We constrain the properties (size and mass) of the neutral envelope of this Planetary Nebula by comparing our observations with models. The faint neutral halo around BD+303639 contains information about the change in the chemistry of its central star. Imaging polarimetry is an ideal tool to observe this environment, since the light scattered in the neutral halo becomes linearly polarized, and the light from the central star is largely unpolarized. The properties of the dust in the neutral halo can be derived from our imaging polarimetry data in the narrow-band H_α, H_α continuum, Na and Na continuum filters. We have also obtained broadband imaging linear polarization images with the Sloan R and Sloan I filters. We model our observations with a polarized radiative transfer code that takes into account different grain sizes and morphologies. Our results show that the O-rich ring that surrounds BD+303639 extends up to a distance of 6500 AU from the central star. We derive a total mass for the O-ring of $2.1 \cdot 10^{-2} M_\odot$, and a mass loss rate during the O-rich period of $3.9 \cdot 10^{-5} M_\odot yr^{-1}$. Assuming an expansion velocity of 22 km/s, we conclude that the period of strong mass loss during the O-rich phase lasted 1400 years.

*In preparation, to be submitted.

5.1 Introduction

Planetary nebulas (PNs) are the product of the severe mass loss that occurs in the final stages of the evolution of intermediate ($1 - 8M_{\odot}$) mass stars (Weinberger & Kerber 1997). At this stage, convection brings heavy elements such as C,N and O to the surface of the star. The strong wind produced at the end of the AGB phase sends the outer atmospheres of these stars into interstellar space, revealing their inner nucleus. When the star leaves the AGB phase, its temperature increases considerably, and the remnant material, which has previously been ejected, becomes ionized. At this point, the surrounding material becomes visible at optical wavelengths: a PN has been born. Studies of PNs span cover the electromagnetic spectrum from radio wavelengths (e.g., Taylor et al. 1987) to X-rays (Kreysing et al. 1992, Kastner et al. 2000).

The study of PNs provides critical insights into the history of their central stars and thereby adds crucial information to our understanding of stellar evolution. One of the main problems faced when comparing PN observations to evolutionary models of stars is the difficulty to detect the non-ionized (neutral) halos of the PNs. Neutral halos are the oldest, outermost regions of the PN, and they are formed by the material ejected by the central star in the early stages of the AGB phase. Their study and comparison with the younger, ionized regions of the PNs, leads to a better understanding of the evolution of the central star during the AGB phase (Huggins et al. 1996). Unfortunately, because of the intrinsically low brightness of the neutral halos, it is difficult to probe their physical properties. Different methods have to be used to measure their properties (for a discussion about different methods used in the past to measure neutral halos see Dinerstein 1991). Polarimetry is a powerful tool to detect and characterize these halos. By removing the largely unpolarized light from the central star and the ionized region, the neutral halo can be more easily detected. Furthermore, polarimetry can provide information on dust grain size and composition.

In this paper we present the first imaging polarimetry observations of BD+303630 at optical wavelengths. BD+303639 is one of the best studied planetary nebulas, and is known to have an extended neutral halo. The polarized images produced by ExPo (Rodenhuis et al. 2011b, Canovas et al. 2011c), a dual-beam imaging polarimeter, allow us to characterize the neutral envelope of BD+303639 at optical wavelengths.

BD+303639 (Campbell's hydrogen star) is a low excitation, young planetary nebulae. Its central star, a late-type carbon-rich Wolf-Rayet star [WC9], is a scaled version of the more massive Wolf-Rayet HD 164270 (Smith & Aller 1971, Crowther et al. 2006, Crowther 2008). The first attempts to measure its distance produced values smaller than 1 kpc (see, for instance, Underhill 1983, Sabbadin 1984, Acker et al. 1992). Proper-motion measurements produced substantially larger distances: 1.5 ± 0.4 kpc (Kawamura & Masson 1996) and 2.68 ± 0.810 kpc (Hajian & Terzian 1994). The radiative transfer model discussed by Siebenmorgen et al. (1994) suggests a distance ≥ 2 kpc. The most recent study, based on Hubble Space Telescope (HST) data from two different epochs, derives a distance of 1.2 kpc (Li et al. 2002). As a consequence

of the different distances calculated for BD+303639 during the past years, the stellar parameters derived for its central star differ accordingly to the distance chosen for the calculations. Based on the distance reported by Li et al. (2002), Crowther et al. (2006) derived $R_\star = 0.85 R_\odot$ and $L_\star = 6027 L_\odot$ for the central star.

The ionized shell of BD+303639 is known to be a source of X rays (Kreysing et al. 1992, Kastner et al. 2000, 2002). The size of this shell is $5'' \times 4''$ (Li et al. 2002) at optical wavelengths, and it has an expansion velocity of 22 ± 4 km s^{-1} (Mellema 2004). This value is much smaller than the expansion velocity measured for the neutral gas (Bachiller et al. 1992, 1991). Bernard-Salas et al. (2003) presents a detailed description of the spectra of BD+303639 from ultraviolet (UV) to infrared (IR) wavelengths. The electron density and temperature inside the shell derived from this work are $11,000 \mathrm{cm}^{-3}$ and 8,500 K, respectively.

Emission lines of molecular hydrogen (H_2) indicated the presence of neutral gas in the nebula of BD+303639 (Beckwith et al. 1978). Pwa et al. (1986) suggest that a neutral halo must exist to explain the low mass of the ionized material found in this object. Dinerstein & Sneden (1988) reports the first measurements of the *scattering* of the sodium D lines ($\lambda\lambda 5890, 5895$) in the neutral halo of this object. Furthermore, measurements of the 21-cm line of hydrogen also confirmed the presence of a neutral envelope (Taylor et al. 1990). Observations at millimeter and sub-millimeter wavelengths with the *James Clerck Maxwell Telescope* (JCMT) allowed Hoare et al. (1992) to resolve, for the first time, the cool dust in the neutral regions of BD+303639. Based on these and previous observations at infrared wavelengths, a first model of the dust in this PN was developed. The dusty halo of BD+303639 was imaged for the first time at optical wavelengths by Harrington et al. (1997). In this work, VLA radio measurements were combined with narrow-band images taken with the HST to map the selective extinction $E_{\beta-\alpha}$. As a result, a more elaborate model of the dust in the neutral envelope was produced. Recent measurements at near infrared (NIR) wavelengths show that the halo extends to larger distances than measured before (Phillips & Ramos-Larios 2007).

BD+303639 caught the attention of the astronomical community when (Waters et al. 1998a) showed that the ISO spectrum contains features of both silicates (associated with O-rich chemistry), and PAHs (which indicate a C-rich chemistry). Later on it was discovered that other PNs with [WC] central stars showed the same behavior (i.e., Cohen et al. 1999). More recently, Matsumoto et al. (2008) found for the first time silicate absorption features in the mid-infrared spectrum of BD+303639. A late thermal pulse at the very end of the AGB phase can explain the source of this dual-chemistry nature (see Zijlstra et al. 1991, Leuenhagen et al. 1996, Waters et al. 1998a, Herwig et al. 1999).

The polarimetric data presented in this paper allow us to constrain the dust properties of BD+303639. We compare two different models to our images obtained with the H_α and H_α continuum filters. To account for the O- and C- rich nature of this target, we model an outer ring composed of O-rich dust, and an inner ring composed of C-rich dust. Comparisons with these models allow us to constrain the size of the O-rich shell. Based on this, we calculate the mass loss rate of the star during its

earlier, O-rich stage. The observations, instrumentation used and data reduction are described in §2. The model is explained in §3. The discussion and conclusions are presented in §4 and §5, respectively.

5.2 Observations and Data Reduction

BD+303639 was observed as part of the"Evolved Stars" campaign of ExPo at the William Herschel Telescope (WHT). During this campaign, several post-AGB stars were observed. The seeing during these three days was fairly good, with an average value of 0.9". The narrow band filters used here (H_α,H_α continuum, Na and Na continuum) were manufactured by Andover Corporation. The Sloan R and Sloan I (Fukugita et al. 1996) broadband filters were also used during our observations. A diskless, unpolarized, star (HD122815) was used for comparison purposes. A set of dome flat-fields was taken in the beginning and at the end of each night. A set of dark frames was taken at the beginning of each set of observations. A summary of the observations presented here is shown in Table 5.1.

5.2.1 ExPo: The instrument

ExPo (Rodenhuis et al. 2008b, 2011b) is a dual-beam imaging polarimeter, which is optimized for the detection of the (linearly) polarized light that originates in different circumstellar environments. This instrument works at optical wavelengths, being sensitive to linearly polarized light from 400 to 900 nm. The main components of ExPo are a ferroelectric liquid crystal (FLC), a cube polarizing beamsplitter (BS) assembly and an electron-multiplying (EM) CCD camera. The FLC changes between two states, "A" and "B" every 0.028 seconds. The B state rotates the polarization plane of the incoming light by 90° with respect to the "A" state. The beamsplitter divides the incoming light into two beams ("left" and "right") with orthogonal polarization states. The two simultaneous images generated by the beamsplitter are projected onto the EM-CCD. Each time the EM-CCD reads a frame, two simultaneous images with opposite polarization states are recorded. At the end of one FLC cycle, four images ($A_{\rm Left}$, $A_{\rm Right}$, $B_{\rm Left}$ and $B_{\rm Right}$) are produced.

As a visitor instrument, ExPo is placed at the Nasmyth platform of the WHT. ExPo does not have a de-rotator, so the sky rotation must be corrected during the data analysis.

5.2.2 Data Analysis

Each of the four images recorded after one FLC cycle is individually corrected for dark, flat, cosmic rays, instrumental polarization and sky rotation. The cleaned images are then aligned with a template image. The "right" images are then re-aligned with respect to to the "left" ones with a third of a pixel accuracy (see Canovas et al. 2011c, for a detailed description of the data reduction approach for ExPo).

Because of the short exposure times used by ExPo, it is possible to reduce the effect of seeing by about 30% by properly aligning each image (around 30% of the error in a wavefront is caused by the tip-tilt component, see Noll 1976). Polarized intensity ($P_I^{'}$) and intensity images are then calculated as

$$P_I^{'} = \frac{1}{2}\Big((A_{\rm Left} - A_{\rm Right}) - (B_{\rm Left} - B_{\rm Right})\Big), \tag{5.1}$$

$$I = \frac{1}{2}(A_{\rm Left} + A_{\rm Right} + B_{\rm Left} + B_{\rm Right}). \tag{5.2}$$

The "double-difference" image described by Eq. 5.1 has been discussed in detail by several authors (see for instance Kuhn et al. 2001, Hinkley et al. 2007, Perrin et al. 2008, Canovas et al. 2011c). Systematic errors and speckle noise (Racine et al. 1999, Sivaramakrishnan et al. 2002, Soummer et al. 2007) are minimized by this technique, allowing ExPo to increase its sensitivity and to reach high contrast ratios. To recover the Stokes parameters Q and U in the reference frame of the observed target, it is necessary to combine at least two different FLC positions (see, for example, Bagnulo et al. 2009b). Four different sets, taken at four different FLC orientations (0°, 22.5°, 45° and 67.5°) are recorded in each ExPo observation. Two calibrated, redundant datasets are calculated from these measurements. Residual errors such as uncorrected cosmic rays are easily removed by comparing these two redundant datasets. The calibration procedure for ExPo is discussed in detail by Rodenhuis et al. (2011b). The sky polarization is calculated separately for the Q and U images. In each image, the median of four different sky regions is first computed and then subtracted. The polarized intensity is then calculated as $P_I = \sqrt{Q^2 + U^2}$ and the polarization degree as $P = P_I/I$. There is a systematic error in the calibration process, which produces a rotation of the reference system by 9°. Because of this, the Stokes Q image is not aligned with the vertical direction (following the standard convention), but is tilted by 9°. The source of this error is not yet known. This error will affect the polarized angle, calculated as $P_\Theta = 0.5 \cdot \arctan(U/Q)$, but not the (scalar) P and P_I images.

5.2.3 Ghosts

Ghost images can be troublesome for our analysis, in particular if they are polarized. Due to the nature of ExPo, being a visitor instrument, and because of the different filters used during our observations, ghosts must be carefully identified during each campaign. The first dataset obtained during these observations was severely affected by a ghost, and therefore this dataset is not taken into account in our analysis. To remove the ghosts associated with our filters in the subsequent observations, the ExPo filter wheel was tilted by an appropriate angle. For comparison, two sets of images taken with the Sloan R filter, with and without ghosts, are shown in Fig. 5.1. Because of the filter ghost on the left image, the central star looks elongated towards the south-west direction. The left image shows no signs of ghosts, and the point spread function (PSF) is much sharper than its equivalent in the left image.

Target	Filter	No. Frames.	Exp. Time[sec]
BD+303639	Sloan R[1]	4×12282	0.028
"	Sloan R	4×8188	0.028
"	Sloan I	4×12282	0.028
"	H_α	4×12282	0.028
"	H_αCont	4×16376	0.028
"	Na	4×4095	0.1
"	Na Cont	4×4095	0.1
HD122815	-	4×1022	0.028

Table 5.1: Summary of ExPo observations. The dataset labelled as Sloan R[1] was affected by ghosts, as explained in §2.3

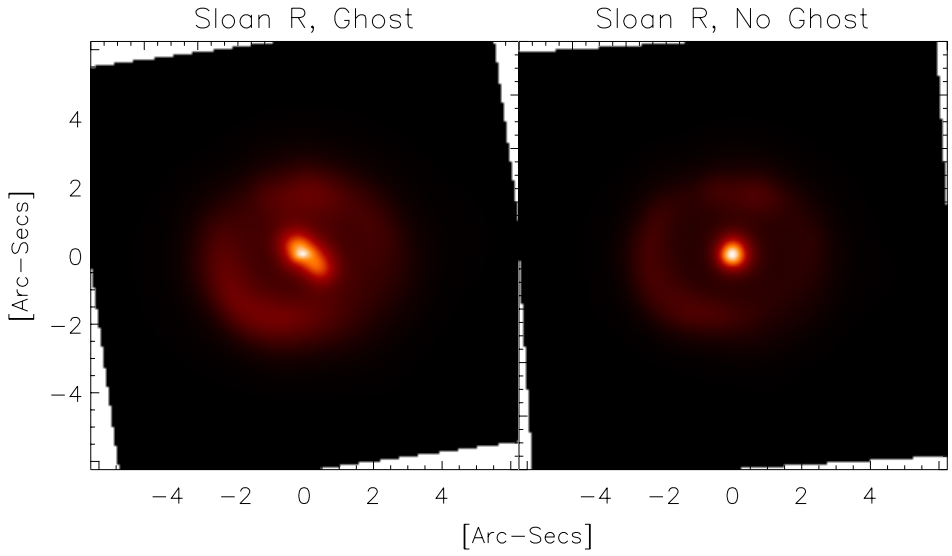

Figure 5.1: Left: Intensity image of BD+303639 taken with the Sloan R filter, severely affected by a ghost. Right: The same image after tilting the filter wheel. The ghost has disappeared. North is up and East is to the left in both images.

5.3 Results

For each filter, only the (calibrated) dataset with higher signal to noise (i.e., with better seeing conditions) is discussed here. For comparison, the unpolarized (diskless) star HD122815 is analyzed following the same data reduction approach as BD+303639.

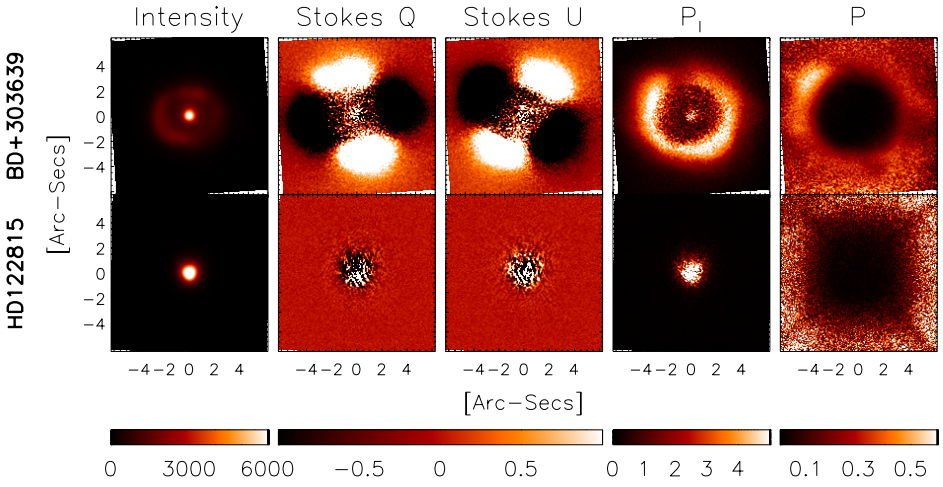

Figure 5.2: Top row: BD+303639, Sloan R filter. Bottom row: HD122815 (diskless, unpolarized), no filter. From left to right: total intensity (I), Stokes Q and U images, polarized intensity (P_I) and degree of polarization, P. As expected, HD122815 does not show any structure in the polarized images. The effect of the spiders of the telescope is clearly visible in the degree of polarization image. BD+303639 shows very strongly polarized features. North is up and East is to the left in all the images. Units of the color bars are given in arbitrary units.

The results of this analysis are shown in Fig. 5.2. The unpolarized star does not show any polarized structure at all. Some remnant (photon) noise can be seen at the center of the P_I image. On the other hand, BD+303639 shows at least three different structures than can be seen in the intensity and polarized images. The I image shows a bright (ionized) shell around the central star at a distance of 2.5". The dimmer regions of this shell are caused by dust extinction (this effect has been discussed at length by several authors, see for instance Harrington et al. 1997, Li et al. 2002, Lee & Kwok 2005). The Stokes Q and U images display the butterfly pattern associated with light scattered by circumstellar matter. These images show that the amount of polarized light is much larger outside of the ionized ring. This is also clearly shown in the P image. The degree of polarization, P, image shows a similar pattern. There is a faint ring with a larger degree of polarization, with a bright cloud on the North-East of this ring, and two dimmer regions around the West and South-West directions. This ring appears to extend even further out than the bright ring that appears in the polarized intensity image.

The Sloan R, H_α and H_α continuum images were obtained with the same instrument setup (i.e., gain and exposure time). The transmission and width of the H_α filter and the H_α continuum filter are the same. The corresponding I and P_I images

are shown in Fig. 5.3 (top and bottom row, respectively). To enhance the differences between these two images, we have normalized the I images to the maximum value of the H_α I image. We then repeat the same process with the P_I image. The ionized shell is brighter than the star in the H_α I image, while the opposite happens in the H_α continuum image. Furthermore, the difference in flux between the two images is considerable, with the star emitting 4.45 times more flux in the H_α than in the H_α continuum image. It may be that our images are contaminated by strong emission from other lines. We are currently analyzing this possibility, but this might explain this strong difference for the stellar flux in both filters. P_I shows a polarized ring at a distance of 3.6" from the central star in the H_α image, while the H_α continuum image shows a discrete amount of polarized light uniformly spread around the star. Moreover, the amount of polarized flux in the H_α continuum is also remarkably smaller when compared with its counterpart image at H_α. The polarized ring coincides in size and shape with the dusty halo that appears in the selective extinction $E_{\beta-\alpha}$ image calculated by Harrington et al. (1997).

The polarization degree (P) image for the H_α filter, shown in Fig. 5.4, indicates the presence of a faint ring surrounding the bright ring that is clearly visible in the P_I image, as happens with the Sloan R image (see the top-right image in Fig. 5.3). To better indicate these three different rings, different contours are plotted over the P image in Fig. 5.4. The contour of the ionized shell is shown by a blue line. The contours of the bright ring that appears in the P_I are shown by white lines. Finally, the brightest features of the faint ring that appear on the P image are indicated by yellow contour lines. The degree of polarization in the continuum filter does not show any structure at all, as expected from its faint polarized flux, which is why we do not show that image here.

Comparison between the Sloan R (top row of Fig. 5.2) and H_α (Fig. 5.3 and Fig. 5.4) shows that the images in both filters have the same features. In both filters a polarized ring around the ionized shell appears with a high signal-to-noise ratio (SNR), and a faint ring in the degree of polarization image is visible in the outermost regions of the nebula. The presence of a dust envelope that extends further out from the central star has already been reported by several authors (Latter et al. 1995, Harrington et al. 1997, Phillips & Ramos-Larios 2007).

5.4 Discussion

Several studies have reported the presence of silicates and polycyclic aromatic hydrocarbons (PAHs) on the nebular spectrum of BD+303639 (Waters et al. 1998a, Cohen et al. 2002, Matsumoto et al. 2008). PAHs are associated with carbon-rich chemistry, while silicates are associated with oxygen-rich dust (Waters et al. 1996, Waelkens et al. 1996). The nebula around BD+303639 is not older than 1000 years (Li et al. 2002), so the simultaneous presence of O-rich and C-rich features in its spectrum suggests a recent change in the chemistry of the central star. This dual chemistry is now known to be common in planetary nebulas with [WC]-type central stars (Waters et al. 1998a,b,

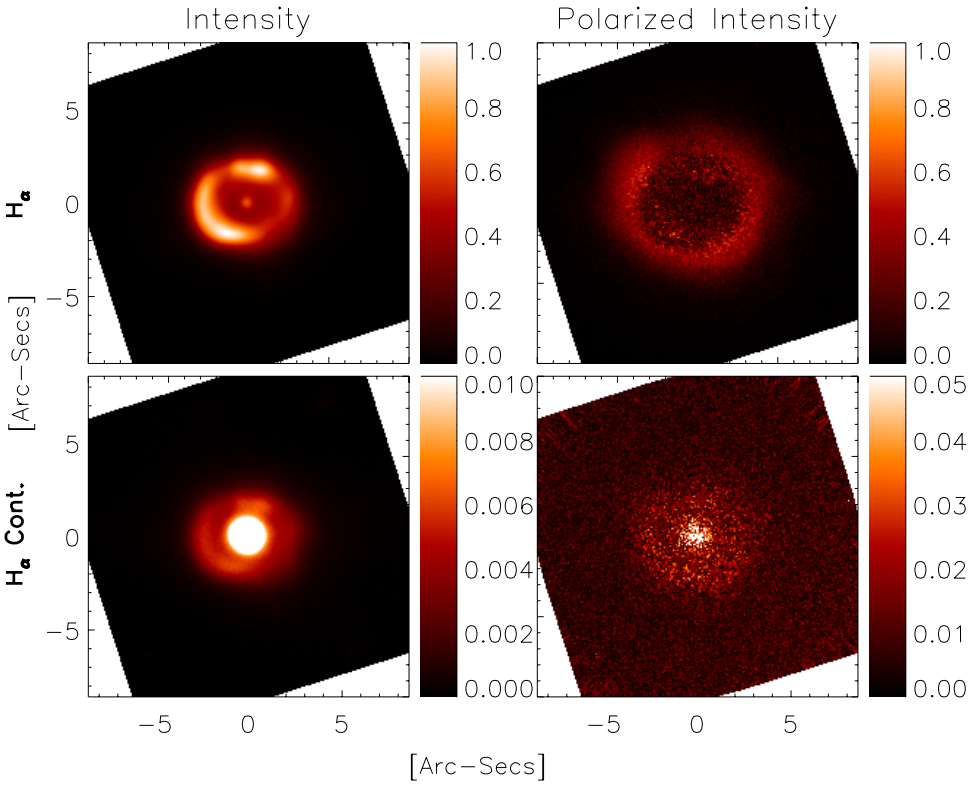

Figure 5.3: Top row: H_α filter. Bottom raw: H_αContinuum filter. The intensity images are normalized to the H_α intensity. The polarized intensity images are normalized to the H_α polarized intensity images. North is up, East is to the left in all images.

Cohen et al. 1999, 2002). To explain this phenomena, two main scenarios are proposed: a late thermal pulse that ejects the O-rich surface of the star, uncovering its C-rich nucleus (Schoenberner 1979, Iben et al. 1983, Willems & de Jong 1986, Herwig et al. 1999), or the existence of a circumbinary disk where the silicates are in orbit around the system (Lloyd Evans 1990, Barnbaum et al. 1991, Cohen et al. 1999, 2002). There is no evidence of a companion for the central star of BD+303639, so the first scenario (the late thermal pulse at the end of the AGB phase) is the most plausible one for this system. According to this hypothesis, the central star of BD+303639 first released its outermost (O-rich) layers no longer than 1000 years ago, and then it became a C-rich star. Because of this, the O-rich material (silicates) is expected to be in the outermost regions of the nebulae. The C-rich material that has been expelled since the onset of the late thermal pulse should be distributed in a shell closer to the central star. Matsumoto et al. (2008) finds evidences of a *thin* shell of silicates at a

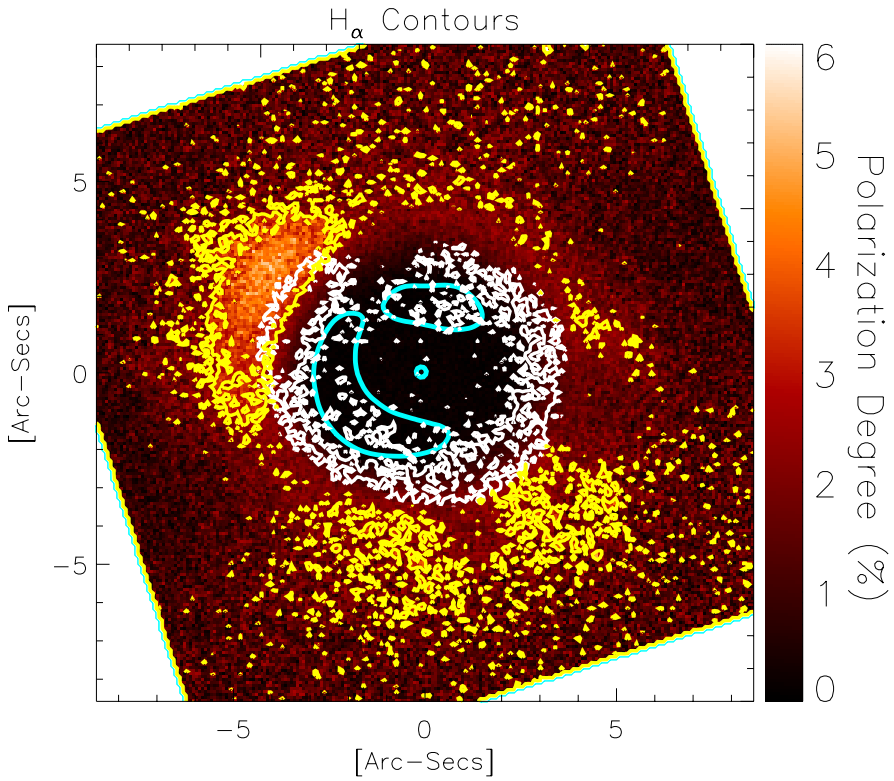

Figure 5.4: H_α filter image (degree of polarization) of BD+303639. Blue contour lines indicate the brightest regions of the I image (i.e., the ionized shell, see the top-left image in Fig/ 5.3). White contour lines indicate the regions with higher P_I (see the top-right image in Fig. 5.3). The yellow contour lines show the regions with a degree of polarization of 2.75%.

distance of 3″ from the central star, confirming this hypothesis. Here we compare our polarimetric observations with a model of BD+303639, in which an inner ring of Carbon-rich material is surrounded by an outer ring of Oxygen-rich dust. We generate a grid of models with different sizes of this outer ring, and then we compare these models with our measurements.

5.4.1 Model Setup

We have produced two models (Model 1 and Model 2) of BD+303639 to compare with our H_α and H_α continuum images. Model 1 simulates the polarized features produced by a star surrounded by a ring of ionized gas, and this model is compared with the H_α images. Model 2 does not include the ionized ring, and only contains a

central star as the source of light. This model is compared with the H_α continuum image. Both models include one ring of carbon-rich dust, and an outer ring of oxygen-rich dust. In both cases, we assume a continuous outflow with constant mass loss and constant escape velocity to model the density function. According to this, the density $\rho(r)$ scales with the distance to the star as $\rho(r) \propto r^{-2}$, where r is the distance to the star. Previous studies indicate that the geometry of BD+303639 is better described by an ellipsoidal shape (Bryce & Mellema 1999, Li et al. 2002, Lee & Kwok 2005) seen almost pole on (inclination angle of $i \sim 10°$). Because of this small inclination we consider the distribution of dust and gas to be axisymmetric around the central star. To study in detail the consequences of the elliptical shape of BD+303639 on the polarized features that we observe is beyond the scope of this paper.

To account for the properties of the central star (distance, temperature, luminosity and mass), we use the values derived by Crowther et al. (2006). Those parameters are based on the most recent distance calculations to BD+303639 measured by Li et al. (2002) (1.2 kpc). The ring made of ionized gas has an inner radius of 3000 astronomical units (AUs) and a width of 200 AUs. We adjust the brightness of this ring to fit our observations. To compute the dust distribution we make use of the radiative transfer code MCMax, described in Min et al. (2009b). The shape of the dust particles is modelled with the distribution of hollow spheres (DHS) discussed by Min et al. (2005b). For this computation, we use an "irregularity parameter" of $f_{max} = 0.8$. In both the C-rich and O-rich rings we use the classical MRN dust size distribution derived by (Mathis et al. 1977). This distribution follows the power law

$$n(a)\,\mathrm{d}a \propto a^{-3.5}\mathrm{d}a, \tag{5.3}$$

where a is the radius of the grains, ranging from 5 nm to 250 nm.

We then compute a grid of models with different outer radius (i.e., different masses) for the ring made of silicates. The flux in each model is then corrected for reddening. To do this, we adopt the value calculated by Bernard-Salas et al. (2003) of $E(B-V) = 0.34$. The intrinsic absorption inside BD+303639 is not taken into account in this correction (see, for instance Harrington et al. 1997, Lee & Kwok 2005). For the C-rich dust composition we assume amorphous carbon with the refractive index taken from Preibisch et al. (1993b). To model the O-rich dust we consider a mixture of different amorphous silicates with an average composition as derived for the interstellar medium by Min et al. (2007). The refractive index for these particles is taken from Dorschner et al. (1995b), Henning & Stognienko (1996b) and Mutschke et al. (1998). We consider the gas-to-dust ratio to be the same (100) in both shells. We then compute a total mass of $M = 1.4 \cdot 10^{-3}\mathrm{M}_\odot$ for the C-rich shell. Assuming an expansion velocity for both shells of 22 km/s (Mellema 2004), the mass loss rate during the C-rich period is $\dot{M} = 1.05 \cdot 10^{-5}\mathrm{M}_\odot\mathrm{yr}^{-1}$. This value is not well constrained by the current version of our model, and future calculations will be improved. The O-rich shell has different masses depending on the outer radius used in this computation, and therefore, different mass-loss rates can be derived. The parameters of these models are summarized in Table 5.2.

To compare our observations with these models, we combine the radiative-transfer calculations with a numerical simulation of ExPo, which takes into account the ExPo PSF, the instrumental polarization, the photon noise and the transmission of the telescope and instrument. To simulate the PSFs, we first generate a set of 100 statistically independent wavefronts, considering a seeing of 0.8''. These wavefronts are then combined with a simulation of the William Herschel Telescope aperture to compute a set of ExPo PSFs as described in Min et al. (submitted). The two models of BD+303639 generated before are then convolved with this set of PSFs. The flux in each simulated image is then corrected for transmission effects by taking into account the transmission coefficients of the atmosphere, telescope and instrument (these coefficients are shown in Rodenhuis et al., in preparation). The photon and readout noise are then calculated and added to each image. Finally, the flux is converted to counts by taking into account the exposure time and the CCD gain during the real observations. The final set of images is then reduced in the same way as the observations, using the ExPo pipeline discussed by Canovas et al. (2011c). The images generated at the end of this process are given in units of counts.

Parameter	Value
Distance (d)	1.2 [Kpc]
Stellar Temperature (T_{eff})	55,000 [K]
Stellar Luminosity ($L_\star$)	$6 \cdot 10^3$ [$L_\odot$]
Stellar Mass ($M_\star$)	0.6 [$M_\odot$]
reddening (E(B-V))	0.34
Ionized Gas inner radius (r_I^i)	3000 [AUs]
Ionized Gas outer radius (r_I^o)	3200 [AUs]
C-rich inner radius (r_C^i)	3200 [AUs]
C-rich outer radius (r_C^o)	3900 [AUs]
Mass in the C-rich ring (M_C)	$1.4 \cdot 10^{-3}$[$M_\odot$]
O-rich inner radius (r_O^i)	3900 [AUs]
O-rich outer radius (r_O^o)	[4.1,5,6.5,8,10,100]$\cdot 10^3$ [AUs]

Table 5.2: Main parameters used in the models. Distance, T_{eff}, $L_\star$ and $M_\star$ are taken from Crowther et al. (2006). The reddening E(B-V) is taken from Bernard-Salas et al. (2003).

5.4.2 Comparison with observations

We compare Model 1, calculated with different outer radius for the O-rich ring, with the H_α observations in Fig. 5.5. The comparison between Model 2 and the H_α continuum image is shown in Fig. 5.6. From both figures we see that our model produces a similar amount of counts (flux) as our observations. In Fig. 5.5 we see that the model that better fits our observations is the one indicated by the dark-blue curve, which corresponds to an outer radius of 6500 AUs for the O-rich ring. We also see that the model with the outer radius larger than r_O^o = 10000 AUs (black dashed

line) produces very similar results to the model with r_O^o = 100000 AUs (light-blue dashed line). The "dark-blue" model (r_O^o = 6500 AUs) contains a mass of dust of $2.1 \cdot 10^{-4} M_\odot$, which, assuming a gas-to-dust ratio of 100, implies a total mass of $M_O = 2.1 \cdot 10^{-2} M_\odot$. Taking into account an expansion velocity of 22 km/s, we derive a mass loss rate during the O-rich period of $\dot{M} = 3.9 \cdot 10^{-5} M_\odot \mathrm{yr}^{-1}$.

A comparison of the intensity, Stokes Q and U, polarized intensity and degree of polarization images produced by Model 1 with r_O^o = 6500 AUs and the H_α filter images is shown in Fig. 5.7. All images are smoothed with a 5-pixel gaussian kernel to reduce the noise. In this figure, we have rotated the observed images by 9° to correct the systematic error mentioned in §2.2. After this rotation, the Stokes Q and U images are aligned according to the standard system, with Q positive in the vertical direction, and U positive in the diagonal (bottom left to top right) direction. The simulated images are plotted at the same scale as the observed ones. The third column shows the observed image, and the contours for the observed images (in green color) and the simulations (yellow color). The contour levels are the same for both the observed and the simulated images. The intensity, Stokes Q and U, and the polarized intensity images show an almost perfect match with the real observations. The degree of polarization in the simulated image is slightly too high, producing a ring that is brighter than what we observe. An incorrect sky background correction may be the cause of this difference; this is currently being investigated. However, the position and width of this ring matches the observations well, as can be seen from the contours in the third column.

The same comparison, but now between Model 2 and the H_α continuum image is shown in Fig. 5.6. We see that our model needs to be improved to better match the polarized features on this filter. Still, we can reproduce the butterfly pattern that appears in the Stokes Q and U images, and the simulated I and P_I images are very similar to the observed data. However, we also see that we need to improve the model to account for the (small) amount of polarized flux that appears around the central star in the real observations in the Stokes Q, U and P_I images. As mentioned in §3, it may be that our measurements are contaminated by emission from other spectral lines. This could explain the slightly worse fit that we obtain for this images as compared to the good fit that we obtain for the H_α filter. We are currently investigating this possibility.

The model calculated by Waters et al. (1998a) produces an estimate of r_O^o = 29411 AUs, and a mass for the O-rich shell of $M \sim 0.37 M_\odot$. However, his model uses different parameters than ours (distance and temperature of the central star). Even more important is the difference in width that we derive for the O-rich shell when we compare our results with the results obtained by Matsumoto et al. (2008). According to that work, the O-rich dust is located in a very thin shell, with an inner radius of 3600 AUs and a width no wider than 216 AUs. Based on this value, they derive a very high mass loss rate during a very short period of 100 years during the O-rich stage of the central star. We find that this value is incompatible with our model, since the model with the smaller outer radius (red dashed line in Figures 5.5 and 5.6, r_O^o = 4100 AUs) cannot produce enough polarized flux to explain our observations.

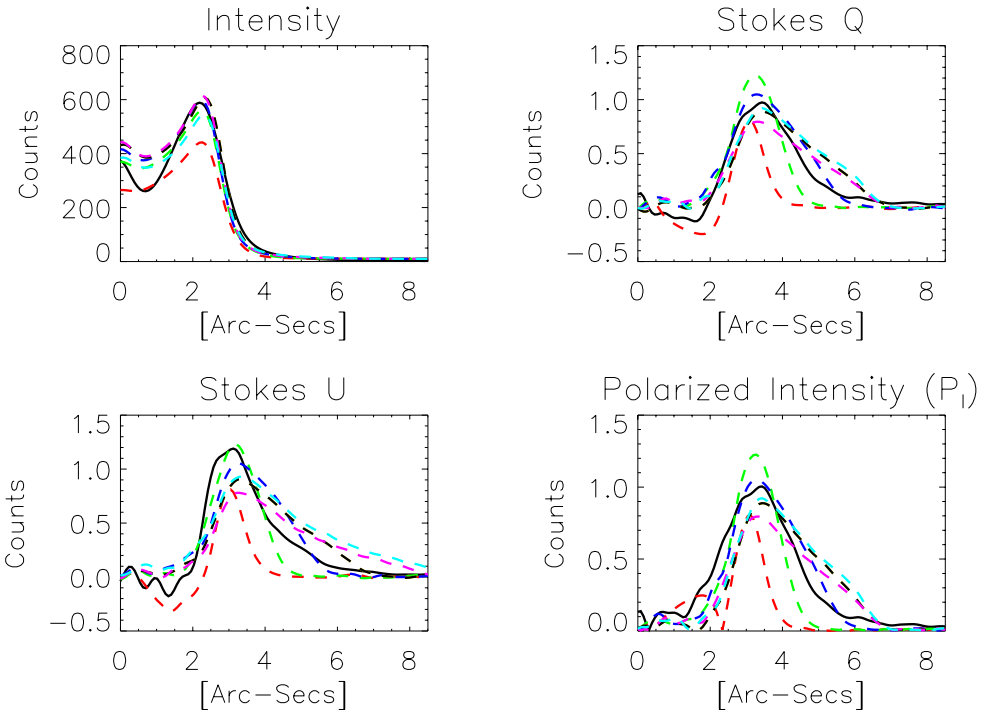

Figure 5.5: Comparison of the H_α filter images of BD+303639 with different models. All plots show a horizontal cut, except for the Stokes *U* plot, which is a diagonal plot (to enhance the bright features of the Stokes *U* image). The thick line shows the cut for the real (observed) images, the dashed line represents the models. The different colors indicate the outer radius of the O-rich ring (r_O^o) with red = 4100 AUs, green = 5000 AUs, Dark Blue = 6500 AUs, Black = 8000 AUs, Purple = 10000 AUs and light-blue = 100000 AUs.

5.5 Conclusions

Our polarized images show a very extended, neutral shell around the central star of BD+303639. This neutral halo has previously been detected at different wavelengths (see for instance, Dinerstein & Sneden 1988, Harrington et al. 1997, Phillips & Ramos-Larios 2007). However, the work presented here is the first polarimetric study of this system. Imaging polarimetry allow us to constrain the properties of the dust (size, composition) in the neutral halo. Our H_α and H_α continuum images allow us to construct a realistic model of BD+303639 that includes an outer ring of O-rich material (silicates), and an inner ring of C-rich dust. The size of the silicate ring that best fits our observations is much bigger than the size predicted by Matsumoto et al. (2008). One of the sources of this difference might be weak flux of the neutral halo, making it difficult to measure the spectra in the outermost regions of the nebula.

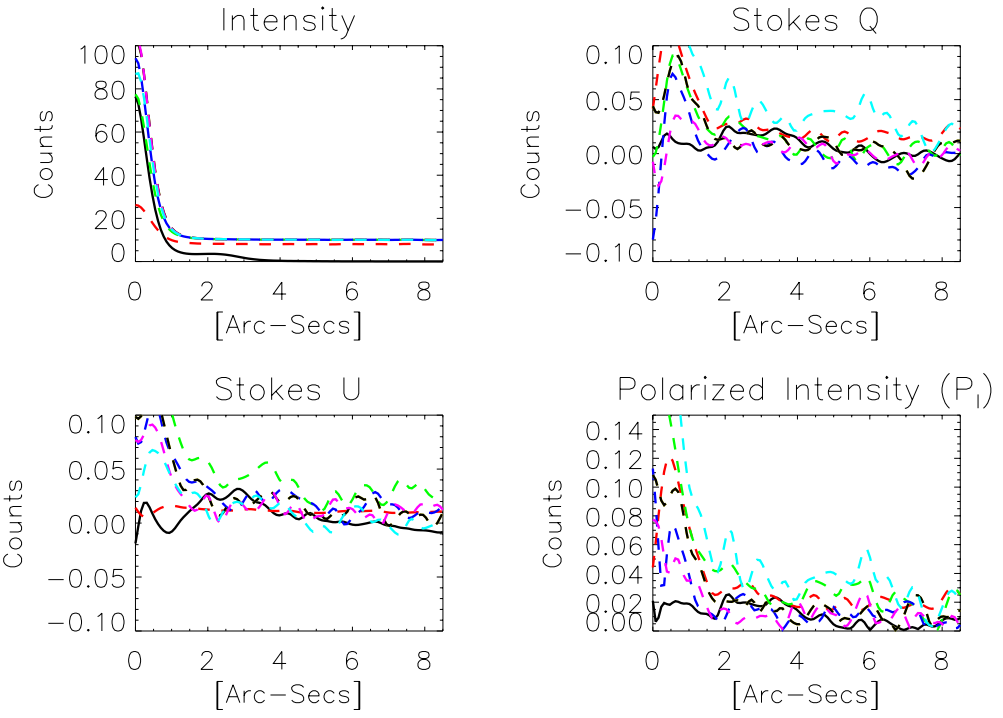

Figure 5.6: Same as in Fig. 5.5, but now for the H_α continuum image, and the corresponding models.

The possibility of contamination from other lines in our images does not change our calculations for the O-rich and C-ring shells; the P_I and P images clearly show a polarized, extended halo. Considering the latest value for the distance to BD+303639, the mass loss rates derived by Waters et al. (1998a) produce approximately the same values as what we obtain from our models. Still, further modeling and a more detailed analysis (currently ongoing) is needed to properly characterize the neutral halo of this interesting object.

Imaging polarimetry proves to be a useful tool to detect and characterize circumstellar environments around young and evolved stars (see for instance: Gledhill & Takami 2001, Ramstedt et al. 2011, Perrin et al. 2009b, Hinkley et al. 2009). This still young, promising technique will lead to a better understanding of the faint circumstellar environments that are difficult to characterize with other techniques. With the advent of new polarimeters such as SPHERE at the VLT, GPI at Gemini and Hi-Ciao at the Subaru telescope, even better polarimetric observations of circumstellar environments will be secured.

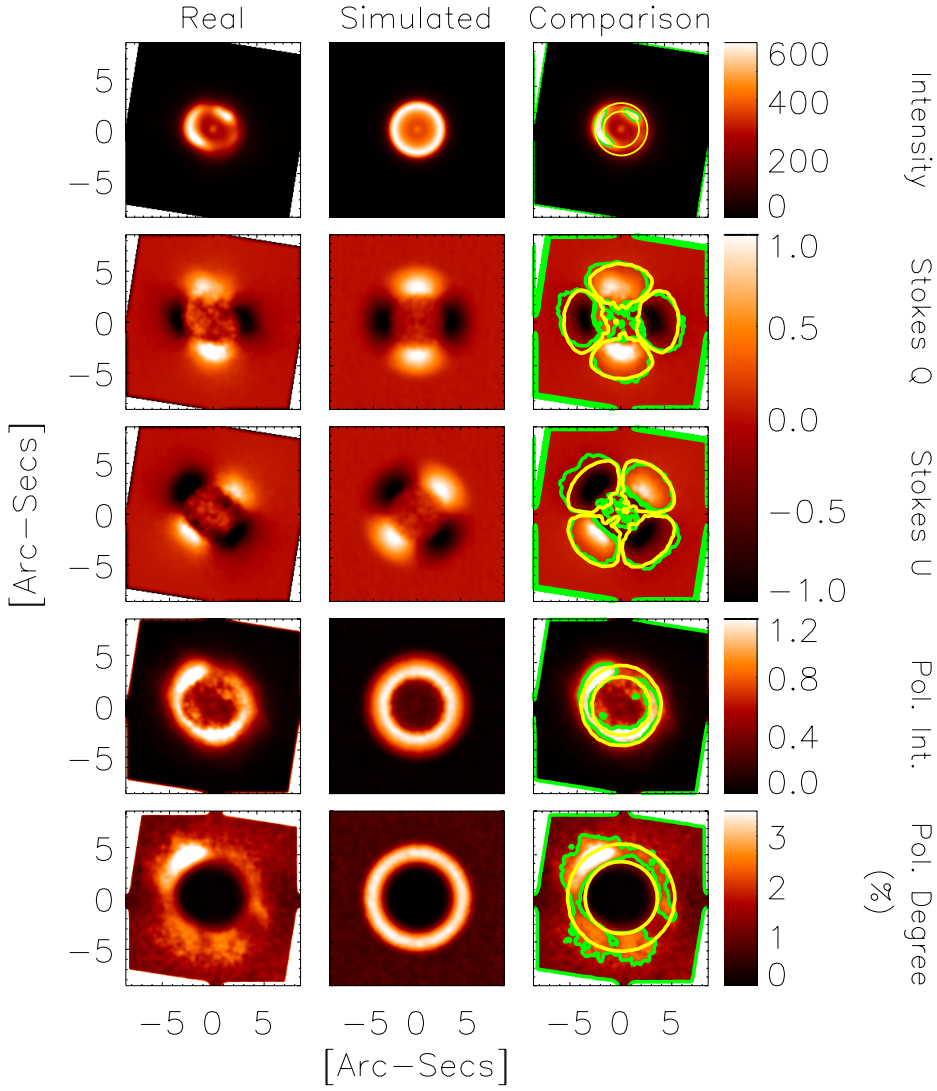

Figure 5.7: Comparison of the H_α observations (left column) with Model 1, assuming an outer ring of silicates r_O^o = 6500 AUs (center column). The right column shows the real observations, with different contour levels for the model (blue contour) and observations (green contours). All images are smoothed with a gaussian kernel of 5 pixels. From top to bottom, the first row shows the intensity I image and the second and third rows show the Stokes Q and U images, respectively. The fourth row shows the polarized intensity (P_I) image, and the bottom row shows the degree of polarization P.

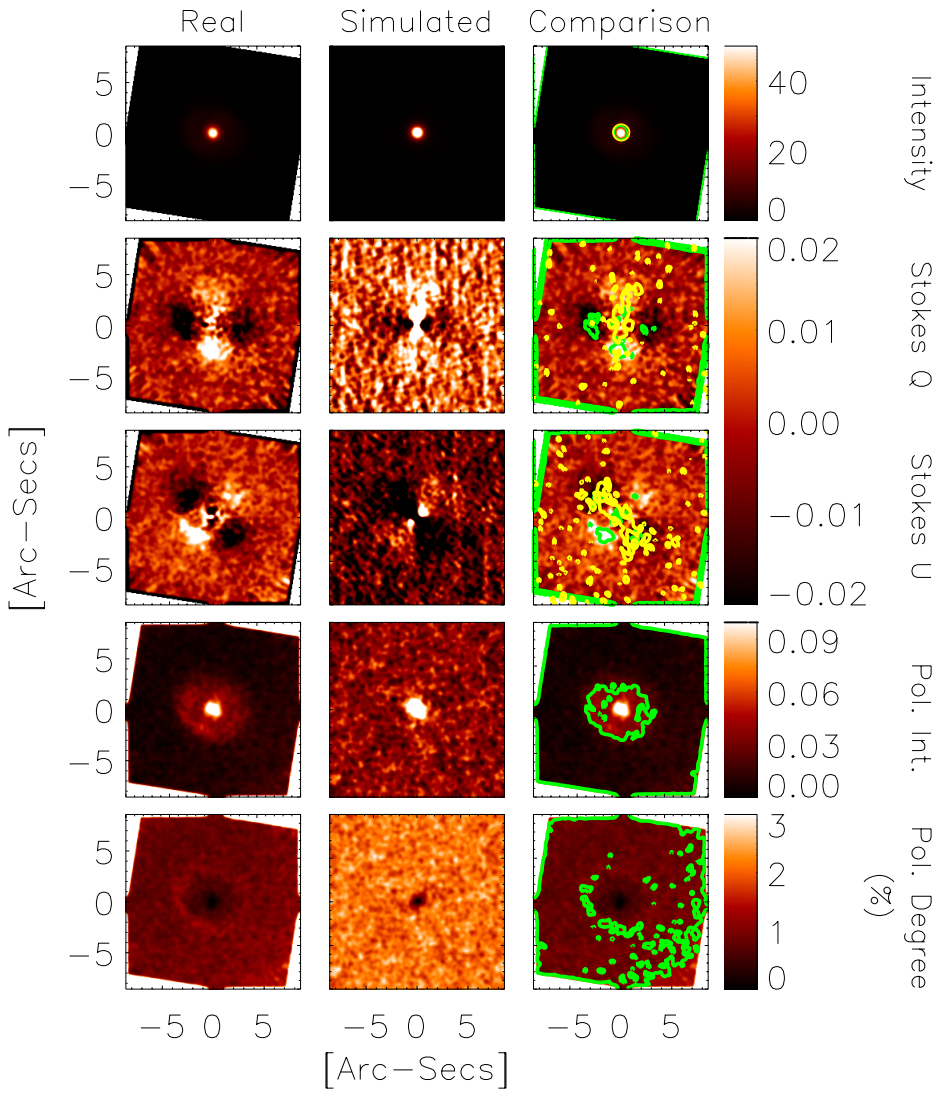

Figure 5.8: Same as Fig. 5.7, but for the H_α continuum filter and the corresponding simulation (Model 2, r_O^o = 6500 AUs).

Acknowledgments

We are grateful to the staff at the William Herschel Telescope for their help during the during the observations.

Bibliography

A. C. Raga, E. M. de Gouveia Dal Pino, A. Noriega-Crespo, P. D. Mininni, & P. F. Velázquez. 2002, A&A, 392, 267 (cited on page 81)

Acker, A., Marcout, J., Ochsenbein, F., Stenholm, B., & Tylenda, R. 1992, Strasbourg - ESO catalogue of galactic planetary nebulae. Part 1; Part 2, ed. Acker, A., Marcout, J., Ochsenbein, F., Stenholm, B., & Tylenda, R. (cited on page 88)

Alonso-Albi, T., Fuente, A., Bachiller, R., et al. 2009, Astron. Astrophys., 497, 117 (cited on pages 68 and 69)

Andrews, S. M., Wilner, D. J., Espaillat, C., et al. 2011, Astrophys. J., 732, 42 (cited on page 54)

Armitage, P. J. 2011, Annual Review of Astronomy and Astrophysics, 49, null (cited on page 6)

Bachiller, R., Huggins, P. J., Cox, P., & Forveille, T. 1991, Astron. Astrophys., 247, 525 (cited on page 89)

Bachiller, R., Huggins, P. J., Martin-Pintado, J., & Cox, P. 1992, Astron. Astrophys., 256, 231 (cited on page 89)

Bagnulo, S., Landolfi, M., Landstreet, J. D., et al. 2009a, Publ. Astron. Soc. Pac., 121, 993 (cited on page 26)

Bagnulo, S., Landolfi, M., Landstreet, J. D., et al. 2009b, Publ. Astron. Soc. Pac., 121, 993 (cited on page 91)

Bailey, J., Ulanowski, Z., Lucas, P. W., et al. 2008, MNRAS, 386, 1016 (cited on page 34)

Barnbaum, C., Kastner, J. H., Morris, M., & Likkel, L. 1991, Astron. Astrophys., 251, 79 (cited on page 95)

Barth, W., Weigelt, G., & Zinnecker, H. 1994, Astron. Astrophys., 291, 500 (cited on page 68)

Beckwith, S., Gatley, I., & Persson, S. E. 1978, Astrophys. J. Lett., 219, L33 (cited on page 89)

Begemann, B., Dorschner, J., Henning, T., Mutschke, H., & Thamm, E. 1994, Astrophys. J. Lett., 423, L71 (cited on page 43)

Bell, K. R., Lin, D. N. C., Hartmann, L. W., & Kenyon, S. J. 1995, Astrophys. J., 444, 376 (cited on page 6)

Benisty, M., Malbet, F., Dougados, C., et al. 2010, A&A, 517, L3 (cited on pages 69 and 83)

Bernard-Salas, J., Pottasch, S. R., Wesselius, P. R., & Feibelman, W. A. 2003, Astron. Astrophys., 406, 165 (cited on pages 89, 97, and 98)

Beuzit, J.-L., Feldt, M., Mouillet, D., et al. 2010, in In the Spirit of Lyot 2010 (cited on page 12)

Bonnefoy, M., Lagrange, A.-M., Boccaletti, A., et al. 2011, Astron. Astrophys., 528, L15+ (cited on page 5)

Bouwman, J., de Koter, A., Dominik, C., & Waters, L. B. F. M. 2003, Astron. Astrophys., 401, 577 (cited on page 54)

Brown, J. M., Blake, G. A., Dullemond, C. P., et al. 2007, Astrophys. J. Lett., 664, L107 (cited on page 54)

Bryce, M. & Mellema, G. 1999, MNRAS, 309, 731 (cited on page 97)

Burrows, A. 2005, Nature, 433, 261 (cited on page 3)

Burrows, A., Sudarsky, D., & Hubeny, I. 2004, Astrophys. J., 609, 407 (cited on page 3)

Canovas, H., Rodenhuis, M., Jeffers, S. V.and Min, M., & Keller, C. U. 2011a, In preparation (cited on page 18)

Canovas, H., Rodenhuis, M., Jeffers, S. V.and Min, M., & Keller, C. U. 2011b, In preparation (cited on page 18)

Canovas, H., Rodenhuis, M., Jeffers, S. V., Min, M., & Keller, C. U. 2011c, Astron. Astrophys., 531, A102+ (cited on pages 49, 53, 71, 72, 79, 88, 90, 91, and 98)

Chauvin, G., Lagrange, A.-M., Zuckerman, B., et al. 2005, Astron. Astrophys., 438, L29 (cited on page 4)

Christou, J. C. 1991, Publ. Astron. Soc. Pac., 103, 1040 (cited on page 35)

Christou, J. C., Zinnecker, H., Haas, M., Leinert, C., & Ridgway, S. T. 1992, in European Southern Observatory Conference and Workshop Proceedings, Vol. 39, European Southern Observatory Conference and Workshop Proceedings, ed. J. M. Beckers & F. Merkle, 83–+ (cited on page 68)

Clariá, J. J. 1974, Astron. Astrophys., 37, 229 (cited on page 68)

Close, L. M., Roddier, F., Hora, J. L., et al. 1997, Astrophys. J., 489, 210 (cited on page 42)

Cohen, M., Barlow, M. J., Liu, X.-W., & Jones, A. F. 2002, MNRAS, 332, 879 (cited on pages 94 and 95)

Cohen, M., Barlow, M. J., Sylvester, R. J., et al. 1999, Astrophys. J. Lett., 513, L135 (cited on pages 89 and 95)

Crowther, P. A. 2008, in Astronomical Society of the Pacific Conference Series, Vol. 391, Hydrogen-Deficient Stars, ed. A. Werner & T. Rauch, 83–+ (cited on page 88)

Crowther, P. A., Morris, P. W., & Smith, J. D. 2006, Astrophys. J., 636, 1033 (cited on pages 88, 89, 97, and 98)

de Gouveia Dal Pino, E. M. 1999, Astrophys. J., 526, 862 (cited on page 81)

Dinerstein, H. L. 1991, Publ. Astron. Soc. Pac., 103, 861 (cited on page 88)

Dinerstein, H. L. & Sneden, C. 1988, Astrophys. J. Lett., 335, L23 (cited on pages 89 and 100)

Dominik, C. 2009, in Astronomical Society of the Pacific Conference Series, Vol. 414, Cosmic Dust - Near and Far, ed. T. Henning, E. Grün, & J. Steinacker, 494–+ (cited on page 42)

Dominik, C. & Dullemond, C. P. 2008, Astron. Astrophys., 491, 663 (cited on pages 78 and 79)

Donati, J., Semel, M., Carter, B. D., Rees, D. E., & Collier Cameron, A. 1997, MNRAS, 291, 658 (cited on page 27)

Dorschner, J., Begemann, B., Henning, T., Jäger, C., & Mutschke, H. 1995a, Astron. Astrophys., 300, 503 (cited on page 43)

Dorschner, J., Begemann, B., Henning, T., Jaeger, C., & Mutschke, H. 1995b, Astron. Astrophys., 300, 503 (cited on page 97)

Dubrulle, B., Morfill, G., & Sterzik, M. 1995, Icarus, 114, 237 (cited on page 46)

Dullemond, C. & Monnier, J. 2010, Annual Review of Astronomy and Astrophysics, 48, 205 (cited on page 6)

Dullemond, C. P., Apai, D., & Walch, S. 2006, Astrophys. J. Lett., 640, L67 (cited on page 47)

Dullemond, C. P. & Dominik, C. 2004a, Astron. Astrophys., 417, 159 (cited on page 6)

Dullemond, C. P. & Dominik, C. 2004b, Astron. Astrophys., 421, 1075 (cited on pages 42 and 46)

Dullemond, C. P., Hollenbach, D., Kamp, I., & D'Alessio, P. 2007a, Protostars and Planets V, 555 (cited on page 6)

Dullemond, C. P., Hollenbach, D., Kamp, I., & D'Alessio, P. 2007b, in Protostars and Planets V, ed. B. Reipurth, D. Jewitt, & K. Keil, 555–572 (cited on page 42)

Espaillat, C., Calvet, N., Luhman, K. L., Muzerolle, J., & D'Alessio, P. 2008, Astrophys. J. Lett., 682, L125 (cited on page 54)

Fischer, O., Stecklum, B., & Leinert, C. 1998, Astron. Astrophys., 334, 969 (cited on page 68)

Fried, D. L. 1966, Journal of the Optical Society of America (1917-1983), 56, 410 (cited on page 58)

Fruchter, A. S. & Hook, R. N. 2002, Publications of the Astronomical Society of the Pacific, 114, pp. 144 (cited on page 25)

Fukugita, M., Ichikawa, T., Gunn, J. E., et al. 1996, Astron. J., 111, 1748 (cited on page 90)

Garcia, P. J. V., Thiébaut, E., & Bacon, R. 1999, Astron. Astrophys., 346, 892 (cited on page 69)

García-Lorenzo, B., Eff-Darwich, A., Fuensalida, J. J., & Castro-Almazán, J. 2009, MNRAS, 397, 1633 (cited on page 59)

Geiss, J. 1987, Astron. Astrophys., 187, 859 (cited on page 43)

Gillett, F. C. 1986, in Astrophysics and Space Science Library, Vol. 124, Light on Dark Matter, ed. F. P. Israel, 61–69 (cited on page 5)

Gledhill, T. & Takami, M. 2001, Monthly Notices of the Royal Astronomical Society, 328, 266 (cited on page 101)

Gledhill, T. M., Chrysostomou, A., Hough, J. H., & Yates, J. A. 2001, MNRAS, 322, 321 (cited on page 42)

Graham, J. R., Macintosh, B., Doyon, R., et al. 2007, in Bulletin of the American Astronomical Society, Vol. 38, Bulletin of the American Astronomical Society, 968–+ (cited on pages 12 and 18)

Grevesse, N. & Sauval, A. J. 1998a, Space Sci. Rev., 85, 161 (cited on page 43)

Grevesse, N. & Sauval, A. J. 1998b, Space Sci. Rev., 85, 161 (cited on page 79)

Hajian, A. R. & Terzian, Y. 1994, in Bulletin of the American Astronomical Society, Vol. 26, American Astronomical Society Meeting Abstracts, 1469–+ (cited on page 88)

Harrington, J. P., Lame, N. J., White, S. M., & Borkowski, K. J. 1997, Astron. J., 113, 2147 (cited on pages 89, 93, 94, 97, and 100)

Hartmann, L. & Calvet, N. 1995, Astron. J., 109, 1846 (cited on page 6)

Hartmann, L. & Kenyon, S. J. 1996a, Annu. Rev. Astron. Astrophys., 34, 207 (cited on page 6)

Hartmann, L. & Kenyon, S. J. 1996b, Annu. Rev. Astron. Astrophys., 34, 207 (cited on page 68)

Hartmann, L., Kenyon, S. J., Hewett, R., et al. 1989, Astrophys. J., 338, 1001 (cited on page 68)

Harvey, P. M., Wilking, B. A., & Joy, M. 1984, Nature, 307, 441 (cited on page 5)

Hashimoto, J., Tamura, M., Muto, T., et al. 2011, Astrophys. J. Lett., 729, L17+ (cited on page 42)

Henning, T. & Stognienko, R. 1996a, Astron. Astrophys., 311, 291 (cited on page 43)

Henning, T. & Stognienko, R. 1996b, Astron. Astrophys., 311, 291 (cited on page 97)

Herbst, W., Racine, R., & Warner, J. W. 1978, Astrophys. J., 223, 471 (cited on page 68)

Herwig, F., Blöcker, T., Langer, N., & Driebe, T. 1999, Astron. Astrophys., 349, L5 (cited on pages 89 and 95)

Hiltner, W. A. 1949, Science, 109, p. 165 (cited on page 31)

Hinkley, S., Oppenheimer, B. R., Soummer, R., et al. 2009, Astrophys. J., 701, 804 (cited on pages 9, 69, 72, and 101)

Hinkley, S., Oppenheimer, B. R., Soummer, R., et al. 2007, Astrophys. J., 654, 633 (cited on pages 4 and 91)

Hoare, M. G., Roche, P. F., & Clegg, R. E. S. 1992, MNRAS, 258, 257 (cited on page 89)

Hook, I. 2009, in Science with the VLT in the ELT Era, ed. A. Moorwood, Astrophysics and Space Science Proceedings (Springer Netherlands), 225–232 (cited on page 18)

Huggins, P. J., Bachiller, R., Cox, P., & Forveille, T. 1996, Astron. Astrophys., 315, 284 (cited on page 88)

Hughes, A. M., Wilner, D. J., Qi, C., & Hogerheijde, M. R. 2008, Astrophys. J., 678, 1119 (cited on page 46)

Iben, Jr., I., Kaler, J. B., Truran, J. W., & Renzini, A. 1983, Astrophys. J., 264, 605 (cited on page 95)

Ibragimov, M. A. & Shevchenko, V. S. 1990, in A. K. Mamatkazina, ed. C. on Classical Be Stars & A. H. Stars, Alma Alta (cited on page 68)

Joos, F. 2007, PhD thesis, Eidgenoessische Technische Hochschule Zuerich (Switzerland) (cited on page 32)

Kalas, P., Graham, J. R., Chiang, E., et al. 2008, Science, 322, 1345 (cited on pages 5, 7, and 18)

Kalas, P., Graham, J. R., & Clampin, M. 2005, Nature, 435, 1067 (cited on page 5)

Kaltcheva, N. T. & Hilditch, R. W. 2000, MNRAS, 312, 753 (cited on page 68)

Kama, M., Min, M., & Dominik, C. 2009, Astron. Astrophys., 506, 1199 (cited on pages 45 and 47)

Kastner, J. H., Li, J., Vrtilek, S. D., et al. 2002, Astrophys. J., 581, 1225 (cited on page 89)

Kastner, J. H., Soker, N., Vrtilek, S. D., & Dgani, R. 2000, Astrophys. J. Lett., 545, L57 (cited on pages 88 and 89)

Kawamura, J. & Masson, C. 1996, Astrophys. J., 461, 282 (cited on page 88)

Keller, C. U. 1996, Sol. Phys., 164, 243 (cited on pages 4 and 27)

Keller, C. U. 2002, Instrumentation for Astrophysical Spectropolarimetry (cited on page 19)

Keller, C. U. & von der Luehe, O. 1992, Astron. Astrophys., 261, 321 (cited on page 4)

Kenworthy, M. A., Codona, J. L., Hinz, P. M., et al. 2007, Astrophys. J., 660, 762 (cited on page 4)

Kolmogorov, A. 1941, Akademiia Nauk SSSR Doklady, 30, 301 (cited on page 58)

Koresko, C. D., Beckwith, S. V. W., Ghez, A. M., Matthews, K., & Neugebauer, G. 1991, Astron. J., 102, 2073 (cited on page 68)

Kreysing, H. C., Diesch, C., Zweigle, J., et al. 1992, Astron. Astrophys., 264, 623 (cited on pages 88 and 89)

Kuhn, J. R., Potter, D., & Parise, B. 2001, Astrophys. J. Lett., 553, L189 (cited on pages 18, 69, and 91)

Lafrenière, D., Marois, C., Doyon, R., Nadeau, D., & Artigau, É. 2007, Astrophys. J., 660, 770 (cited on page 4)

Lagrange, A.-M., Bonnefoy, M., Chauvin, G., et al. 2010, Science, 329, 57 (cited on page 5)

Lagrange, A.-M., Bonnefoy, M., Chauvin, G., et al. 2010, Science, 329, 57 (cited on page 18)

Latter, W. B., Kelly, D. M., Hora, J. L., & Deutsch, L. K. 1995, Astrophys. J. Suppl., 100, 159 (cited on page 94)

Law, N. M. 2006, PhD thesis, Cambridge University (cited on pages 35 and 59)

Law, N. M., Mackay, C. D., & Baldwin, J. E. 2006, Astron. Astrophys., 446, 739 (cited on page 25)

Lee, T.-H. & Kwok, S. 2005, Astrophys. J., 632, 340 (cited on pages 93 and 97)

Leuenhagen, U., Hamann, W.-R., & Jeffery, C. S. 1996, Astron. Astrophys., 312, 167 (cited on page 89)

Li, J., Harrington, J. P., & Borkowski, K. J. 2002, Astron. J., 123, 2676 (cited on pages 88, 89, 93, 94, and 97)

Lloyd Evans, T. 1990, MNRAS, 243, 336 (cited on page 95)

Malbet, F., Rigaut, F., Bertout, C., & Lena, P. 1993, Astron. Astrophys., 271, L9+ (cited on page 68)

Marois, C., Lafrenière, D., Doyon, R., Macintosh, B., & Nadeau, D. 2006, Astrophys. J., 641, 556 (cited on page 32)

Marois, C., Macintosh, B., Barman, T., et al. 2008a, Science, 322, 1348 (cited on page 4)

Marois, C., Macintosh, B., Barman, T., et al. 2008b, Science, 322, 1348 (cited on page 18)

Martin, Martin, S. R., & Booth, A. J. 2010, Astronomy and Astrophysics, 511, 4 pages (cited on page 4)

Martinez, P., Carpentier, E. A., & Kasper, M. 2010, Publ. Astron. Soc. Pac., 122, 916 (cited on page 18)

Masiero, J., Hodapp, K., Harrington, D., & Lin, H. 2008, ArXiv e-prints (cited on page 36)

Mathis, J. S., Rumpl, W., & Nordsieck, K. H. 1977, Astrophys. J., 217, 425 (cited on pages 79 and 97)

Matsumoto, H., Sakon, I., Onaka, T., et al. 2008, Astrophys. J., 677, 1120 (cited on pages 89, 94, 95, 99, and 100)

Meeus, G., Waters, L. B. F. M., Bouwman, J., et al. 2001a, Astron. Astrophys., 365, 476 (cited on page 6)

Meeus, G., Waters, L. B. F. M., Bouwman, J., et al. 2001b, Astron. Astrophys., 365, 476 (cited on page 46)

Mellema, G. 2004, Astron. Astrophys., 416, 623 (cited on pages 89 and 97)

Merín, B., Brown, J. M., Oliveira, I., et al. 2010, Astrophys. J., 718, 1200 (cited on page 54)

Mesa, D., Gratton, R., Berton, A., et al. 2011, Astron. Astrophys., 529, A131+ (cited on page 12)

Millan-Gabet, R. & Monnier, J. D. 2002, The Astrophysical Journal Letters, 580, L167 (cited on page 69)

Miller, R. H. 1963, Appl. Opt., 2, 61 (cited on page 31)

Min, M., Canovas, H., Keller, C. U., Jeffers, S. V., & Rodenhuis, M. 2011a, In preparation (cited on pages 32 and 36)

Min, M., Dullemond, C. P., Dominik, C., de Koter, A., & Hovenier, J. W. 2009a, Astron. Astrophys., 497, 155 (cited on page 47)

Min, M., Dullemond, C. P., Dominik, C., de Koter, A., & Hovenier, J. W. 2009b, Astron. Astrophys., 497, 155 (cited on pages 78 and 97)

Min, M., Dullemond, C. P., Kama, M., & Dominik, C. 2011b, Icarus, 212, 416 (cited on page 43)

Min, M., Dullemond, C. P., Kama, M., & Dominik, C. 2011c, Icarus, 212, 416 (cited on page 79)

Min, M. & Flynn, G. F. 2010, Dust Composition in Protoplanetary Disks, ed. Apai, D. A. & Lauretta, D. S., 161–190 (cited on page 43)

Min, M., Hovenier, J. W., & de Koter, A. 2005a, Astron. Astrophys., 432, 909 (cited on page 44)

Min, M., Hovenier, J. W., & de Koter, A. 2005b, Astron. Astrophys., 432, 909 (cited on pages 79 and 97)

Min, M., Hovenier, J. W., Waters, L. B. F. M., & de Koter, A. 2008, Astron. Astrophys., 489, 135 (cited on pages 44 and 45)

Min, M., Waters, L. B. F. M., de Koter, A., et al. 2007, Astron. Astrophys., 462, 667 (cited on page 97)

Murakawa, K. 2010, Astron. Astrophys., 518, A63+ (cited on pages 51 and 58)

Mutschke, H., Begemann, B., Dorschner, J., et al. 1998, Astron. Astrophys., 333, 188 (cited on page 97)

Nagaraju, K., Sankarasubramanian, K., Rangarajan, K. E., et al. 2008, Bulletin of the Astronomical Society of India, 36, 99 (cited on page 37)

Nightingale, N. S. & Buscher, D. F. 1991, MNRAS, 251, 155 (cited on page 59)

Noll, R. J. 1976, J. Opt. Soc. Am., 66, 207 (cited on pages 59 and 91)

Oppenheimer, B. R., Brenner, D., Hinkley, S., et al. 2008, Astrophys. J., 679, 1574 (cited on pages 7 and 69)

Oppenheimer, B. R. & Hinkley, S. 2009, Annu. Rev. Astron. Astrophys., 47, 253 (cited on pages 3 and 4)

Packham, C., Hough, J. H., & Telesco, C. M. 2005, in Astronomical Society of the Pacific Conference Series, Vol. 343, Astronomical Polarimetry: Current Status and Future Directions, ed. A. Adamson, C. Aspin, C. Davis, & T. Fujiyoshi, 38–+ (cited on page 36)

Pancharatnam, S. 1955, Proceedings Mathematical Sciences, 41, 130 (cited on page 19)

Patat, F. & Romaniello, M. 2006, Publ. Astron. Soc. Pac., 118, 146 (cited on page 21)

Perrin, M. D., Graham, J. R., & Lloyd, J. P. 2008, Publ. Astron. Soc. Pac., 120, 555 (cited on page 91)

Perrin, M. D., Schneider, G., Duchene, G., et al. 2009a, Astrophys. J. Lett., 707, L132 (cited on page 42)

Perrin, M. D., Schneider, G., Duchene, G., et al. 2009b, Astrophys. J. Lett., 707, L132 (cited on page 101)

Phillips, J. P. & Ramos-Larios, G. 2007, Astron. J., 133, 347 (cited on pages 89, 94, and 100)

Poetzel, R., Mundt, R., & Ray, T. P. 1989, Astron. Astrophys., 224, L13 (cited on page 69)

Pojmanski, G. 2002, Acta Astron., 52, 397 (cited on page 73)

Preibisch, T., Ossenkopf, V., Yorke, H. W., & Henning, T. 1993a, Astron. Astrophys., 279, 577 (cited on page 43)

Preibisch, T., Ossenkopf, V., Yorke, H. W., & Henning, T. 1993b, Astron. Astrophys., 279, 577 (cited on page 97)

Pwa, T. H., Pottasch, S. R., & Mo, J. E. 1986, Astron. Astrophys., 164, 184 (cited on page 89)

Quanz, S. P., Meyer, M. R., Kenworthy, M. A., et al. 2010, Astrophys. J. Lett., 722, L49 (cited on page 4)

Racine, R., Walker, G. A. H., Nadeau, D., Doyon, R., & Marois, C. 1999, Publ. Astron. Soc. Pac., 111, 587 (cited on pages 9, 71, and 91)

Ramstedt, S., Maercker, M., Olofsson, G., Olofsson, H., & Schöier, F. L. 2011, Astron. Astrophys., 531, A148+ (cited on page 101)

Roddier, F. 2004, Adaptive Optics in Astronomy, ed. Roddier, F. (cited on page 20)

Rodenhuis, M., Canovas, H., Jeffers, S. V., & Keller, C. U. 2008a, in Society of Photo-Optical Instrumentation Engineers (SPIE) Conference, Vol. 7014, Society of Photo-

Optical Instrumentation Engineers (SPIE) Conference Series (cited on pages 7, 18, and 48)

Rodenhuis, M., Canovas, H., Jeffers, S. V., & Keller, C. U. 2008b, in Presented at the Society of Photo-Optical Instrumentation Engineers (SPIE) Conference, Vol. 7014, Society of Photo-Optical Instrumentation Engineers (SPIE) Conference Series (cited on page 90)

Rodenhuis, M., Canovas, H., Jeffers, S. V., & Keller, C. U. 2011a (cited on pages 7, 9, 18, 21, 28, 31, 48, and 72)

Rodenhuis, M., Canovas, H., Jeffers, S. V., & Keller, C. U. 2011b, In preparation (cited on pages 88, 90, and 91)

Sabbadin, F. 1984, A&A Suppl., 58, 273 (cited on page 88)

Sahai, R., Hines, D. C., Kastner, J. H., et al. 1998, Astrophys. J. Lett., 492, L163+ (cited on page 7)

Schoenberner, D. 1979, Astron. Astrophys., 79, 108 (cited on page 95)

Siebenmorgen, R., Zijlstra, A. A., & Krügel, E. 1994, MNRAS, 271, 449 (cited on page 88)

Sivaramakrishnan, A., Lloyd, J. P., Hodge, P. E., & Macintosh, B. A. 2002, Astrophys. J. Lett., 581, L59 (cited on pages 9, 71, and 91)

Smith, B. A. & Terrile, R. J. 1984, Science, 226, 1421 (cited on page 5)

Smith, L. F. & Aller, L. H. 1971, Astrophys. J., 164, 275 (cited on page 88)

Soummer, R., Ferrari, A., Aime, C., & Jolissaint, L. 2007, Astrophys. J., 669, 642 (cited on pages 4, 71, and 91)

Soummer, R., Pueyo, L., Ferrari, A., et al. 2009, Astrophys. J., 695, 695 (cited on page 4)

Stam, D. M., Hovenier, J. W., & Waters, L. B. F. M. 2004, Astron. Astrophys., 428, 663 (cited on page 42)

Stam, D. M., Hovenier, J. W., & Waters, L. B. M. F. 2005, in Astronomical Society of the Pacific Conference Series, Vol. 343, Astronomical Polarimetry: Current Status and Future Directions, ed. A. Adamson, C. Aspin, C. Davis, & T. Fujiyoshi, 207–+ (cited on page 18)

Stam, D. M., Laan, E., Selig, A., Hoogeveen, R., & Hasekamp, O. 2006, in European Planetary Science Congress 2006, 607–+ (cited on page 18)

Stenflo, J. O. & Keller, C. U. 1997, Astron. Astrophys., 321, 927 (cited on page 4)

Sudarsky, D., Burrows, A., Hubeny, I., & Li, A. 2005, Astrophys. J., 627, 520 (cited on page 3)

Suzuki, R., Kudo, T., Hashimoto, J., et al. 2010, in Society of Photo-Optical Instrumentation Engineers (SPIE) Conference Series, Vol. 7735, Society of Photo-Optical Instrumentation Engineers (SPIE) Conference Series (cited on page 12)

Suzuki, R., Tamura, M., Suto, H., et al. 2009, in American Institute of Physics Conference Series, Vol. 1158, American Institute of Physics Conference Series, ed. T. Usuda, M. Tamura, & M. Ishii, 293–298 (cited on page 12)

Szeifert, T., Hubrig, S., Schöller, M., et al. 2010, Astron. Astrophys., 509, L7+ (cited on pages 69, 75, 77, 78, and 83)

Tatarski, V. I. 1961, Science, 134, 324 (cited on page 58)

Taylor, A. R., Gussie, G. T., & Pottasch, S. R. 1990, Astrophys. J., 351, 515 (cited on page 89)

Taylor, A. R., Pottasch, S. R., & Zhang, C. Y. 1987, Astron. Astrophys., 171, 178 (cited on page 88)

Terebey, S., Shu, F. H., & Cassen, P. 1984, Astrophys. J., 286, 529 (cited on page 78)

Thalmann, C., Grady, C. A., Goto, M., et al. 2010, Astrophys. J. Lett., 718, L87 (cited on page 54)

Thalmann, C., Schmid, H. M., Boccaletti, A., et al. 2008, in Presented at the Society of Photo-Optical Instrumentation Engineers (SPIE) Conference, Vol. 7014, Society of Photo-Optical Instrumentation Engineers (SPIE) Conference Series (cited on page 18)

Thiebaut, E., Bouvier, J., Blazit, A., et al. 1995, Astron. Astrophys., 303, 795 (cited on page 68)

Todorov, K., Luhman, K. L., & McLeod, K. K. 2010, The Astrophysical Journal Letters, 714, L84 (cited on page 18)

Trujillo Bueno, J., Landi Degl'Innocenti, E., Collados, M., Merenda, L., & Manso Sainz, R. 2002, Nature, 415, 403 (cited on page 4)

Ulrich, R. K. 1976, Astrophys. J., 210, 377 (cited on page 78)

Underhill, A. B. 1983, Astrophys. J., 266, 718 (cited on page 88)

van Boekel, R., Min, M., Leinert, C., et al. 2004, Nature, 432, 479 (cited on page 42)

van den Ancker, M. E., Blondel, P. F. C., Tjin A Djie, H. R. E., et al. 2004, MNRAS, 349, 1516 (cited on page 68)

Velázquez, P. F. & Rodríguez, L. F. 2001, Rev. Mexicana Astron. Astrofis., 37, 261 (cited on page 69)

Verhoeff, A. P., Min, M., Pantin, E., et al. 2011, Astron. Astrophys., 528, A91+ (cited on page 54)

Vérinaud, C. & EPICS Team. 2010, in In the Spirit of Lyot 2010 (cited on pages 11 and 18)

Vérinaud, C., Kasper, M., Beuzit, J.-L., et al. 2010, in Society of Photo-Optical Instrumentation Engineers (SPIE) Conference Series, Vol. 7736, Society of Photo-Optical Instrumentation Engineers (SPIE) Conference Series (cited on page 12)

Vernin, J. & Munoz-Tunon, C. 1994, Astron. Astrophys., 284, 311 (cited on page 59)

Volten, H., Muñoz, O., Hovenier, J. W., et al. 2007, Astron. Astrophys., 470, 377 (cited on page 44)

Waelkens, C., Waters, L. B. F. M., de Graauw, M. S., et al. 1996, Astron. Astrophys., 315, L245 (cited on page 94)

Waters, L. B. F. M., Beintema, D. A., Zijlstra, A. A., et al. 1998a, Astron. Astrophys., 331, L61 (cited on pages 6, 89, 94, 99, 101, and 119)

Waters, L. B. F. M., Cami, J., de Jong, T., et al. 1998b, Nature, 391, 868 (cited on page 94)

Waters, L. B. F. M., Molster, F. J., de Jong, T., et al. 1996, Astron. Astrophys., 315, L361 (cited on page 94)

Weinberger, R. & Kerber, F. 1997, Science, 276, 1382 (cited on pages 7 and 88)

Weintraub, D. A., Sandell, G., & Duncan, W. D. 1991, Astrophys. J., 382, 270 (cited on page 6)

Whelan, E. T., Dougados, C., Perrin, M. D., et al. 2010, The Astrophysical Journal Letters, 720, L119 (cited on pages 68, 69, and 80)

Whitney, B. A., Clayton, G. C., Schulte-Ladbeck, R. E., et al. 1993, Astrophys. J., 417, 687 (cited on pages 68, 75, 77, 78, and 83)

Whitney, B. A. & Hartmann, L. 1993, Astrophys. J., 402, 605 (cited on pages 77, 81, and 82)

Willems, F. J. & de Jong, T. 1986, Astrophys. J. Lett., 309, L39 (cited on page 95)

Williams, J. P. & Cieza, L. A. 2011, ArXiv e-prints (cited on page 6)

Wolszczan, A. & Frail, D. A. 1992, Nature, 355, 145 (cited on page 3)

Wynne, C. G. 1993, MNRAS, 262, 741 (cited on page 19)

Zijlstra, A. A., Gaylard, M. J., te Lintel Hekkert, P., et al. 1991, Astron. Astrophys., 243, L9 (cited on page 89)

Nederlandse samenvatting

Nederlandse samenvatting

Het werk dat gepresenteerd wordt in dit proefschrift is gebaseerd op de analyse van de data genomen met ExPo, de *Extreme Polarimeter*. ExPo is een zogenaamde *beeldvormende polarimeter* die ontworpen en gebouwd is door de groep van Prof. Christoph Keller aan de Universiteit van Utrecht. Het doel van dit instrument is om via polarisatie de circumstellaire omgevingen rond verschillende typen sterren te detecteren.

Polarimetrie is een tak van optica die de eigenschappen van het elektrisch veld dat geassocieerd wordt met licht bestudeert. Licht kan gepolariseerd worden via verschillende fysische mechanismen. Dit werk concentreert zich op de polarisatie die gevormd wordt door de verstrooiing van licht door stofdeeltjes. Onder verstrooiing verstaat men het fysische proces waarbij een deeltje van richting verandert onder invloed van bijvoorbeeld een atoom, een molecuul of een stofdeeltje. Afhankelijk van de eigenschappen (de grootte en vorm) van de deeltjes waardoor en de hoek waaronder het licht verstrooid wordt verandert de mate van polarisatie.

Het grootste obstakel bij het bestuderen van circumstellaire omgevingen is het grote verschil in helderheid tussen de ster en zijn omgeving. Een jonge ster is typisch tienduizend maal zo helder als zijn protoplanetaire schijf. Echter, het licht dat uitgezonden wordt door deze ster is voor het merendeel ongepolariseerd, terwijl het licht dat verstrooid wordt door deze schijf wel gepolariseerd is. Dit maakt polarimetrie tot een elegante methode om het ongepolariseerde licht van de ster te verwijderen, waardoor alleen het gepolariseerde licht van de schijf overblijft. Verder geeft, zoals hierboven al genoemd, het bestuderen van de polarisatie van het licht meer informatie over de eigenschappen van de circumstellaire materie, waaronder de geometrie en de samenstelling van het stof waaruit het bestaat.

Tijdens mijn promotie onderzoek was ik actief betrokken bij de ontwikkeling van ExPo. Dit instrument combineert een ferro-elektrisch vloeibaar kristal (vanaf nu: FVK) met een bundelsplitser. De FVK schakelt iedere 0.028 seconden tussen twee toestanden, A en B. Iedere keer dat de FVK schakelt wordt de polarisatie van het licht 90° geroteerd. De bundelsplitser verdeelt het licht in twee bundels met tegenovergestelde polarisatie richtingen, waardoor tegelijkertijd twee orthogonaal gepolariseerde beelden geproduceerd worden van het waargenomen object. De combinatie van de snelle modulatie (door de FVK) en de dubbele-bundel techniek

minimaliseert de systematische fouten, waardoor de gevoeligheid voor zwakke polarisatie eigenschappen toeneemt. Doordat ExPo korte belichtingstijden gebruikt, worden de gevolgen van atmosferische verstoringen (*seeing*) gereduceerd. Door de beelden correct samen te voegen wordt het mogelijk om de invloed van seeing met een factor ~ 30 te verbeteren, waardoor de ruimtelijke resolutie verbeterd wordt.

ExPo is ontworpen als een bezoekers instrument. Dit betekent dat het gemakkelijk vervoerd kan worden en opgebouwd op een optische tafel. Het instrument is gebruikt met de William Herschel Telescoop in het *Observatorio del Roque de los Muchachos* (La Palma) bij vijf verschillende waarneem campagnes. Tijdens deze sessies heeft ExPo een rijkdom aan data geproduceerd van observaties van verschillende objecten, waaronder protoplanetaire schijven, post-AGB sterren, de planeten Saturnus en Venus en kometen in ons zonnestelsel.

Zoals alle nieuwe astronomische instrumenten heeft ook ExPo te kampen gehad met onvoorspelbare problemen, welke ik opgelost heb met behulp van data analyse. Het speerpunt van het werk dat ik gedaan heb is de door mij ontworpen ExPo data reductie methode (ook wel de *ExPo pipeline*. Deze pipeline bestaat uit een set verschillende codes die geoptimaliseerd zijn om alle informatie over polarisatie te onttrekken uit de data die genomen is met ExPo. Met deze pipeline is het mogelijk om gereduceerde data te produceren waaruit het merendeel van de systematische fouten van het instrument verwijderd zijn. Deze data kan dan bijvoorbeeld vergeleken worden met verschillende modellen en simulaties om onze observaties te begrijpen.

De resultaten die in dit proefschrift gepresenteerd worden zijn verdeeld in vier hoofdstukken. Het eerste hoofdstuk behandelt de data reductie technieken die nodig zijn om de ExPo data te analyseren. Het tweede hoofdstuk combineert simulaties van protoplanetaire schijven met een numerieke simulatie van ExPo. Deze simulaties zijn bedoeld om de ExPo data beter te kunnen begrijpen. De laatste twee hoofdstukken behandelen observaties die met ExPo zijn gedaan. Het derde hoofdstuk behandelt de gepolariseerde eigenschappen van het jonge dubbelster systeem Z CMa. Het vierde hoofdstuk beschrijft de resultaten van de observatie van BD+303639, een bekende planetaire nevel.

Data reductie voor hoog-contrast beeldvormende polarimetrie

Het ExPo instrument is van de grond af aan ontworpen en gebouwd aan de Universiteit van Utrecht. Het is belangrijk om het instrument te doorgronden om een inzicht te krijgen in de kracht en zwaktes van het apparaat. Daarnaast is het belangrijk om geautomatiseerde data reductie te hebben, aangezien het instrument erg veel data produceert (tot 500 GB per nacht). In hoofdstuk XXX beschrijf ik de data reductie voor ExPo. Een deel van deze beschrijving is alleen van toepassing op ExPo, zoals bijvoorbeeld de uitlijning van de camera beelden. In dit hoofdstuk wordt aangetoond dat uitlijning op basis van een sjabloon betere resultaten oplevert dan uitlijning op de helderste *speckle*, zoals vaak wordt gedaan met korte belichtingstijd.

Simulaties van protoplanetaire schijven

Een correcte interpretatie van polarimetrische waarnemingen is verre van triviaal. Afhankelijk van de eigenschappen van de stofwolk, de eigenschappen van de waargenomen objecten (zoals een rustige of actieve schijf), en de artefacten van de telescoop en/of het instrument, is het mogelijk om tot sterk uiteenlopende conclusies te komen. In hoofdstuk 2 simuleren we allereerst de effecten van de eigenschappen van de stofwolk in twee types protoplanetaire schijven: actief en rustig. Vervolgens combineren we deze simulaties met een numerieke simulatie van het ExPo instrument zelf. Deze simulatie omhelst een aantal *point spread functies* (PSFs) met foton ruis, en instrumentele artefacten zoals uitlees ruis en instrumentele polarisatie. De gesimuleerd ExPo data wordt vervolgens gereduceerd met de methode beschreven in het eerste hoofdstuk van dit proefschrift. De numerieke simulaties van ExPo helpen ons om de geproduceerde data van dit instrument beter te begrijpen, alsmede de artefacten die ontstaan tijdens de data reductie, zoals bijvoorbeeld de effecten van een verkeerde schatting van instrumentele polarisatie. De hier beschreven numerieke simulatie van ExPo wordt gebruikt voor het modelleren van de waarnemingen van Z CMa, welke besproken worden in hoofdstuk 3 van dit proefschrift, en BD+303639, besproken in hoofdstuk 4.

Z CMa: Het ontrafelen van de eigenschappen van een jong dubbelster systeem via *imaging polarimetry*

In hoofdstuk 3 presenteer ik de eerste polarimetrische afbeeldingen van Z CMa. Dit is een erg complex binair systeem, waar een asymmetrische gaswolk de primaire Herbig Be ster omhult. Een enorme jet van deze ster boort een gat in het invallende materiaal dat zowel de primaire als de secondaire ster (een FU Ori ster) omhult. Met behulp van data van ExPo detecteren we drie verschillende polarisatie kenmerken op dit object. Twee daarvan zijn nog niet eerder beschreven, en we bespreken de mogelijke oorzaken daarvan. We vinden dat een gat in de gaswolk om de primaire ster een van deze polarisatie kenmerken kan verklaren. Verder bevestigen we dat verstrooiing van de wand van het gat in de gaswolk het tweede polarisatie kenmerk kan verklaren. Daarnaast stellen we dat een tweede gat in de gaswolk of een jet-gaswolk botsing het derde kenmerk in onze data kan verklaren. Tenslotte vergelijken we een radiatief stralingsmodel van het systeem met de data van ExPo om een schatting te maken van de hoeveelheid materie die uit het omhulsel het systeem invalt.

Het karakteriseren an de neutrale halo van BD+303639 met *imaging polarimetry*

BD+303639 is een fascinerende protoplanetaire nevel (PPN). De centrale ster is een koolstof-rijke, hete Wolf-Rayet ster (WC0). Dit systeem kwam onder de aandacht van de astronomische gemeenschap na de ontdekking van silicaten (Waters et al. 1998a) in de nevel, welke worden geassocieerd met een zuurstof-rijke chemie. Omdat de nevel erg jong is, impliceert dit dat de centrale ster van BD+303639 in de afgelopen 1000 jaar veranderd is van een zuurstof-rijke naar een koolstof-rijke chemie. Metingen

van de samenstelling van de neutrale halo rondom de centrale ster zijn cruciaal om deze evolutie en chemie verandering te verklaren. Waarnemingen met ExPo van deze nevel geven ons nauwkeurige informatie over de stofeigenschappen in het neutrale omhulsel. Middels een vergelijking met modellen kunnen we de straal van de zuurstof-rijke ring rondom de ster meten.

Resumen

El trabajo presentado en esta tesis está basado en el análisis de los resultados obtenidos con ExPo, el "Extreme Polarimeter" (Polarímetro Extremo). ExPo es un *imaging polarimeter*[1] que ha sido diseñado y construido por el grupo del profesor Christoph Keller, en la Universidad de Utrecht. El propósito de este instrumento es detectar y caracterizar los entornos estelares en diferentes tipos de estrellas mediante el uso de la polarimetría.

La polarimetría es la rama de la óptica que se ocupa de estudiar las propiedades del campo eléctrico asociado a la luz. La luz puede polarizarse mediante diferentes mecanismos; en esta tesis me centro en la polarización causada por *scattering* por polvo. El scattering es el proceso por el cual una partícula de luz (fotón en el caso que aquí nos ocupa) modifica su trayectoria debido al efecto de otra partícula (ya sea átomo, molécula, polvo). Dependiendo de las propiedades (tamaño, forma, etc) de las partículas causantes del scattering y del ángulo de scattering, la luz será polarizada en mayor o menor medida.

Como se ha dicho anteriormente, el objetivo de ExPo es proporcionar imágenes de diferentes entornos estelares. El principal problema que aparece cuando se intentan obtener imágenes de dichos entornos es el elevado contraste (diferencia de intensidad) presente en estas imágenes. Por ejemplo, una estrella joven es usualmente cuatro órdenes de magnitud (10000 veces) más brillante que su disco protoplanetario. Por otro lado, la luz producida en las estrellas es principalmente luz sin polarizar, mientras que la luz reflejada por el disco protoplanetario (propiamente hablando, luz que ha sido desviada de su trayectoria previa mediante el proceso de *scattering*) está (linealmente) polarizada. Por tanto, la polarimetría ofrece un método elegante para eliminar la mayor parte de la luz de la estrella, permitiendo la detección de los fotones polarizados. Además, y como ha sido explicado anteriormente, haciendo uso de la polarimetría podemos aprender más sobre las propiedades de los entornos estelares, como son la composición del polvo, geometría de los diferentes entornos estelares, etc.

Durante mi doctorado he estado involucrado activamente en el desarrollo de ExPo. Este instrumento combina un cristal líquido ferroeléctrico (*ferroelectric liquid crystal*, FLC) con un *polarizing beamsplitter*. El FLC cambia de estado, alternando entre

[1] Instrumento que obtiene imágenes polarizadas.

dos estados ("A" y "B") cada 0.028 segundos. Cada vez que el FLC cambia del estado A al B, el plano de polarización de la luz es rotado 90°, y viceversa. El *beamsplitter* divide el haz de luz en dos haces con estados opuestos de polarización, generando dos imágenes simultáneas, polarizadas ortogonalmente, del objeto observado. La combinación de rápida modulación (producida por el FLC) y de un *polarizing beamsplitter* minimiza los errores sistemáticos del instrumento, aumentando la sensibilidad de ExPo. Además, los cortos tiempos de exposición empleados por ExPo permiten reducir los efectos causados por el *seeing* atmosférico. Mediante un apropiado alineamiento de las imágenes adquiridas con ExPo, es posible mejorar el efecto del *seeing* hasta un factor del ~ 30%, aumentando así la resolución espacial de dichas imágenes.

ExPo ha sido diseñado como un instrumento visitante, lo que significa que puede ser fácilmente empaquetado y montado de nuevo en diferentes telescopios. En los cuatro años de mi doctorado, ExPo ha visitado el Telescopio William Herschel del Observatorio del Roque de los Muchachos (La Palma) en cinco ocasiones. Durante las observaciones realizadas en estas visitas, ExPo ha producido más de 2 Terabytes de datos, obteniendo imágenes polarizadas de diferentes objetos como discos protoplanetarios, estrellas post-AGB, cometas y planetas de nuestro sistema solar (Venus y Saturno).

Como cualquier nuevo instrumento en astronomía, los datos obtenidos con ExPo han estado afectados por multitud de problemas, *a priori* inesperados, que he tenido que resolver mediante diferentes técnicas de procesado y análisis de datos. La piedra angular del trabajo que aquí presento es el paquete de programas encargados de procesar y analizar todas las imágenes obtenidas con ExPo. Mediante este set de programas es posible obtener imágenes polarizadas en las que la mayor parte de los errores sistemáticos asociados a ExPo han sido eliminados. Las imágenes así obtenidas son posteriormente comparadas con diferentes modelos y simulaciones para poder explicar nuestras observaciones.

Los resultados que presento en esta tesis están divididos en cuatro capítulos. En el primer capítulo se explican las técnicas de procesado de imágenes que son necesarias para poder analizar las imágenes obtenidos con ExPo. El segundo capítulo combina diferentes modelos de discos protoplanetarios con una simulación numérica de ExPo. Estas simulaciones nos ayudan a entender mejor las imágenes producidas por ExPo. Los capítulos tercero y cuarto están dedicados al análisis de dos objetos observados con ExPo. En el tercer capítulo, analizamos las regiones polarizadas que aparecen en nuestras imágenes de Z CMa, un sistema binario formado por una estrella tipo FU Orionis y otra tipo Herbig Be. El cuarto capítulo describe nuestros resultados sobre BD+303639, una nebulosa planetaria extensivamente estudiada en previos trabajos.

Data Reduction Techniques for High Contrast Imaging Polarimetry

ExPo es un instrumento que ha sido diseñado y construido "desde cero" en la Universidad de Utrecht. Un estudio riguroso del comportamiento de este instrumento es necesario para poder conocer sus puntos fuertes y débiles. Por otro lado, y debido a la enorme cantidad de datos que pueden ser generados con ExPo (en torno a 500

Gigabytes de datos/900,000 imágenes por noche de observación), es fundamental disponer de un conjunto de códigos numéricos que automáticamente puedan analizar estos datos. En este capítulo describo los procedimientos que deben ser empleados para obtener el máximo rendimiento de los datos obtenidos por ExPo. Algunos de los resultados que aquí presento son sólo aplicables a observaciones realizadas con ExPo, como ocurre con el procedimiento de alineado de imágenes aquí descrito. En este capítulo se comprueba que alinear las imágenes obtenidas con ExPo con respecto a una imagen de referencia (*template*) produce mejores resultados que el tradicional método de alinear imágenes de acuerdo a los píxeles más brillantes (*brightest speckle*). Este último procedimiento es el más utilizado para alinear imágenes obtenidas con cortos tiempos de exposición.

Protoplanetary disk simulations

La correcta interpretación de las observaciones realizadas con un polarímetro es complicada. Dependiendo de las propiedades de los granos de polvo en los objetos observados, la geometría de dichos objetos (por ejemplo, discos acampanados (*flared*) o aplanados (*settled*)), y los efectos introducidos por el propio instrumento de medida y/o telescopio, es posible inferir conclusiones erróneas. En el capítulo 3 de esta tesis primero simulamos dos diferentes tipos de discos protoplanetarios: discos acampanados y discos aplanados. Para cada caso, calculamos varios modelos que tienen en cuenta diferentes tamaños de granos de polvo. Estas simulaciones son combinadas con una simulación numérica de ExPo. Dicha simulación incluye un set de *point spread functions* (PSFs) con ruido fotónico y efectos instrumentales como es el ruido de lectura, o la polarización instrumental. Las imágenes obtenidas en este proceso son analizadas siguiendo las pautas de análisis de datos que han sido explicadas en el capítulo previo. Estas simulaciones nos permiten entender mejor los datos obtenidos por ExPo, así como el efecto de los errores producidos durante el análisis de los datos (por ejemplo, los efectos de una incorrecta estimación de la polarización instrumental). La simulación numérica de ExPo descrita aquí es empleada durante el modelado de nuestras observaciones de Z CMa, discutido en el capítulo 4 de esta tesis, y the BD+303639, discutido en el capítulo 5.

Z CMa: Constraining the properties of a young binary system via Imaging Polarimetry

En el capítulo cuarto de esta tesis presento las primeras imágenes polarizadas de Z CMa. Éste es un sistema binario de gran complejidad, donde un capullo de polvo de simetría no bien definida envuelve a la estrella más masiva del sistema (estrella primaria). Un inmenso jet asociado a esta estrella está excavando una cavidad en la nube de polvo (*infalling envelope*) que rodea todo el sistema. Con las observaciones realizadas por ExPo, detectamos tres elementos polarizados en las imágenes de Z CMa. Dos de ellos no han sido descritos en previas observaciones de este sistema. Un agujero en el capullo de polvo que rodea a la primaria puede

explicar uno de los elementos polarizados que observamos en nuestras imágenes. Por otro lado, nuestros datos confirman que el *scattering* en las paredes de la cavidad excavada por el jet es el origen del segundo elemento polarizado que medimos en nuestros datos. Finalmente, sugerimos que otro agujero en el capullo de polvo, o una colisión entre el jet y una nube del polvo pueden ser el origen del tercer elemento polarizado que detectamos en nuestros datos. Para concluir, comparaciones de nuestras observaciones con varios modelos de Z CMa nos permiten obtener una primera aproximación para la tasa de caída (*falling rate*) del material que envuelve todo el sistema (*infalling envelope*).

Characterizing the neutral halo of BD+303639 via imaging polarimetry

BD+303639 es una nebulosa planetaria fascinante. Su estrella central es rica en Carbono, y pertenece a la categoría de estrellas Wolf-Rayet de tipo tardío [WC9]. Este sistema captó la atención de la comunidad astronómica después del descubrimiento de la presencia de silicatos (los cuales indican la presencia de abundante Oxígeno) en esta nebulosa. Debido a la juventud de la misma, este resultado implica que la estrella central de BD+303639 sufrió un cambio en su composición química, pasando de ser rica en Oxígeno a ser rica en Carbono en algún momento de los últimos 1000 años. Las medidas de la composión del material no ionizado (*neutral halo*) en torno a la estrella central son fundamentales para explicar la evolución, así como la transformación química de la estrella central de BD+303639. Las observaciones realizadas con ExPo proporcionan medidas precisas de la naturaleza de dicho material. Comparaciones con diferentes modelos nos permiten medir el radio exterior del envoltorio rico en silicatos.

Acknowledgments

First of all, I thank my supervisor Christoph Keller for giving me the opportunity to start a PhD in Utrecht. I still find amazing that I could enter his group, considering the extremely poor english that I had when talking to him the first time, during my phone interview. I have learned much more than I could imagine from you, Christoph.

In Michiel Rodenhuis I have found an excellent office mate and fellow during the ExPo-adventure. I really appreciate the time we spent at the optical lab, at the William Herschel Telescope, and driving from the Observatory while listening to The Doors, Rollings and many more classics. Thank for all that moments, and for making ExPo work.

Sandra Jeffers and Michiel Min, you both have been my personal referees during the last months of my PhD. Thank you. Sandra, I do really, really appreciate all your comments and suggestions, even when my papers were returned to me full of red ink. Michiel, the last chapters of my thesis were written in time thanks to your help and models, thanks again for this. I truly enjoyed all the discussions we had about science since that day, at around 06 00 a.m. at the WHT, when I told you: - Mmm there is something circularly shaped, quite polarized, that looks like a planet, in our RcRB data.... What do you think????!!!! - Mmmm".

Maria, you arrived the last to the little ExPo family, but you immediately became part of it. Thanks for helping with ExPo, for listening -some of- my screams in the telescope, and many more things. Stefano, all your problems with the ExPo pipeline helped me to really improve it. Thanks!

I am grateful to Klara for all her comments and advices about the introduction of this thesis. Gracias! And Tim, Sjors and Michiel, I am grateful to you all for your help with the dutch translation.

I am indebted to Thomas Henning, Sebastian Wolf, Lynne Hillenbrand, Frank Verbunt and Bram Achterberg, for reading my thesis.

Gracias Evencio, por haber sido mi tutor durante mi proyecto de fin de carrera. Trabajando contigo me di cuenta de que de verdad quería empezar un doctorado.

It is quite difficult for me to separate between the people from the department and my friends; in my case they form a well-mixed group. Catherine, you were the first person I met when I first arrived to Utrecht! I was just arriving from Lanzarote, it was quite late at night, and then you gave me the keys of my new apartment. Thanks

for that, and more important, thanks for being such a nice colleague and officemate. Matteo, it is a pity that we didn't start our PhD's at the same time. I enjoyed so much going out with you and the italian mafia. Selma, "mi niña"! Thanks for all your help during my "extremely-short-visit" at Baltimore, and for the nice moments here in Utrecht. Alex and Klara, thanks for all the cigarettes (and nice moments) I stole you. Nikola, I owe you one favor for teaching me how to make a ring with IDL, remember?... and many many more for all the dinners, drinks, and great, "non-scientific" discussions we had together. Aninha! I am so happy we started our PhD's together. Thank you for all the time we spent inside and outside the department, for your help with my english, and for all the (excellent) caipirinhas you have done. I want to drink many more (it is not a joke!). Without any special order, I would like to thank Axel, Carlo, Frans, Sander, Daria, Eveline, Jorrit, Helena, Marthain, Bob, Diederik, Joke, Sabina, and many more that I am probably skipping. Thanks also to Marion, Ed and Sake for helping to keep our department well organized an working.

Many friends have contributed to make my time in Utrecht unforgettable. Some of them just stayed in Utrecht for a few months, but they did contribute, in many different ways, to help me with my research. Germán, gracias por enseñarme nuevos pasos de baile, entre otras cosas. Irune, gracias por los momentos que pasamos juntos. Dany, además de un buen ajedrecista y jugador de pictionary (el arca de Noé!!), eres un gran colega. Sylvia, Meri, Belen, Victor, Elena, gracias por todos esos partidos, cenas, almuerzos y fiestas que nos han alegrado tantos momentos.

Quisiera dar las gracias muy especialmente a Juan y Mónica, por todos los momentos que hemos pasado juntos. Juan (Gañán!!!!!!!!!), me enseñaste más música de la que aprendí en varios años de conservatorio, además de incontables momentos de felicidad y risas. Mónica, siempre has estado ahí. Gracias por hacer la mejor tortilla del mundo, y por haber sido mi mejor "madre" en Utrecht (y sabes por qué lo digo).

Arjen, Esteban y Javi (mi Javi). I could have never imagined that I was going to find my best friends (or maybe brothers) here in Utrecht. And that they were going to live all together in Bilderdijkstraat 2B. You have been a constant source of joy during my PhD. I have learned so many things from you guys. You have been supporting me during the worst moments of my PhD, when it was always rainy and cloudy outside... Thank you. For everything.

"No es muy recomendable empezar una relación con un estudiante de doctorado a punto de terminar". Bea, conmigo has demostrado tener una paciencia infinita. Gracias por no rendirte conmigo, por apoyarme siempre, por animarme tanto durante los últimos tramos de mi tesis.

Gracias a mi hermana Helena por recordarme constantemente que, aunque esté lejos y en otros mundos, no debo olvidar mis raíces. Siembre es importante tener los pies en la tierra...

Finalmente, quisiera agradecer a mis padres todo lo que me han enseñado, y lo que aún les queda por enseñarme. Cuando tenía 4 años mi madre me enseñó un libro bastante viejo, lleno de dibujos de colores, que describía los planetas de nuestro Sistema Solar. Y empezó a contarme cosas acerca de ellos, y me enseñó sus nombres. Desde aquel momento nunca dejé de interesarme por los planetas, y por

la astrofísica en general. Así hasta terminar escribiendo una tesis que entre otras cosas, describe una técnica ('Imaging Polarimetry') que puede ayudar a detectar nuevos y lejanos planetas. Posiblemente, en aquel instante mi madre no podía ni imaginar las consecuencias de abrir aquel viejo libro, un acto que yo le agradezco infinitamente. De mi padre, además de aprender a discutir apasionadamente (a gritos según mis amigos), he heredado el amor por la lectura, que camina unido a las ganas (o necesidad) de aprender. Y sobre todo, he heredado su tenacidad (cabezonería). De él aprendí a no rendirme cuando un programa no me funciona, cuando mis cálculos no son correctos, o cuando simplemente todo me sale mal. Si no es por eso, habría sido mucho más fácil que me hubiera rendido en algún momento de los últimos cuatro años, que hubiera tirado la toalla, en lugar de enfrentarme a interminables líneas de (complicados) códigos numéricos.

Curriculum vitae

I was born in Almería, Spain. My love for astronomy started during my childhood, and it was probably enhanced by the amazing skies of the Canary Islands, where I lived since I was 4 years old.

I started the physics degree in 2002, in the Facultad de Física de La Laguna. In 2006 I obtained a studentship to work as a telescope operator in the Mons Telescope (Observatorio del Teide) and in the telescope of the Physics Department of La Laguna University. During the same year, I did my "Proyecto de Fin de Carrera", analyzing the (gravitational) microlensing effect in different quasars under the supervision of prof. Evencio Mediavilla. As part of this research, I attended the Gravitational Lensing School organized by the Marie Curie Network ANGLES, that took place in Valencia, 2007. I finished my degree in July 2007, obtaining the "Licenciatura en Física, especialidad astrofísica" in the Universidad de La Laguna.

In August 2007 I started my PhD research at Utrecht University, under the supervision of prof. Christoph Keller. Here I have worked in a complete different field, participating in the developing and data analysis of ExPo, the Extreme Polarimeter. During these four years I have visited the "Observatorio del Roque de los Muchachos" five times with ExPo. I have shown our results in conferences in Quebec, Hawaii and Maryland, and I have given invited talks in institutions such as the Instituto de Astrofísica de Canarias or the Space Telescope Science Institute, among others.

Astronomy compels the soul to look upwards and leads us from this world to another.

La astronomía obliga al alma a mirar hacia arriba y la conduce desde las cosas de aquí a las de allí en lo alto.

— Plato. ”The Republic”